

AD-A135 252

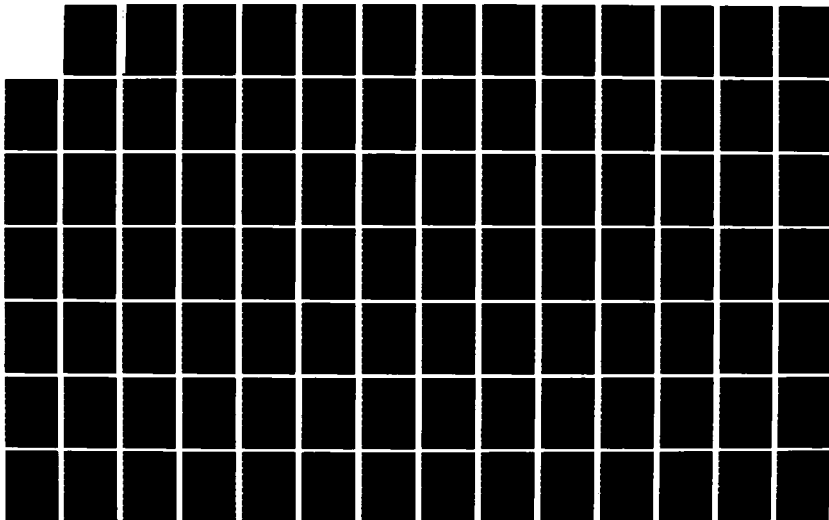
A STUDY OF MICROWAVE AND MILLIMETER-WAVE QUASI-OPTICAL
PLANAR MIXERS(U) TEXAS UNIV AT AUSTIN MICROWAVE LAB
K D STEPHAN ET AL. 31 AUG 83 MW-83-2 ARO-17735.25-EL
DAGG29-81-K-0053

1/3

UNCLASSIFIED

F/G 9/5

NL





MICROCOPY RESOLUTION TEST CHART
NATIONAL BUREAU OF STANDARDS-1963-A

(12)

A STUDY OF MICROWAVE AND MILLIMETER-WAVE
QUASI-OPTICAL PLANAR MIXERS

TECHNICAL REPORT

KARL D. STEPHAN AND TATSUO ITOH

AUGUST 31, 1983

U.S. ARMY RESEARCH OFFICE

CONTRACT NO. DAAG29-81-K-0053

UNIVERSITY OF TEXAS

DEPARTMENT OF ELECTRICAL ENGINEERING

AUSTIN, TX 78712

DTIC
ELECTE
S DEC 2 1983
A

AD-A185-262

DTIC FILE COPY

APPROVED FOR PUBLIC RELEASE;
DISTRIBUTION UNLIMITED

83 12 02 016

MICROWAVE LABORATORY REPORT No. 83-2

A STUDY OF MICROWAVE AND MILLIMETER-WAVE
QUASI-OPTICAL PLANAR MIXERS

TECHNICAL REPORT

KARL D. STEPHAN AND TATSUO ITOH

AUGUST 31, 1983

U.S. ARMY RESEARCH OFFICE

CONTRACT NO. DAAG29-81-K-0053

UNIVERSITY OF TEXAS
DEPARTMENT OF ELECTRICAL ENGINEERING
AUSTIN, TX 78712

DTIC
SELECTED
S DEC 2 1983
A


APPROVED FOR PUBLIC RELEASE;
DISTRIBUTION UNLIMITED

REPORT DOCUMENTATION PAGE		READ INSTRUCTIONS BEFORE COMPLETING FORM
1. REPORT NUMBER MW No. 83-2	2. JVT ACCESSION NO. A195 252	3. RECIPIENT'S CATALOG NUMBER
4. TITLE (and Subtitle) A Study of Microwave and Millimeter-wave Quasi-Optical Planar Mixers	5. TYPE OF REPORT & PERIOD COVERED Technical Report	
	6. PERFORMING ORG. REPORT NUMBER	
7. AUTHOR(s) Karl D. Stephan and Tatsuo Itoh	8. CONTRACT OR GRANT NUMBER(s) DAAG 29-81-K-0053	
9. PERFORMING ORGANIZATION NAME AND ADDRESS University of Texas at Austin Dept. of Electrical Engineering Austin, TX 78712	10. PROGRAM ELEMENT, PROJECT, TASK AREA & WORK UNIT NUMBERS	
11. CONTROLLING OFFICE NAME AND ADDRESS U. S. Army Research Office Post Office Box 12211 Research Triangle Park, NC 27709	12. REPORT DATE August 31, 1983	
	13. NUMBER OF PAGES	
14. MONITORING AGENCY NAME & ADDRESS (if different from Controlling Office)	15. SECURITY CLASS. (of this report) Unclassified	
	15a. DECLASSIFICATION/DOWNGRADING SCHEDULE NA	
16. DISTRIBUTION STATEMENT (of this Report) Approved for public release; distribution unlimited.		
17. DISTRIBUTION STATEMENT (of the abstract entered in Block 20, if different from Report) NA		
18. SUPPLEMENTARY NOTES The findings in this report are not to be construed as an official Department of the Army position, unless so designated by other authorized documents.		
19. KEY WORDS (Continue on reverse side if necessary and identify by block number) Quasi-optical mixer, slot-ring antenna, bowtie antenna, slot-ring mixer, Bowtie mixer, balanced mixer, subharmonic mixer, polarization duplexing		
20. ABSTRACT (Continue on reverse side if necessary and identify by block number) Quasi-optical mixers promise to simplify microwave and millimeter-wave receiving and remote sensing systems, especially where imaging of the field of view is desired. Two types of quasi-optical mixers were studied both experimentally and theoretically. One mixer used a slot-ring antenna, while the other used a bowtie antenna and an antiparallel diode pair to allow subharmonic local oscillator pumping. Both mixers are suitable for monolithic integration at millimeter wavelengths.		

The slot-ring antenna is formed by cutting an annular slot in a metallic sheet coated on one side with a dielectric layer. If a simple radial electric field distribution in the slot is assumed at the resonant frequency of the first-order mode, a Hankel-transform domain analysis permits prediction of the radiation patterns and radiation resistance of the antenna. These predictions were confirmed by measurement. An X-band balanced mixer model showed a measured conversion loss of $6.5 \text{ dB} \pm 3.1 \text{ dB}$ when fed by a local oscillator source behind the antenna.


To allow local oscillator frequencies of one-half the usual value, a broadband bowtie antenna was fabricated on a dielectric substrate and connected to an antiparallel pair of beam-lead diodes. A simple theory was developed to predict the antenna impedance, and agreed fairly well with previously published data. Pattern measurements of the bowtie antenna were used to calculate mixer conversion loss at 14 GHz, which was found to be $8.6 \text{ dB} \pm 2 \text{ dB}$. Finally, an alternate method of specifying quasi-optical mixer loss was proposed, in which the mixer is treated as an antenna.

Accession For	
NTIS GRA&I	<input checked="" type="checkbox"/>
DTIC TAB	<input type="checkbox"/>
Unannounced	<input type="checkbox"/>
Justification	
By _____	
Distribution/	
Availability Codes	
Dist	Avail and/or Special
A1	



A STUDY OF MICROWAVE AND MILLIMETER-WAVE
QUASI-OPTICAL PLANAR MIXERS

ABSTRACT



Quasi-optical mixers promise to simplify microwave and millimeter-wave receiving and remote sensing systems, especially where imaging of the field of view is desired. Two types of quasi-optical mixers were studied both experimentally and theoretically. One mixer used a slot-ring antenna, while the other used a bowtie antenna and an antiparallel diode pair to allow subharmonic local oscillator pumping. Both mixers are suitable for monolithic integration at millimeter wavelengths.

The slot-ring antenna is formed by cutting an annular slot in a metallic sheet coated on one side with a dielectric layer. If a simple radial electric field distribution in the slot is assumed at the resonant frequency of the first-order mode, a Hankel-transform domain analysis permits prediction of the radiation patterns and radiation resistance of the antenna. These predictions were confirmed by measurement. An X-band balanced mixer model showed a measured conversion loss of 6.5 dB \pm 3.1 dB when fed by a local oscillator source behind the antenna.

To allow local oscillator frequencies of one-half the usual value, a broadband bowtie antenna was fabricated on a dielectric substrate and connected to an antiparallel pair of beam-lead diodes. A simple theory was developed to predict the antenna impedance, and agreed fairly well with previously published data. Pattern measurements of the bowtie antenna were used to calculate mixer conversion loss at 14 GHz, which was found to be $8.6 \text{ dB} \pm 2 \text{ dB}$. Finally, an alternate method of specifying quasi-optical mixer loss was proposed, in which the mixer is treated as an antenna.

TABLE OF CONTENTS

Abstract	vii
List of Figures	xi
List of Tables	xv
CHAPTER 1: INTRODUCTION	1
Advantages of Quasi-Optics	2
Prior Work	2
Scope of This Work	3
PART I : THE SLOT-RING ANTENNA MIXER	5
CHAPTER 2: SLOT-RING ANTENNA THEORY	6
Simple Metallic Form and Babinet's Principle	6
Slot Ring Antenna on a Dielectric Substrate	13
CHAPTER 3: SLOT-RING ANTENNA EXPERIMENTS	26
Impedance Measurements	26
X-Band Radiation Pattern Measurements	30
Millimeter-wave Pattern Measurements	38
CHAPTER 4: MODES AND MODE ORTHOGONALITY	44
CHAPTER 5 : SLOT-RING MIXER THEORY	48
Approaches to Mixer Analysis	49
Mixer Using the Slot-Ring Antenna	55
CHAPTER 6: SLOT RING MIXER EXPERIMENTS	65
Conversion Loss Measurement Technique	65
Conversion Loss Experiments	71
CHAPTER 7: SLOT-RING MIXER AND POLARIZING FILTERS	80
Polarization Filter Design	80
Front Polarization Filter	83
Rear Polarization Filter	90
CHAPTER 8: PROPOSED USES AND CONCLUSIONS	92
Further Paths	92
Conclusions	98
PART II : THE BOWTIE ANTENNA SUBHARMONIC MIXER	99

CHAPTER 9: INTRODUCTION	100
CHAPTER 10: THE INFINITE FIN ANTENNA	102
CHAPTER 11: BOWTIE ANTENNA THEORY	111
Modes of Free Space	111
Modes the Bowtie Antenna Excites	113
Confirmation of Simple Theory	122
Subharmonic Mixer Using the Bowtie Antenna	126
Dielectric-Supported Bowtie	129
CHAPTER 12: SUBHARMONIC MIXER OPERATION	131
Background and Theory	131
Factors in Subharmonic Mixer Design	134
CHAPTER 13: BOWTIE ANTENNA MEASUREMENTS	138
CHAPTER 14: MAKING THE BOWTIE MIXERS	148
CHAPTER 15: BOWTIE MIXER EXPERIMENTS	151
14 GHz Tests	151
35 GHz Tests	157
CHAPTER 16: METRICS FOR QUASI-OPTICAL MIXERS	163
Difficulties in Measuring Quasi-Optical Mixer Conversion Loss	163
Effective Mixer Aperture	163
Isotropic Conversion Loss L_{150}	165
CHAPTER 17: BOWTIE MIXER CONVERSION LOSS RESULTS	168
Table Column Headings	168
Numerical Results	171
CHAPTER 18: PROPOSED USES AND CONCLUSIONS	176
APPENDIX A - DERIVATION OF FAR-FIELD EXPRESSIONS	179
APPENDIX B - FIELDS AT THE DIELECTRIC-AIR INTERFACE	182
APPENDIX C - KRADRNG PROGRAM	192
Bibliography	198

LIST OF FIGURES

No.		Page
2-1	Metal-only slot-ring antenna.	7
2-2	Complementary antenna impedances.	9
2-3	Loop antenna.	11
2-4	Comparison of microstrip and slot ring structures.	14
2-5	Slot ring feed method showing electric field in plane of device.	15
2-6	Slot ring model: (a) magnetic wall (b) equivalent circuit.	16
3-1	Slot-ring antenna radiation pattern measurement apparatus.	32
3-2	Measured E-plane patterns of slot-ring antenna with frequency as parameter.	34
3-3	Measured H-plane patterns of slot-ring antenna with frequency as parameter.	35
3-4	Calculated and measured H-plane patterns of slot-ring antenna at 10 GHz.	36
3-5	Calculated and measured E-plane patterns of slot-ring antenna at 10 GHz.	37
3-6	Calculated and measured H-plane patterns of alumina slot-ring antenna, 65.2 GHz.	41
3-7	Calculated and measured H-plane patterns of alumina slot-ring antenna, 95.5 GHz.	42
4-1	First three modes of the slot-ring antenna.	45
4-2	Slot-ring antenna feeds: (a) balanced (b) unbalanced.	47
5-1	Equivalent-circuit model of a general mixer.	50
5-2	Three diode models useful in mixer analysis: (a) ideal switch; (b) time-varying resistance; (c) time-varying resistance and capacitance.	52

No.	Page
5-3 Single-diode slot-ring mixer.	56
5-4 Equivalent circuit of single-diode slot-ring mixer.	57
5-5 Ideal diode with junction capacitance C_j and spreading resistance R_s .	60
6-1 Comparison of (a) conventional and (b) quasi-optical mixers.	67
6-2 Two-diode balanced slot-ring mixer showing diode input voltages.	72
6-3 Slot-ring mixer conversion loss measurement apparatus.	74
6-4 Matching network for 10 MHz IF.	75
7-1 Polarizing filter for use at X-band.	82
7-2 Use of polarizing filters with slot-ring mixer.	86
7-3 Typical dependence of conversion loss on LO power delivered to diodes.	89
8-1 Proposed array of slot-ring mixers.	93
8-2 Shielded coplanar-line IF outputs for mixer array.	94
8-3 Dish used for imaging.	96
8-4 Dielectric lens used for imaging.	97
10-1 The metal-only bowtie antenna.	103
10-2 Infinite fin antenna Z_{in} versus half-angle ψ .	106
10-3 (a) Symmetrical dipole (b) Unipole and ground.	107
11-1 Bowtie antenna exciting modes of free space.	114
11-2 General equivalent circuit of bowtie antenna.	117
11-3 Equivalent circuit of TM_{11} mode wave impedance.	121

No.	Page
11-4 Simplified equivalent circuit of bowtie antenna using only TM_{11} mode.	123
11-5 Comparison of measured patterns of metal-only bowtie antenna of electrical length = 240° with calculated TM_{11} mode pattern.	125
11-6 Calculated and measured real part of metal-only bowtie antenna impedance versus electrical length.	127
11-7 Calculated and measured imaginary part of metal-only bowtie antenna impedance versus electrical length.	128
11-8 Bowtie antenna on a dielectric substrate.	130
12-1 Equivalent circuits of conventional single-diode mixer showing (a) diode (b) ideal switch (c) switch waveform.	132
12-2 Equivalent circuits of subharmonic mixer showing (a) diodes (b) ideal switches.	134
12-3 Switching waveforms of subharmonic mixer.	135
13-1 Plan of radiation pattern measurements for bowtie antenna.	139
13-2 Bowtie antenna radiation pattern measurement apparatus.	141
13-3 Raw plot of bowtie antenna radiation pattern.	143
13-4 Data of Fig. 13-3 as processed and plotted by HP-85 computer.	144
13-5 E-plane patterns, 7 and 14 GHz, bowtie antenna.	146
13-6 H-plane patterns, 7 and 14 GHz, bowtie antenna.	147
14-1 Photograph of diode pair at bowtie antenna terminals.	150
15-1 Apparatus for 14 GHz conversion loss measurements.	152
15-2 Matching network used in bowtie mixer conversion loss experiments.	154
15-3 Impedance-matching capability of matching network in Fig. 15-2 at 400 MHz.	155

No.		Page
15-4	Photograph of bowtie mixer in front of LO horn.	158
15-5	Circuit used for impedance matching and DC diode tests in 35 GHz conversion loss work.	160
15-6	Current-voltage characteristics of bowtie mixer with power delivered to LO horn as parameter.	161
17-1	Relative IF output power versus LO power, 14 GHz bowtie mixer.	174
B-1	Slot-ring antenna showing coordinate system.	183

LIST OF TABLES

No.		Page
I	Slot-Ring Antenna Impedance Data	28
II	Alumina Slot-Ring Antenna Data	40
III	Slot-Ring Mixer Conversion Loss Calculations	77
IV	Bowtie Mixer Conversion Loss Data	169

CHAPTER 1: INTRODUCTION

Smaller, lighter, and more efficient: these are the goals that microwave engineers have strived for since the earliest days of radar development during World War II. The solid-state revolution took some time to reach the microwave industry, but in the last ten years the gallium arsenide field-effect transistor and other solid-state devices have replaced vacuum tubes in many transmitting, as well as all receiving, applications. This progress has allowed orders-of-magnitude reductions in microwave system size, weight, and power consumption.

The hope of integrating entire receiver front ends on one semiconductor substrate is being realized in several laboratories, although large quantities of monolithic microwave integrated circuits have yet to be made. One component which resists change, however, is the antenna. For a given wavelength, this essential component cannot be made smaller without sacrificing some desirable property, such as high forward gain or low sidelobe levels.

One way to retain a given forward gain while shrinking the antenna is to reduce the wavelength of operation. This approach to miniaturization is one factor contributing to recent increased interest in millimeter-wave technology [1], despite the atmospheric absorption problems and difficulties with sources that this move to higher frequencies involves.

ADVANTAGES OF QUASI-OPTICS

Another advantage which millimeter waves possess is the possibility of using quasi-optical techniques. Conventional rectangular waveguide shows losses as high as 5 dB/m at 90 GHz, which makes lengthy sections of waveguide unattractive at these frequencies. Properly designed quasi-optical systems, involving free-space transmission and optical components such as lenses, reflectors, and polarizers, can often achieve improved performance compared to a waveguide system [2].

A unique potential of quasi-optical receivers is their ability to perform instantaneous imaging of multiple radiation sources. Present passive imaging techniques generally involve sequential scanning, which takes a certain minimum time to perform. On the other hand, a truly optical imaging system, in which a two-dimensional image is focused upon an array of sensors or receivers, can distinguish many sources simultaneously in less time than it takes the scanning system to locate one source. The requirement in this application is for an array of millimeter-wave detectors or receivers, each of which is small enough to allow an adequate number of picture elements (pixels) to be concentrated in the limited focal plane area of a quasi-optical system.

PRIOR WORK

Although quasi-optical techniques have been applied for many years, there are relatively few references in the literature to mixers

having a true quasi-optical input in the form of a free-space wave. Clifton [3] described a 600-GHz mixer using a dielectric lens to focus energy onto a diode in a reduced-height waveguide. In principle, several such waveguides mounted side by side in an array could form a focal-plane imaging system, but the awkward waveguides containing point-contact diodes would create a nightmarish mechanical assembly.

The construction of microwave planar mixers on a dielectric substrate had to await manufacture of the beam-lead diode. These mass-produced devices possess much of the ruggedness of conventional packaged diodes, but their small size and reduced parasitic impedances makes them competitive with waveguide-mounted chip devices. A good example of current quasi-optical mixer work with beam-lead diodes on a planar substrate is the device built by Yuan, Paul, and Yen [4] working at 140 GHz. It also used a dielectric lens, but instead of a waveguide at the focus, two linear slot antennas on a quartz substrate received the incoming power. A mixer circuit was fabricated next to the antennas on the same substrate. Such planar construction is highly suitable for use in arrays.

SCOPE OF THIS WORK

This study is limited to the examination of two quasi-optical planar mixer structures suitable for imaging applications. In both cases, the work was carried on only to the point at which a single model structure was shown to work satisfactorily. Before arrays of these mix-

ers can be built, the individual structures must be scaled down to the desired wavelength, and mixer-mixer interactions need to be investigated.

This dissertation is divided into two parts, each dealing with one type of quasi-optical mixer. In Part I, the theoretical and experimental development of a device meeting the requirements for quasi-optical imaging is given. The device itself is a combined receiving antenna and mixer using an simple planar antenna structure called a slot-ring antenna. The analysis given will predict the terminal resistance and radiation patterns of the antenna. The predictions will be compared to experimental data which confirm their essential features. Next we describe the construction of a functioning mixer whose conversion loss is a respectable 6.5 ± 3 dB.

Part II describes a mixer whose function is essentially the same as the mixer of Part I. They differ in that the mixer of Part II uses a subharmonic local oscillator, making generation of the required power for a given input frequency much easier at millimeter wavelengths. A theoretical development of the bowtie antenna used in Part II adequately describes its behavior, and experiments follow the precedents established in Part I to determine conversion loss. The best conversion loss measured for the subharmonic mixer was 8.6 dB \pm 2 dB.

PART I : THE SLOT-RING ANTENNA MIXER

CHAPTER 2: SLOT-RING ANTENNA THEORY

The slot-ring antenna has several characteristics making it especially suitable for use in a quasi-optical mixer. In this chapter, we will thoroughly analyze the slot-ring structure as a radiator of electromagnetic waves. Three analysis methods will be discussed in order of increasing complexity. The first technique is based on the dual nature of the slot-ring antenna with respect to the well-studied wire-loop antenna. This method is useful for obtaining rough estimates of terminal impedance values and approximate radiation patterns. The second approach treats the antenna as a section of slot line bent into a loop. It is primarily useful for finding the resonant frequency of the first-order mode. Finally, a full-wave analysis will be presented which gives an easily evaluated expression for the real part of the input impedance as well as predictions of radiation patterns which agree well with experimental data.

SIMPLE METALLIC FORM AND BABINET'S PRINCIPLE

The slot ring structure in its simplest form, with no dielectric, is shown in Fig. 2-1. It is a planar structure formed by cutting a ring in an otherwise continuous metallic sheet. In this and all subsequent theoretical discussions, all flat conductors are assumed

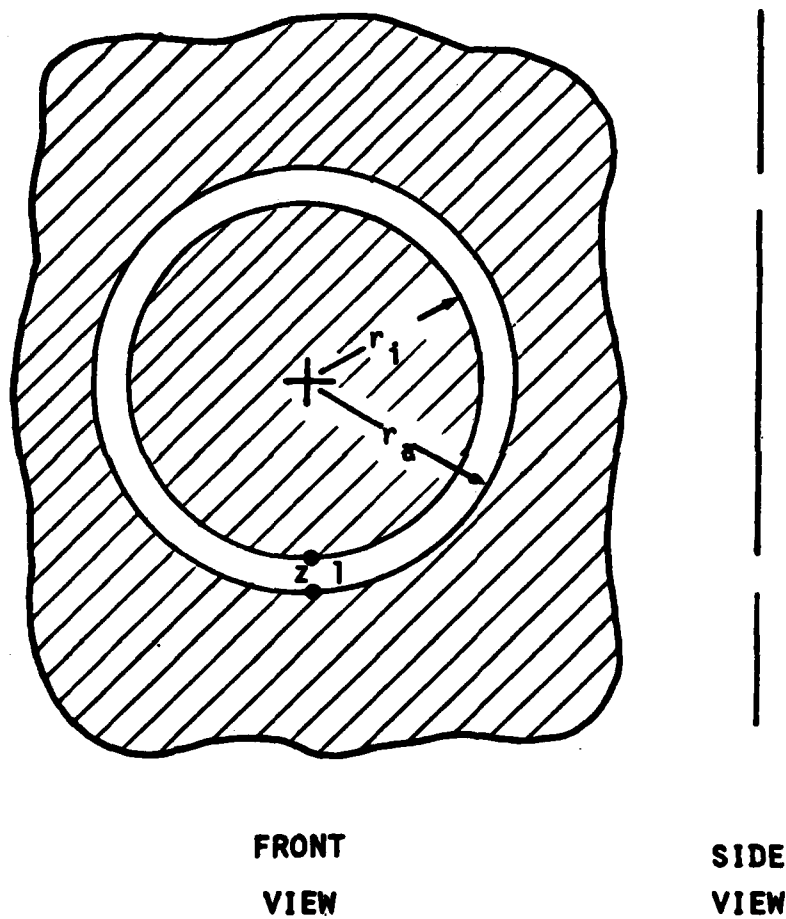


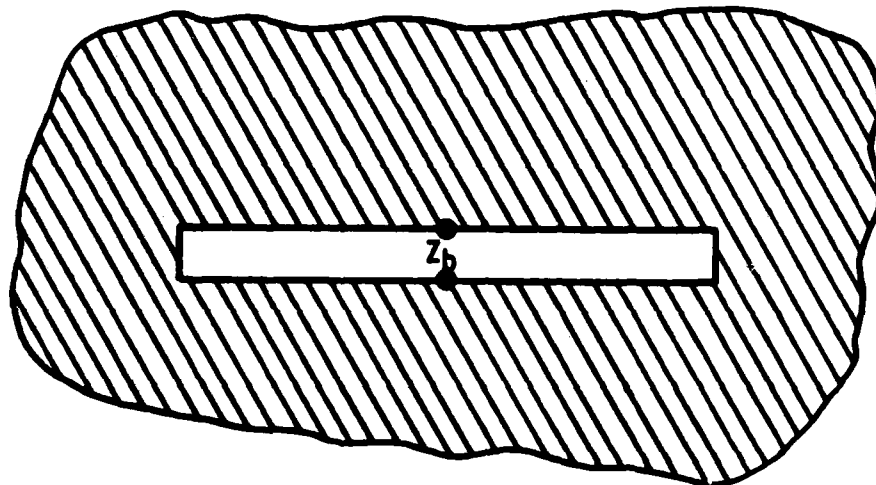
Fig. 2-1. Metal-only slot-ring antenna.

to be lossless and vanishingly thin. The relatively large conducting areas provided by the slot ring make this a good assumption for most cases. Power is fed to the antenna through terminals which bridge the gap, and the driving-point impedance seen at this point is denoted as Z_1 . The inner and outer radii of the ring are called r_i and r_a , respectively.

Without any direct analysis of this structure whatsoever, a rough idea of its behavior may be obtained through the use of Babinet's principle [1] as elaborated by Booker and Kraus [2]. Babinet addressed the problem of the light intensity behind an opaque screen of arbitrary shape illuminated from one side. It is intuitively obvious that if the original screen is replaced by its complement (transparent where the original screen was opaque and vice versa), the areas illuminated through the original screen will not be illuminated through the second screen. What Babinet showed was the mathematical fact that the sum of two intensities measured at any point behind two complementary screens equals the intensity present with no screen at all, even for gray areas in the diffraction zones of the screen edges.

Booker adapted Babinet's analysis to include polarization effects, and used it to derive an important theorem about the impedances of planar antennas that are mechanical complements or duals of each other. One example using this theorem is illustrated in Fig. 2-2, showing a dipole and a slot antenna of the same dimensions. Booker showed that if the input impedance of a dipole made of flat coplanar metal strips is Z_a , the impedance across the center of a slot of the same dimensions cut in an infinite metallic sheet is

IMPEDANCE OF MEDIUM = Z_0



$$4 Z_a Z_b = Z_0^2$$

Fig. 2-2. Complementary antenna impedances.

$$Z_b = \frac{Z_o^2}{4 \cdot Z_a}$$

(2-1)

where Z_o is the intrinsic impedance of the medium (376.7 ohms for vacuum). The analysis requires only that the terminal spacing be much smaller than a wavelength. This example is merely a specific application of the general principle which can be applied to any pair of complementary planar metallic structures.

Since the slot ring is formed on an infinite metallic sheet, we find that its dual or complementary structure is a loop antenna in which a flat ribbon replaces the customary wire of round cross-section (Fig. 2-3). Booker also asserts that a strip of width B much smaller than a wavelength can be replaced by a round wire of diameter approximately $B/2$. By replacing our ribbon conductor with a wire of the proper diameter, we arrive at a structure extensively studied in the literature: the wire loop antenna.

The slot ring is most useful for mixer service when operated at a wavelength near one ring circumference. Therefore, to find the approximate drive-point impedance using Equation 1, we seek the impedance of a loop whose perimeter equals one wavelength. Collin and Zucker [3] found that a loop having a perimeter of one wavelength and a ratio of wavelength to wire diameter of about 280 has a real impedance at resonance of 138 ohms. Using Booker's equation, we find that a slot-ring antenna with

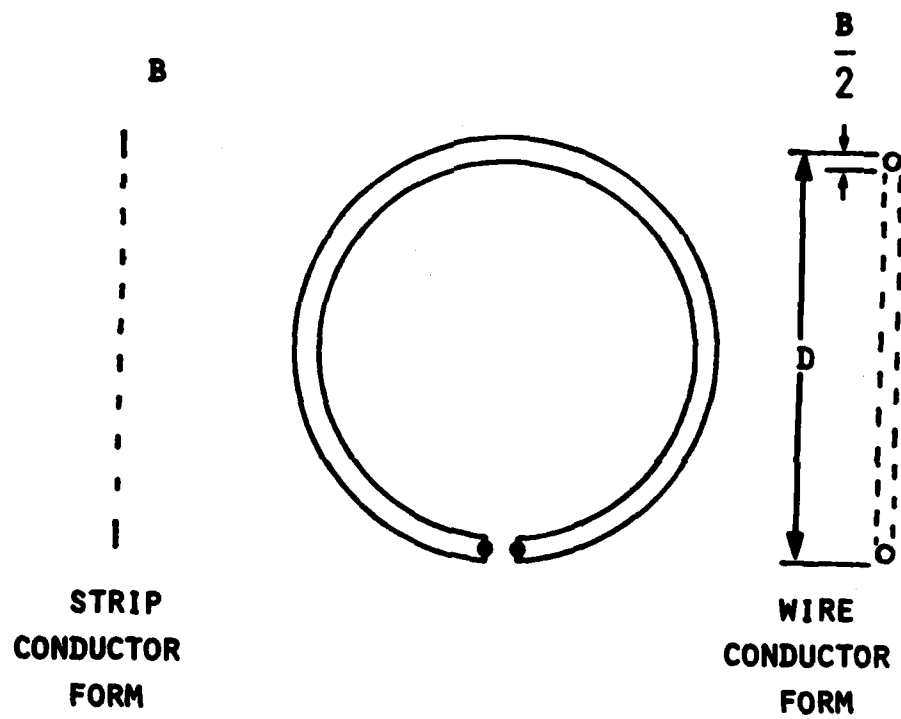


Fig. 2-3. Loop antenna.

a wavelength-to-gap ratio of about 140 should have a radiation resistance Z_r , at resonance, of approximately 257 ohms. The more elaborate theory developed later and applied to an antenna with a somewhat smaller wavelength-to-gap ratio predicts a resistance of 244 ohms, while the experimentally measured value was 232 ± 10 ohms.

In addition to the theorem concerning radiation resistance, Booker showed that the field patterns of complementary antennas are the same if the electric and magnetic fields are interchanged. Like the full-wavelength loop, a slot-ring antenna can be expected to radiate primarily in directions perpendicular to the plane of the loop, with a modest antenna gain of a few dB above that of a half-wave dipole.

These initial conclusions about the slot-ring antenna encouraged further analysis. The radiation pattern would allow reception in the desired directions with respect to the plane of a prospective array, and the impedance level was consistent with the idea of mounting mixer diodes directly across the slot gap. Diodes mounted this way show small parasitic inductance because of the large conductor area at their terminals.

So far, one very practical problem has been overlooked: if the supporting metal is cut away from the central disc, what holds it up? A practical structure must use some mechanical support for the center, and a dielectric substrate can provide this support. In addition to supporting the central conducting disc, the dielectric can double as the semiconductor substrate from which the mixer diodes are formed. The next chapter presents two analyses predicting the effects of a dielectric layer, including enhancement of antenna gain on the dielectric side.

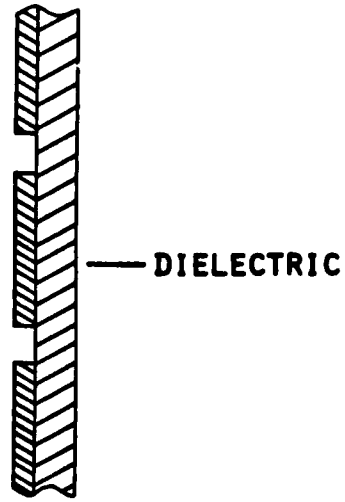
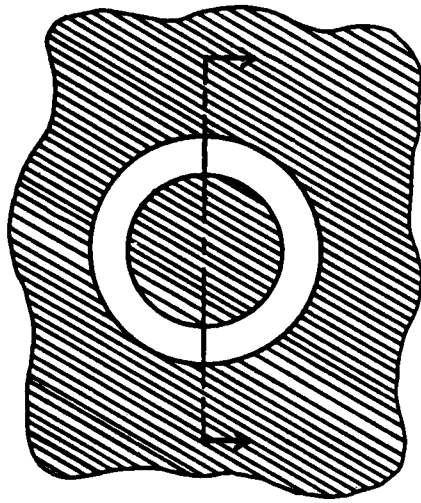
SLOT RING ANTENNA ON A DIELECTRIC SUBSTRATE

When a dielectric backing is added to the metallic slot antenna, the resulting structure is practical to fabricate by etching techniques on conductor-coated microwave substrates. The slot-ring structure thus formed is the dual of the more familiar microstrip ring resonator (see Fig. 2-4). The microstrip ring is a segment of microstrip bent into a loop; the slot ring is a segment of slot line bent into a loop. Slot line, first described by Cohn [4], is a planar waveguiding structure in which waves propagate along a slot or gap in a metal coating on a dielectric slab. It has recently found application in millimeter-wave mixers [5].

Like the microstrip resonator, the slot ring structure's resonant modes occur at frequencies for which the ring circumference is an integral number of guide wavelengths. To use the structure as an antenna, we excited the first-order azimuthal mode ($n=1$) by the means shown in Fig. 2-5. Neglecting the other modes for the moment, the impedance seen by the voltage source will be real at resonance, and all the power delivered will be radiated. Three problems arise: (1) how to calculate the resonant frequency; (2) how to determine the ring's radiation pattern; and (3) how to find the input resistance at resonance.

A first-order estimate of the resonant frequency can be derived from the transmission-line equivalent circuit of the slot ring (Fig. 2-6). By placing a magnetic wall across the ring as shown in Fig. 2-6(a), we disturb nothing since the structure is symmetrical. The wall

SLOT RING



MICROSTRIP RING

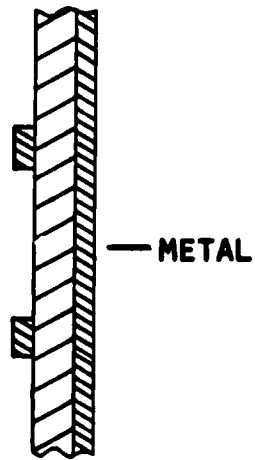
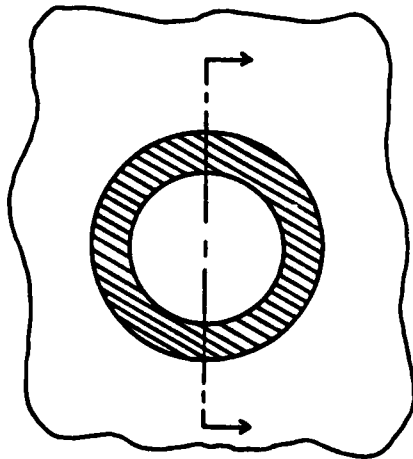


Fig. 2-4. Comparison of microstrip and slot ring structures.

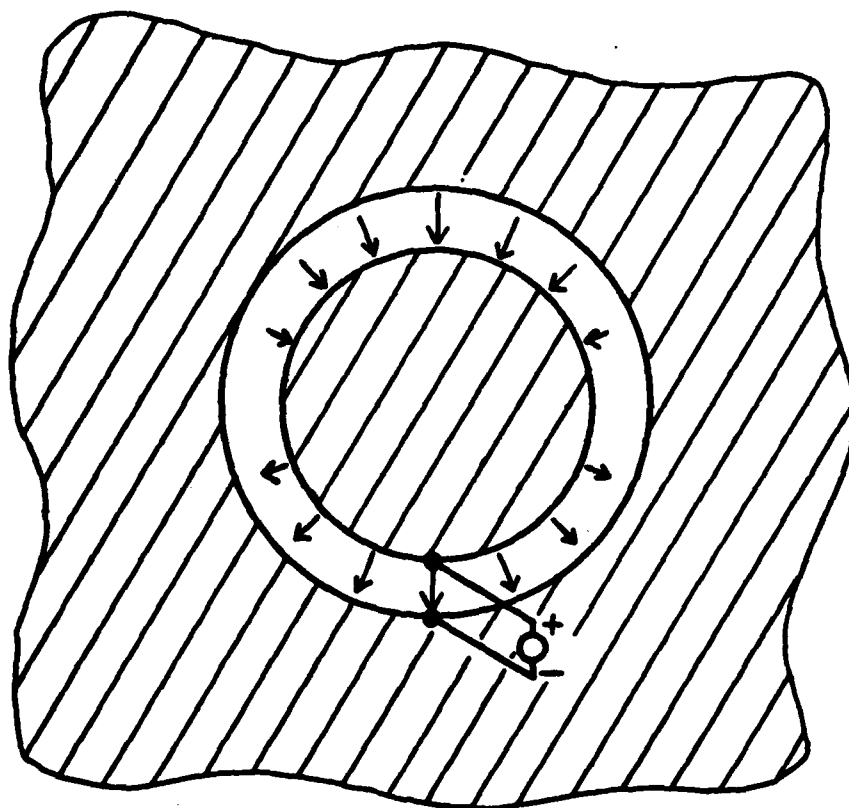


Fig. 2-5. Slot ring feed method showing electric field in plane of device.

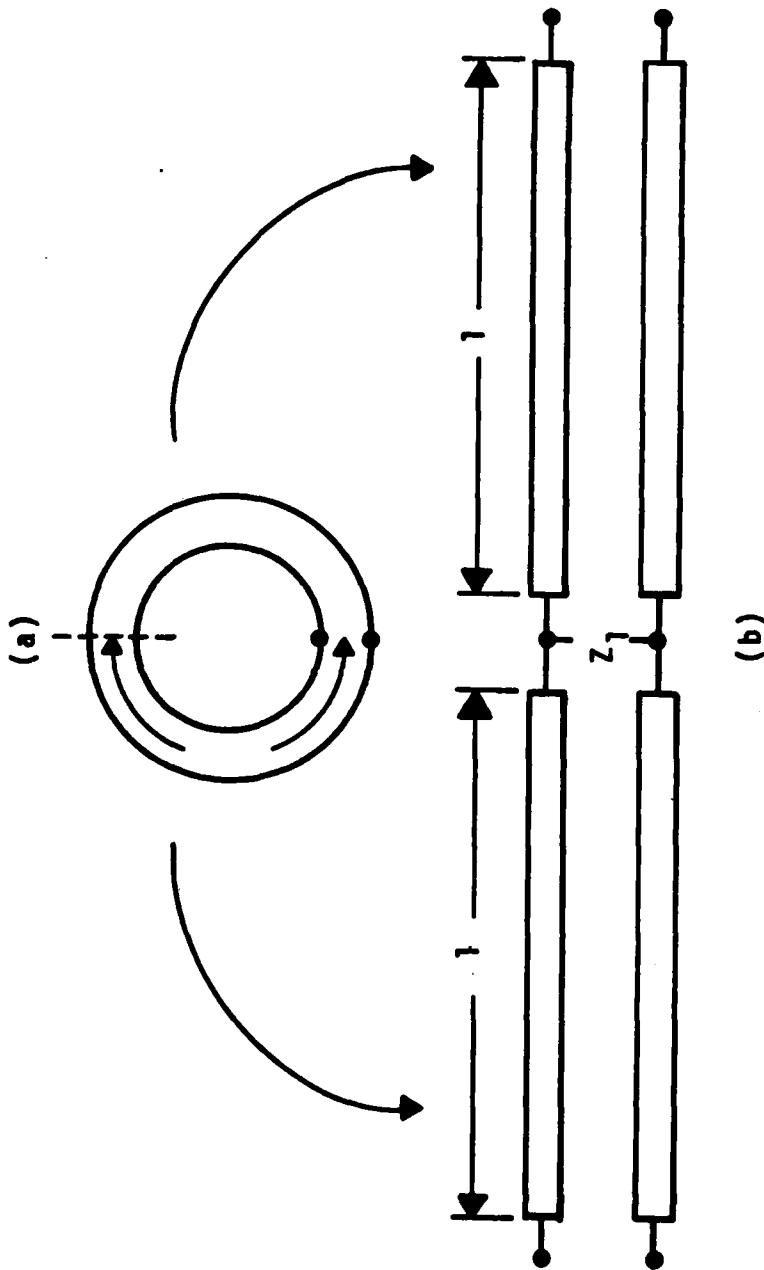


Fig. 2-6. Slot ring model: (a) magnetic wall
(b) equivalent circuit.

permits opening the ring at the point diametrically opposite the input terminals, since no current flows through the wall. This operation yields the equivalent transmission-line circuit shown in Fig. 2-6(b).

If we define the average ring radius r_{av} to be the arithmetic mean of the inner and outer radii r_i and r_o , the gap width g is $r_o - r_i$. At the resonant frequency of the first-order mode, the two lines are each a half-wave long electrically. Each line's mechanical length is approximately

$$l = \pi r_{av} \quad (2-2)$$

Knowledge of the mechanical length and the slotline velocity factor allows calculation of the resonant frequency within about 10%-15% of the actual value, even if the published tables for straight slot line [6] are used with the curved line shown in Fig. 2-6(a). The smaller the relative gap, g/r_{av} , the better the estimate will be. For a more precise calculation of the resonant frequency, recourse can be made to spectral-domain techniques such as in the paper by Kawano and Tomimuro [7]. Once the resonant frequency is determined for a particular application, both the radiation patterns and the radiation resistance may be found from the following analysis.

In 1981, Araki and Itoh [8] showed that if the tangential electric field was known on a cylindrically symmetric planar surface, the field could be Hankel-transformed to derive the far-field radiation pat-

terns from that surface. In their case, the fields had to be calculated from estimates of the currents on a microstrip patch. In the present case, however, a very simple estimate of the electric field in the slot will yield a good evaluation of the antenna patterns and the radiation impedance.

In choosing an estimate of the field, care should be taken to ensure that the functional form is easy to Hankel-transform analytically. The estimate chosen is this:

$$E_r(r) = 1/r \text{ for } (r_{av} - g/2) < r < (r_{av} + g/2) \quad (2-3)$$

$$E_r(r) = 0 \text{ otherwise} \quad (2-4)$$

$$E_\phi(r) = 0 \quad (2-5)$$

The motivation for the $1/r$ dependence will be explained below. This simple choice satisfies the boundary condition that the tangential electric field be zero on the metallic sheet, and expresses the intuitively reasonable idea that, for narrow gaps at least, the azimuthal field in the gap will be small compared to the radial field.

The $(n\pm 1)$ th order Hankel transforms of the chosen function are

$$\tilde{E}_{(\pm)}(\alpha) = \int_0^{\infty} E_r(r) J_{(n\pm 1)}(\alpha r) r dr \quad (2-6)$$

where $J_n(\alpha r)$ is the n th-order Bessel function of the first kind, and α is the Hankel transform variable. Applying this to the chosen estimate, we find

$$\tilde{E}_{(\pm)}(\alpha) = \int_{r_i}^{r_a} (1/r) J_{(n\pm 1)}(\alpha r) r dr \quad (2-7)$$

$$\tilde{E}_{(\pm)}(\alpha) = \int_{r_i}^{r_a} J_{(n\pm 1)}(\alpha r) dr \quad (2-8)$$

This integral is easy to evaluate analytically through recursion relations given in published tables [9]. Assuming that all the fields vary as $\exp(jn\phi)$ and using the saddle-point equations given in Reference [8] and reproduced in Appendix A, we find that the far-field equations for E_θ and E_ϕ are

$$E_{\theta}(r, \theta, \phi) = -(k_0/2r) \cdot j^n \cdot e^{j(n\phi - k_0 r)} \cdot [\tilde{E}_o(k_0 \sin\theta)] \quad (2-9)$$

$$E_{\phi}(r, \theta, \phi) = +(k_0/2r) \cdot j^{n+1} \cdot e^{j(n\phi - k_0 r)} \cdot (\cos\theta) [\tilde{E}_e(k_0 \sin\theta)] \quad (2-10)$$

where linear combinations of the Hankel-transformed estimates are used:

$$\tilde{E}_o(k_0 \sin\theta) = \tilde{E}_{(+)}(k_0 \sin\theta) - \tilde{E}_{(-)}(k_0 \sin\theta) \quad (2-11)$$

$$\tilde{E}_e(k_0 \sin\theta) = \tilde{E}_{(+)}(k_0 \sin\theta) + \tilde{E}_{(-)}(k_0 \sin\theta) \quad (2-12)$$

The spherical coordinates r , θ , and ϕ refer to the point at which the fields are measured, $r = 0$ being the center of the ring. The quantity k_0 is the wavenumber in free space, and n is the azimuthal order of resonance being analyzed. In the case of interest, $n = 1$ and $\omega = \omega_0$, the resonant frequency of the first-order mode.

Equations (2-9) through (2-12) apply to any tangential electric field in the plane containing the origin of the spherical coordinate system ($\theta = 90^\circ$). In order to treat the case of a finite thickness of dielectric, the estimated field in the gap is used to find the field on the far side of the dielectric layer. Then the dielectric-air interface becomes the new plane containing the known fields. In the

Hankel-transform domain, this is a relatively easy process. By matching boundary conditions at the dielectric-metal and dielectric-air interfaces, the tangential electric field at the latter interface can be expressed in terms of the Hankel-transformed field within the gap, which has already been assumed. The following equations for the Hankel-transformed fields at the dielectric surface are stated here without proof. Because of the extensive algebraic manipulation required, their derivations are given in Appendix B.

Let us define t to be the thickness of the dielectric layer of relative dielectric constant ϵ_r . If we let

$$\alpha = k_0 \sin\theta \tag{2-13}$$

$$\beta_1 = \sqrt{k_0^2 - \alpha^2} \tag{2-14}$$

$$\beta_2 = \sqrt{k_0^2 \epsilon_r - \alpha^2} \quad (2-15)$$

$$f_e(\alpha) = \frac{\beta_2 \cos(\beta_2 t) + j \epsilon_r \beta_1 \sin(\beta_2 t)}{\beta_2 \sin(\beta_2 t) - j \epsilon_r \beta_1 \cos(\beta_2 t)} \quad (2-16)$$

$$f_h(\alpha) = \frac{\beta_2 \sin(\beta_2 t) - j \beta_1 \cos(\beta_2 t)}{\beta_2 \cos(\beta_2 t) + j \beta_1 \sin(\beta_2 t)} \quad (2-17)$$

then the Hankel-transformed fields at the dielectric-air interface are given by

$$\tilde{E}_e(\alpha) = [\cos(\beta_2 t) + f_h(\alpha) \sin(\beta_2 t)] \cdot [\tilde{E}_{(+)}(\alpha) + \tilde{E}_{(-)}(\alpha)] \quad (2-18)$$

$$\tilde{E}_o(\alpha) = [\cos(\beta_2 t) - f_e(\alpha) \sin(\beta_2 t)] \cdot [\tilde{E}_{(+)}(\alpha) - \tilde{E}_{(-)}(\alpha)] \quad (2-19)$$

Substitution of these equations for $\tilde{E}_e(\alpha)$ and $\tilde{E}_o(\alpha)$ into Equations 2-11 and 2-12 now gives the far-field expressions for the dielectric-coated side of the slot-ring antenna.

It should be noted that this analysis assumes that only the first-order mode is excited, and that no higher-order surface waves arise. The former assumption is justified in the following way. Assum-

ing a parallel equivalent circuit for the various modes, the zero-order mode and all higher-order modes have very small radiation conductances compared to that of the first-order mode at its resonant frequency. Therefore, the other modes draw little current and can be neglected compared to the excitation of the first-order mode. We may assume that no higher-order surface waves propagate [10] when the dielectric thickness is less than

$$t_{\max} = \frac{\pi}{2k_0 \sqrt{\epsilon_r - 1}}$$

(2-20)

Also, the equations assume that the metallic sheet extends to infinity. Practical antennas always stop short of this, but the effects of a finite ground plane will appear as inaccuracies in the radiation patterns only near the plane of the device ($\theta = 90^\circ$).

The third problem to be addressed is the radiation resistance. A classic method [11] easily yields this quantity. The terminal voltage can be found by integrating the assumed field across the gap:

$$|V| = \int_{r_i}^{r_a} (1/r) dr \quad (2-21)$$

$$|V| = \ln(r_a/r_i) \quad (2-22)$$

The total power radiated from the antenna with this voltage at its terminals is obtained [12] with the aid of Equations (2-9) and (2-10):

$$P = (1/2\eta) \cdot \int \int_{\text{SPHERE}} (|E_\theta|^2 + |E_\phi|^2) dS \quad (2-23)$$

where η is the intrinsic impedance of free space.

Since the input impedance Z_1 at resonance is purely resistive, the input power at the terminals equals the radiated power:

$$2 \cdot (V^2/2Z_1) = P \quad (2-24)$$

The factor of two in front arises from the fact that the practical antenna is excited from only one point, but the field equations assume excitation of both orthogonal modes in quadrature ($\cos\phi + j\sin\phi$). Solving for Z_1 , we find

$$Z_1 = \frac{[\ln(r_a/r_1)]^2}{p}$$

(2-25)

Care must be taken to use the proper equations for E_ϕ and E_θ on the dielectric and metal sides. This completes the analysis of the antenna. Strictly speaking, the resistance found in Equation (2-25) applies only at the resonant frequency although it will not vary appreciably for a small frequency range around resonance. As we shall show, the slot ring operated at its first-order resonance is a fairly low-Q device so neither precise impedance calculations nor exact resonant frequencies are vital to a serviceable design.

CHAPTER 3: SLOT-RING ANTENNA EXPERIMENTS

To test the antenna theory just elucidated, we made extensive impedance and pattern measurements using a number of different slot-ring structures. The following paragraphs describe the construction and measurement of several large scale models as well as pattern measurements made with X-band antennas. The measured impedance values confirmed our theory, and the patterns were used to determine an antenna gain figure used in later mixer calculations.

IMPEDANCE MEASUREMENTS

Although direct impedance measurements at the X-band mixer frequency would have been most desirable, the equipment necessary to perform such measurements was not available at the time. Since our complex impedance measurement facilities were usable up to only 1 GHz, structures for these measurements were built to resonate between 500 MHz and 1 GHz. To investigate the behavior of the slot-ring structure with no dielectric, a thin slab of stiff foamed polystyrene plastic was obtained. Since its dielectric constant was about 1.03, negligible error was introduced by assuming that the antenna was suspended in air. A flat framework of copper plates and wires was soldered to the outer conductor of a piece of semirigid coaxial cable, and the entire assembly was made

flush with the slab's surface by carving small channels in it. Upon this flat surface we placed a sheet of aluminum foil which formed a good ground plane when pressure was applied with another styrofoam sheet. A circular hole was cut in the foil to form the outer edge of a slot ring when a round copper disc was soldered to the center conductor of the cable. The edge of the disc formed the inner edge of the slot. By varying the diameter of the hole in the foil, the slot width could be adjusted. The impedance data from this structure are given in Table I.

To observe the effect of a dielectric layer, we replaced one styrofoam sheet with a sheet of dielectric material having the thickness and dielectric constant given in Table I. Making the dielectric-loaded ring approximately half the size of the earlier foam-dielectric ring maintained the resonant frequency near the same value.

The calculated resonant frequencies were found in the following manner. For the foam-dielectric structure, the resonant free-space wavelength was roughly estimated to be the same as the ring circumference. The same procedure was followed for the dielectric-slab structure, except that the slot line guide wavelength was estimated from published tables [1].

A computer program was written to perform the numerical integrations required for the calculated impedance values. This program along with explanatory notes is reproduced in Appendix C. The impedances were calculated at the resonant frequencies measured in the laboratory.

The predicted resonant frequencies were lower than the measured ones by 11% for the foam-dielectric rings. This relatively small error

TABLE I
SLOT-RING ANTENNA IMPEDANCE DATA

Structure Dimensions				Calculated Values			Measured Values		
Inner Radius (cm)	Outer Radius (cm)	Dielectric Constant (Relative)	Layer Thickness (cm)	Resonant Frequency (MHz)	Radiation Resistance (ohms)	Resonant Frequency (MHz)	Radiation Resistance (ohms)	Radiation Q	
7.7	8.2	1	--	600	240*	675 ± 2	235 ± 10	5	
7.7	7.95	1	--	610	244*	676 ± 2	232 ± 10	6.6	
3.048	3.302	12	0.635	720	590**	882 ± 2	518 ± 20	25.9	

* At $f_0 = 660$ MHz

** At $f_0 = 880$ MHz

is acceptable for a first-order estimate. The larger 18% error for the dielectric-ring resonant frequency may be due to a poor mechanical contact between the dielectric surface and the foil or the copper disc. Electrochemical plating or evaporating metal on the surface would have created a superior metal-dielectric contact. Covering such a large area (30 cm X 30 cm) by these means was impractical, so the foil was held to the dielectric slab only by the slab's own weight. Perhaps a pneumatic or vacuum system for ensuring intimate contact would have been better than the gravity method used.

Agreement between the measured and calculated radiation resistance values was better than the predictions of resonant frequency. The calculated value of 240 ohms for the wide ring was validated within experimental error, and the narrow ring's measured resistance failed to encompass the calculated value by only two ohms. Possible laboratory effects accounting for the disagreement include reflections of the test signal from the surroundings, since the impedance measurement was not performed in an anechoic chamber. A long hall about 3.5 m wide and 3 m high was found to be an adequate, but not ideal, test area at 600 MHz. Movement of the antenna within the test area caused barely perceptible changes in the measured impedance values, so reflected waves were probably not significant. The dielectric antenna's unexpectedly low measured radiation resistance can again be accounted for by poor mechanical contact, which lowers the effective dielectric constant of the slab.

X-BAND RADIATION PATTERN MEASUREMENTS

Since no UHF pattern measurement facilities were available, we proceeded directly to pattern measurements at the intended frequency of operation: X-band. Accordingly, approximate dimensions were calculated for a slot ring that would resonate near 10 GHz. This was a convenient frequency since since several power sources were available for both signal and local oscillator use.

First, the microwave substrate material was selected. This fiberglass-filled plastic had a nominal dielectric constant of 2.23, and was 0.318 cm thick. A square about 10 cm X 10 cm was cut and a slot ring was machined in the copper coating. The ring's inner radius was 0.39 cm, and the outer radius was 0.54 cm.

Once the antenna was made, the problem of feeding it arose. Although direct coaxial cable feed was used in the UHF impedance measurements, it was felt that the relatively large cable would unduly disturb the currents near the ring. To approximate more closely the actual conditions of use, it was decided to mount a detector diode across the gap and use the antenna as a receiver. While it is true that no absolute power data could be obtained from the rectified current, this technique permitted measurement of relative radiation patterns.

The detected DC voltage appeared between the central copper disc of the antenna and the surrounding ground plane. Experiments showed that little disturbance of the measured pattern was caused by removing the rectified current through a thin wire going from the central disc to

a terminal at the edge of the ground plane. Another precaution, observed whenever possible, was to run the wire in a direction perpendicular to the incoming wave's polarization, so that currents picked up by the wire and possibly fed to the antenna were minimized.

The arrangement for measuring radiation patterns is shown in Fig. 3-1. To increase the system's dynamic range, the RF source was modulated at about 1 kHz and the detected voltage across a 1000-ohm load was monitored with a sensitive wave analyzer having a 100-Hz bandwidth. The noise floor was more than 35 dB below maximum output of the detector.

Since the low-barrier Schottky detector diode used (Aertech model A2S250) did not have a reliable square-law characteristic over this range, a constant input voltage about 10 dB above the noise floor was maintained at the input of the wave analyzer as the antenna was rotated. This constant level was achieved by adjusting the variable attenuator for a constant detected output. The attenuator readings versus angle of antenna rotation then gave a relative radiation pattern directly with no dependence on the diode characteristics. The limitations of manual rotation prevented taking data points at intervals closer than 5 degrees.

Plots were taken at 8, 10, and 12 GHz, both co-polarized and cross-polarized, in both the E-plane and the H-plane of the antenna. The E-plane is the plane perpendicular to the antenna plane containing the antenna terminals. All plots in this chapter are normalized so that the maximum value for any given plot is 0 dB. This prevents direct comparison between two different plots. Nevertheless, changes in pattern

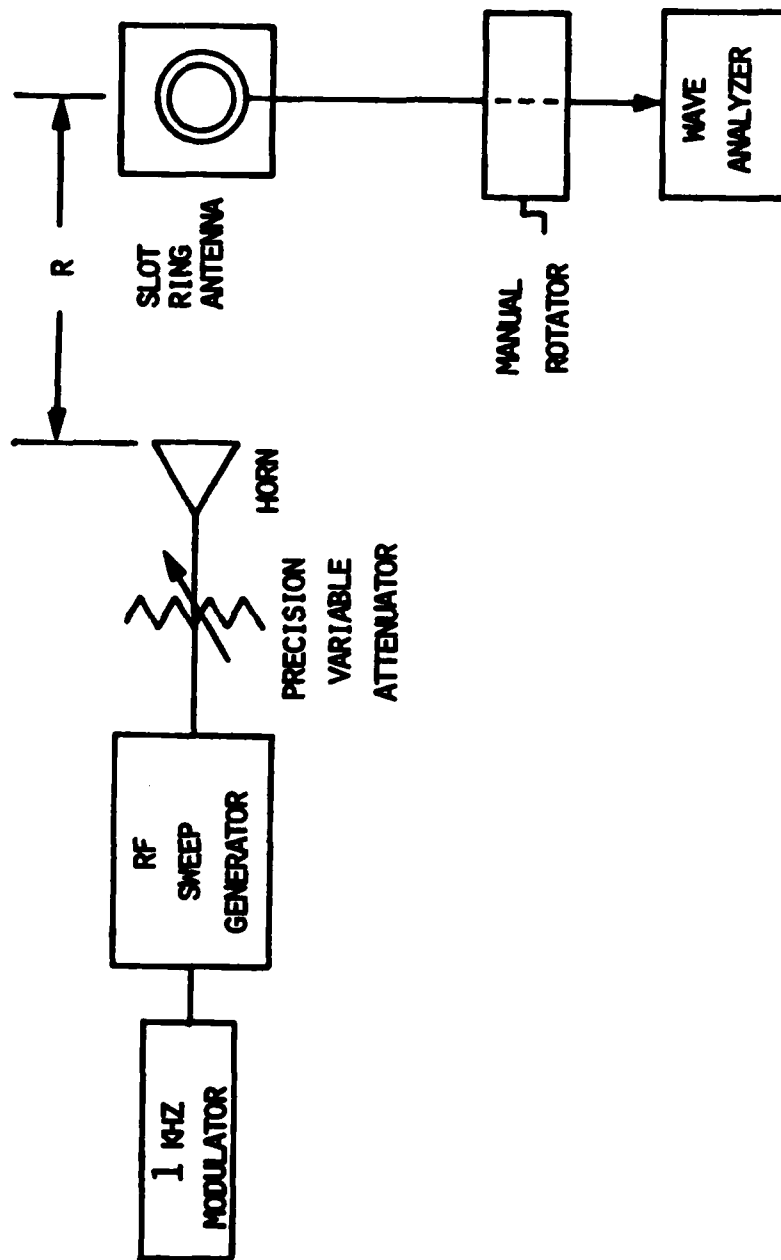


Fig. 3-1. Slot-ring antenna radiation pattern measurement apparatus.

shape can be distinguished, and for this purpose the E-plane radiation patterns at 8 through 12 GHz have been combined in Fig. 3-2. The very smooth, almost circular pattern at 8 GHz shifts gradually to a six-lobed pattern at 10 GHz, and an even rougher shape at 12 GHz. An effect which is clearer in the H-plane patterns is noticeable in these as well: as the frequency rises, the ratio of maximum intensity on the dielectric side to that on the metal side increases. Most planar antennas having a dielectric on only one side show this effect. The lower wave impedance on the dielectric side tends to "pull" currents toward it, increasing the radiation on that side.

The H-plane patterns (Fig. 3-3) show this current-pulling quite well. At 8 GHz, the intensity on opposite sides of the structure differs by only 1 dB, but at 10 GHz, the disparity has grown to 1.5 dB, and at 12 GHz the average difference is about 2.5 dB. Higher dielectric constants can cause even larger differences. These effects are predicted well by the theory developed in the last section, as we shall see now.

In Figs. 3-4 and 3-5, the measured 10 GHz patterns are compared to the patterns calculated from the full-wave analysis developed earlier. The measured H-plane pattern of Fig. 3-4 agrees fairly well with the theoretical prediction, except near the plane of the antenna. Since the theory assumes an infinite ground plane, this disagreement is not surprising, and in fact the measured fields are about 20 dB down at these angles. The observed difference between the dielectric and metal side intensities perpendicular to the antenna is slightly less than the calculated value of 2.2 dB.

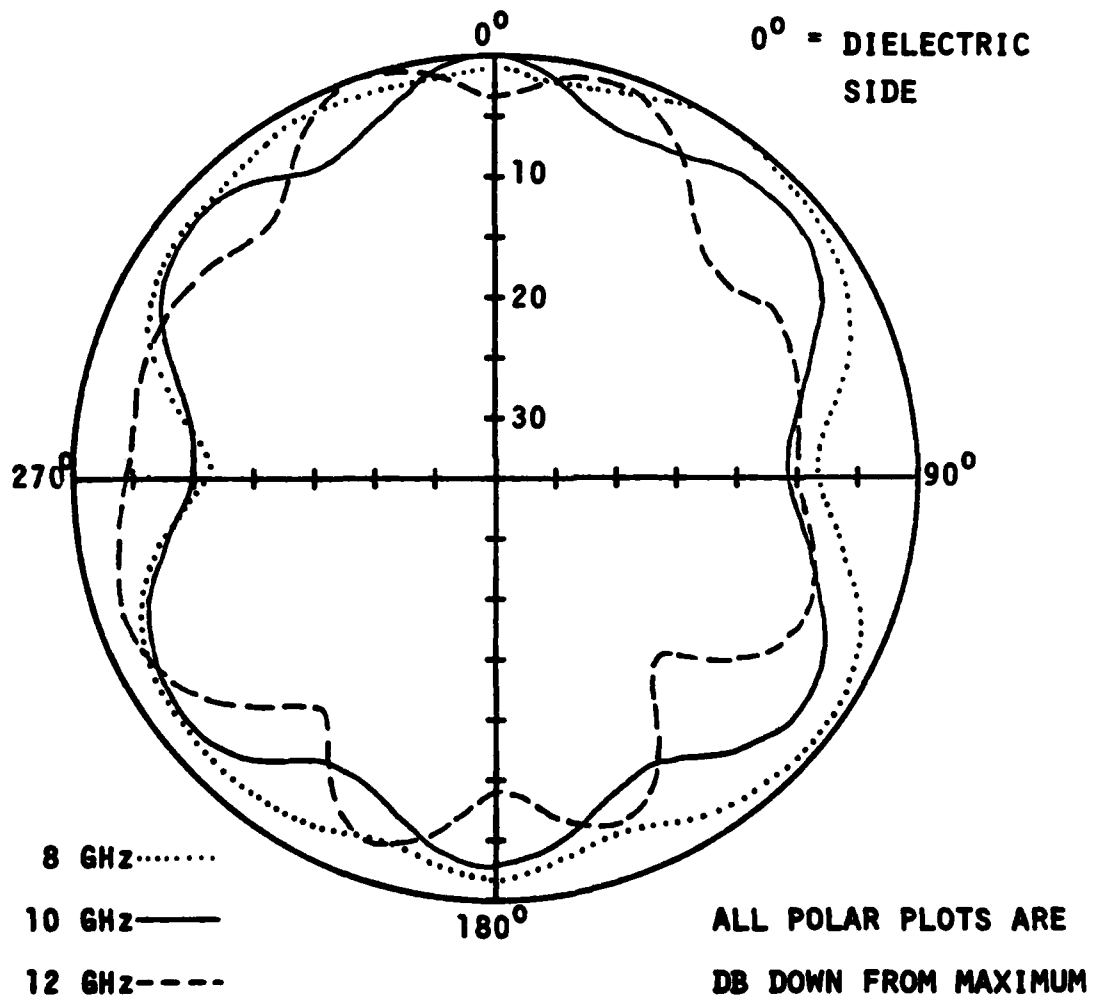


Fig. 3-2. Measured E-plane patterns of slot-ring antenna with frequency as parameter.

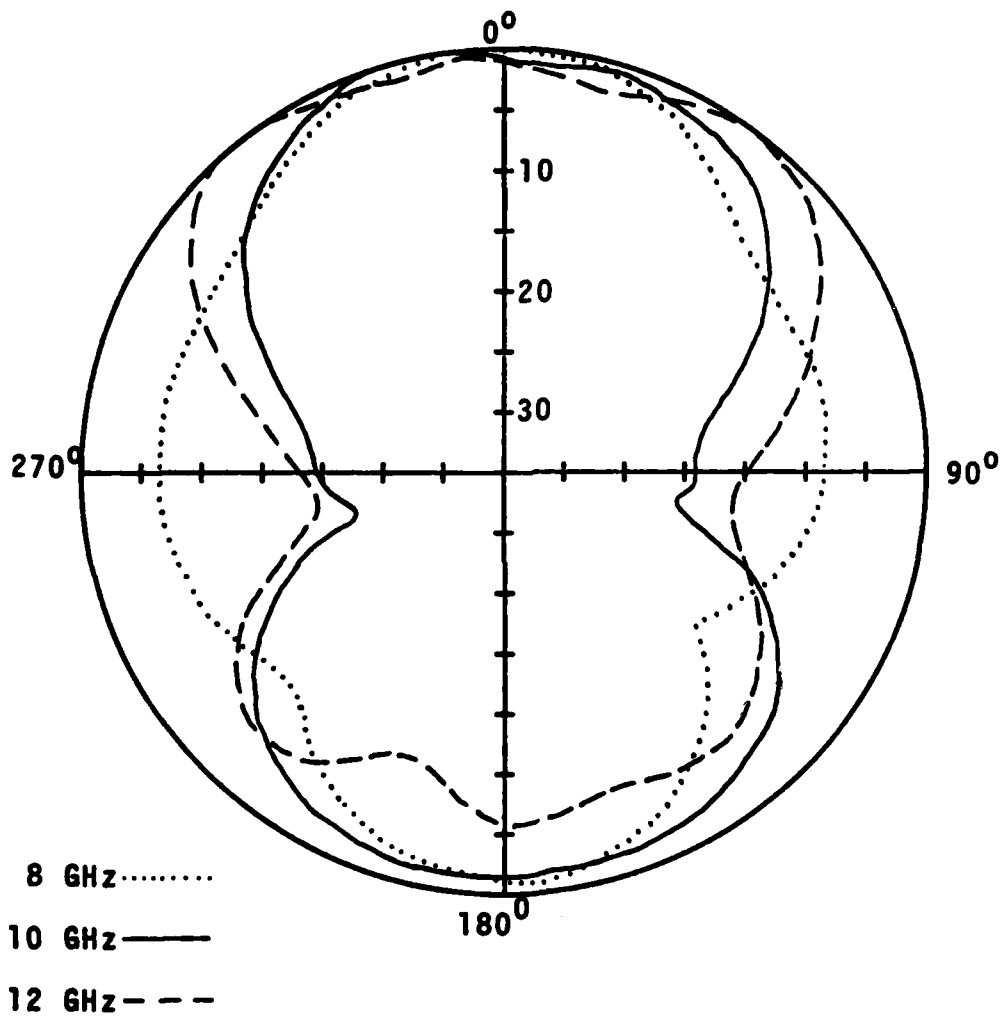


Fig. 3-3. Measured H-plane patterns of slot-ring antenna with frequency as parameter.

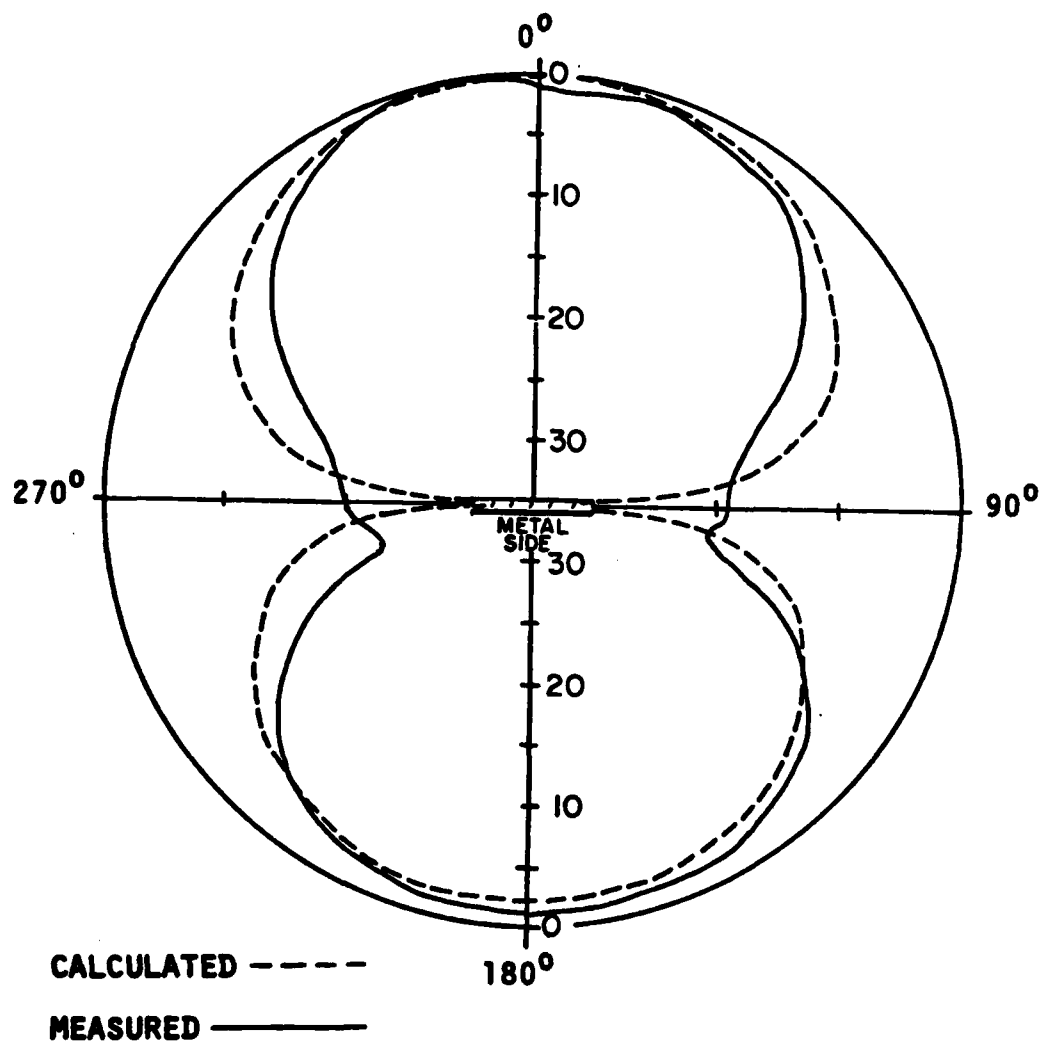


Fig. 3-4. Calculated and measured H-plane patterns of slot-ring antenna at 10 GHz.

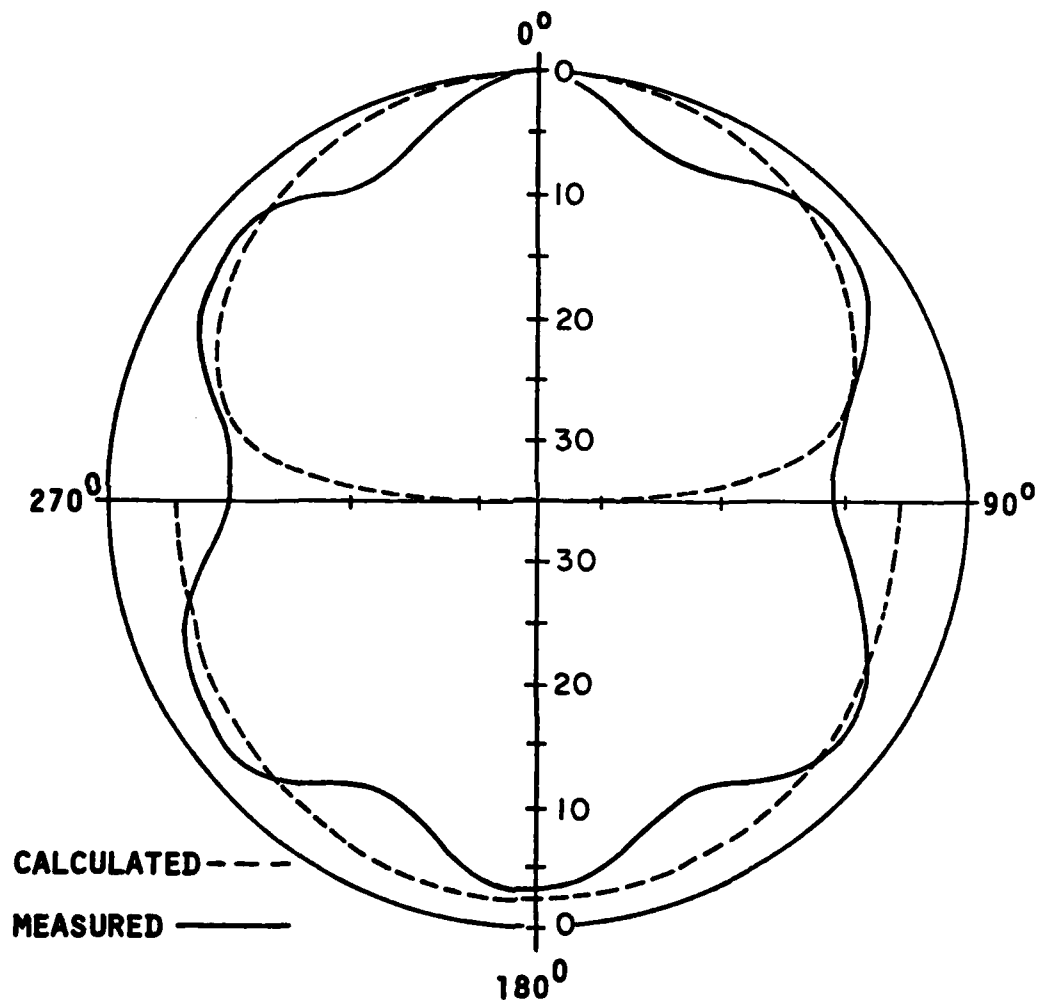


Fig. 3-5. Calculated and measured E-plane patterns of slot-ring antenna at 10 GHz.

The theoretical E-plane pattern shown along with the measured one in Fig. 3-5 requires some explanation. The apparent discontinuities at $\theta = 90^\circ$ and 270° are due to an ill-behaved term in the saddle-point equations given earlier. For any nonzero dielectric thickness t , the E_θ field goes to zero at $\theta = 90^\circ$. But if $t = 0$, a term causing the E-field cancellation at 90° goes to zero, and a finite field at $\theta = 90^\circ$ results. This is physically realizable since E_θ is perpendicular to the conductor, but the non-physical part of the theory arises from the assumption of an infinite ground plane. The edges of the finite dielectric and ground plane in the laboratory case cause diffracted waves that fill in the perfect nulls predicted by theory. Again, except for the region in the plane of the antenna, Fig. 3-5 shows good agreement between prediction and measurement.

MILLIMETER-WAVE PATTERN MEASUREMENTS

For completeness, some data taken in the millimeter-wave region will also be presented. Since no facilities for measuring power above 18 GHz were available at the time, no quantitative mixer data was taken, but the patterns obtained in this band are of practical interest. To simulate a GaAs substrate without incurring the expense of that material, we used a 300- μm sheet of alumina to form a millimeter-wave slot-ring antenna. The dielectric constant of alumina is not exactly the same as that of GaAs (9.6 versus about 13) but the effects observed on alumina will be similar to those encountered with a totally integrated GaAs structure.

We began the fabrication by forming small rings from 25- μm gold wire. Pressing these rings onto the alumina flattened the wire onto the surface to form evaporation masks. Vaporized gold was then deposited onto the substrate, and the rings were removed to reveal annular slots in the otherwise continuous 0.5 μm gold layer. The slot ring we chose to use was about 700 μm in diameter, and had a gap width of about 50 μm . Exact dimensions are given in Table II. Without an intervening chromium or palladium layer, adhesion of the gold to the smooth alumina substrate was very poor, but it was possible to mount one beam-lead diode (Hewlett-Packard type 5082-2264) across the gap without destroying the gold layer. Contact was made to the central disc by means of a spring-loaded gold wire made to touch the surface. The resulting antenna was not mechanically rugged, but proved stable enough to endure radiation pattern tests at 65.2 and 95.5 GHz.

Compared to the patterns at lower frequencies, the millimeter-wave data show even more current-pulling toward the dielectric side. The higher dielectric constant of about 9.6 for alumina also contributes to this effect. Fig. 3-6 compares the measured H-plane pattern at 65.2 GHz with the function calculated from theory. Since the substrate itself was a rectangle measuring about four by six wavelengths at this frequency, it is not surprising that some sidelobes appear in the measured pattern. Nevertheless the ratio of dielectric side to metal side radiation is predicted well, as are the nulls in the antenna plane.

The data taken by irradiating the same structure at 95.5 GHz are plotted in Fig. 3-7. At this frequency, Cohn's straight slot line

TABLE II
ALUMINA SLOT-RING ANTENNA DATA

Dielectric constant (relative)	9.6
Inner ring radius	0.0325 cm
Outer ring radius	0.0375 cm
Substrate thickness	0.03 cm
Calculated radiation resistance	413 Ω at 65.2 GHz
Substrate size	2.9 cm high 1.9 cm wide

Note: Circle at -27 dB indicates measurement limit below which data was extrapolated.

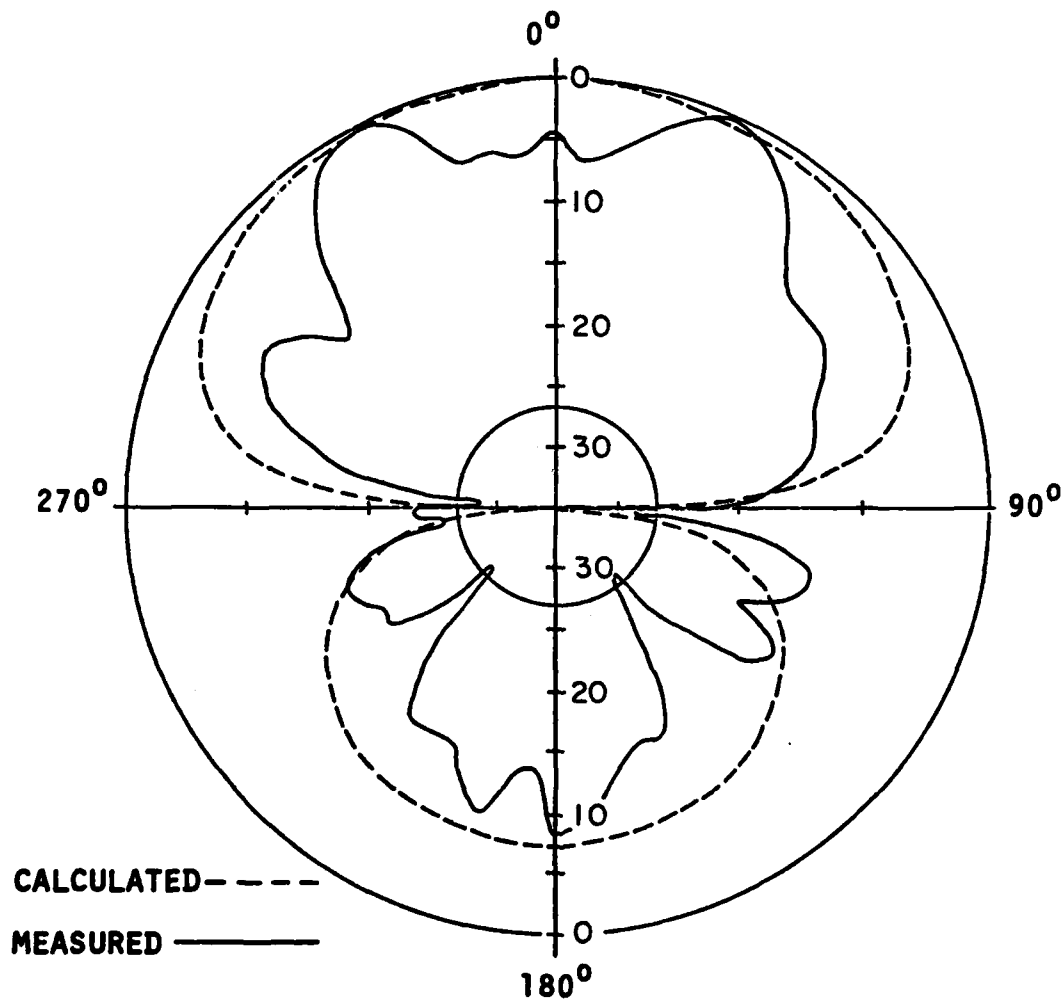


Fig. 3-6. Calculated and measured H-plane patterns of alumina slot-ring antenna, 65.2 GHz.

Note: Circle at -17 dB indicates measurement limit below which data was extrapolated.

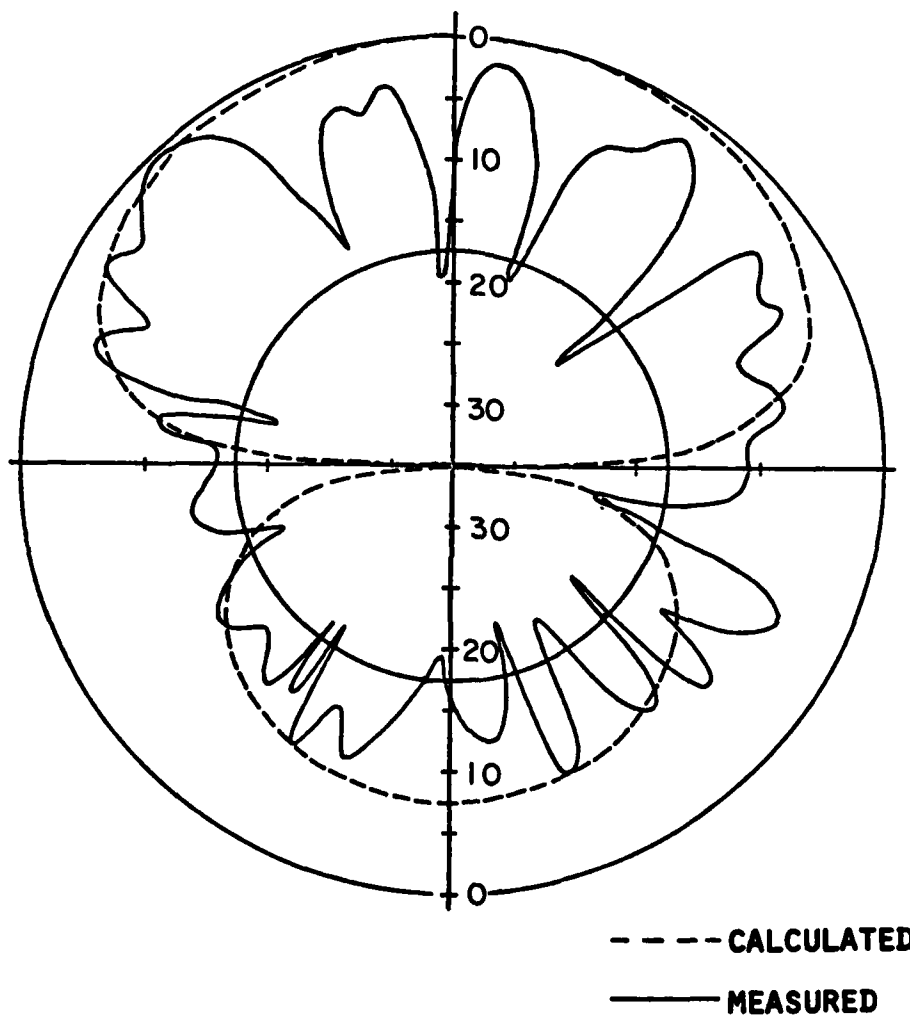


Fig. 3-7. Calculated and measured H-plane patterns of alumina slot-ring antenna, 95.5 GHz.

equations predict that the ring circumference is about 1.6 guide wavelengths, so the pattern can be expected to deviate from the simple first-order mode shape. As the plot shows, even more minor lobes arise at this frequency but the tendency for the dielectric side to give a higher average radiation intensity is still clear.

CHAPTER 4: MODES AND MODE ORTHOGONALITY

Up to now the discussion of the slot-ring antenna has centered exclusively on the first-order mode. This mode can actually exist in two degenerate, orthogonal forms, as we will now show.

The expressions satisfying Maxwell's equations and the boundary conditions for the slot-ring antenna all have one feature in common: their dependence on the longitudinal variable ϕ is of the form

$$f(\phi) = A \cos(n\phi) + j B \sin(n\phi) \quad (4-1)$$

where $n=0,1,2,3,\dots$ is the azimuthal order of the resonant mode. The independence of A and B means that for every $n > 0$, two independent and orthogonal modes exist. The electric fields in the slot for the first three modes are illustrated in Fig. 4-1. Only one mode exists for $n=0$, and it is circularly symmetric. For all higher n 's, the orthogonality of the sine and cosine functions means that, in principle, one mode may be excited without exciting the independent mode having the same azimuthal mode number. Modes of the same order are degenerate and have the same resonant frequency, which increases roughly proportional to n .

The existence of two degenerate, orthogonal first-order modes is a very useful property of the slot-ring antenna. It means that two orthogonally polarized waves can be transmitted or received independent-

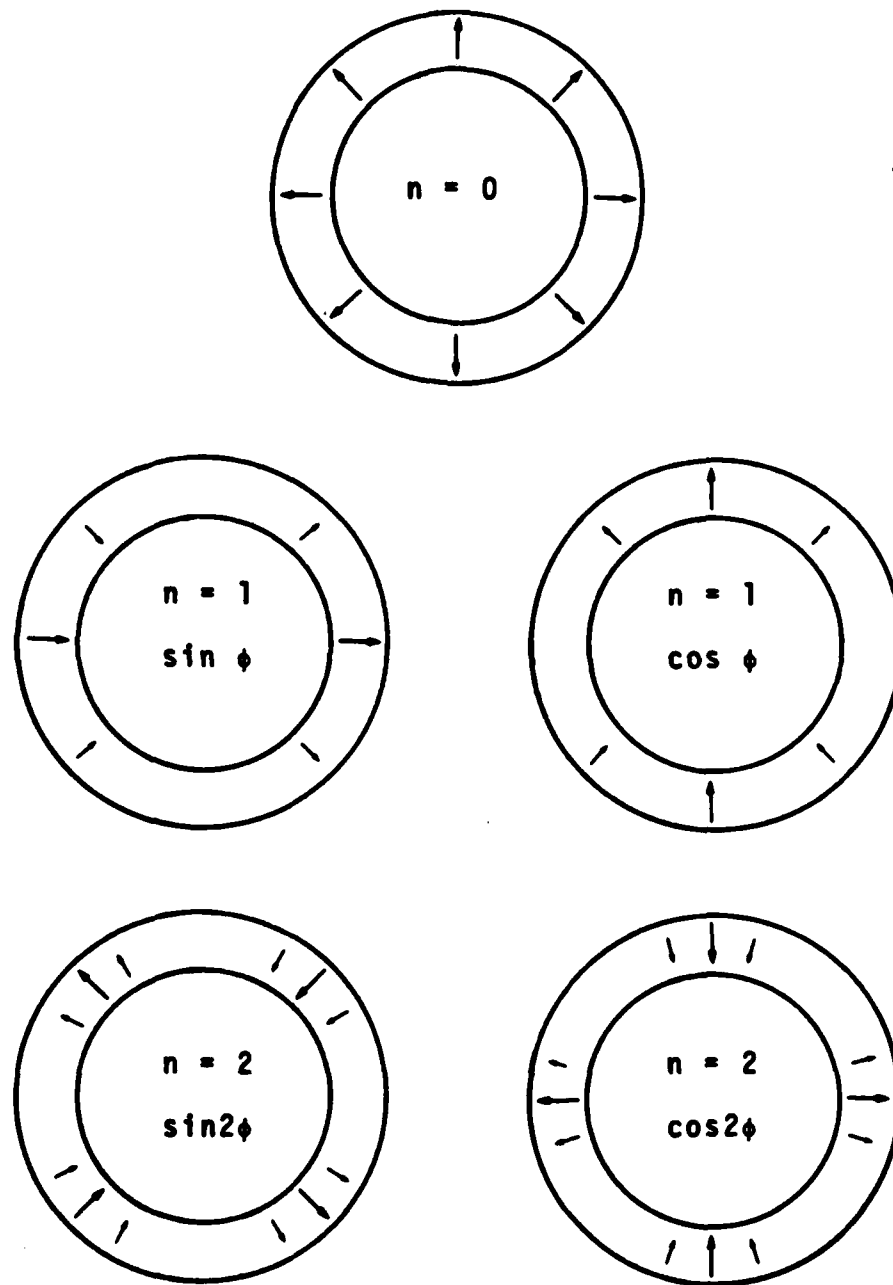


Fig. 4-1. First three modes of the slot-ring antenna.

ly of each other. For example, a horizontally polarized wave can be received at one pair of terminals while the same physical structure is used to receive a vertically polarized signal at another pair. Strictly speaking, to avoid exciting the $n = 0$ mode, the feed should be balanced as shown in Fig. 4-2(a). The voltage V_h is divided into two equal parts and couples only to the horizontally-polarized wave represented by E_x . Similarly, the balanced feed arrangement of V_v excites only vertically-polarized radiation. The $n = 0$ mode is not excited because the balanced feed ensures that the central disc as a whole is always at ground potential.

Using only one terminal pair per polarization, as in Fig. 4-2(b), simplifies the feed problem since it eliminates the necessity for balanced feeds. Although a single-ended feed excites the zero-order mode, this mode usually radiates poorly at the resonant frequency of the first-order mode. Even if zero-mode radiation occurs, symmetry considerations tell us that its radiation pattern must have a null along the Z-axis (perpendicular to the antenna). We will now show how the configuration in Fig. 4-2(b) can be used to create a single-balanced mixer.

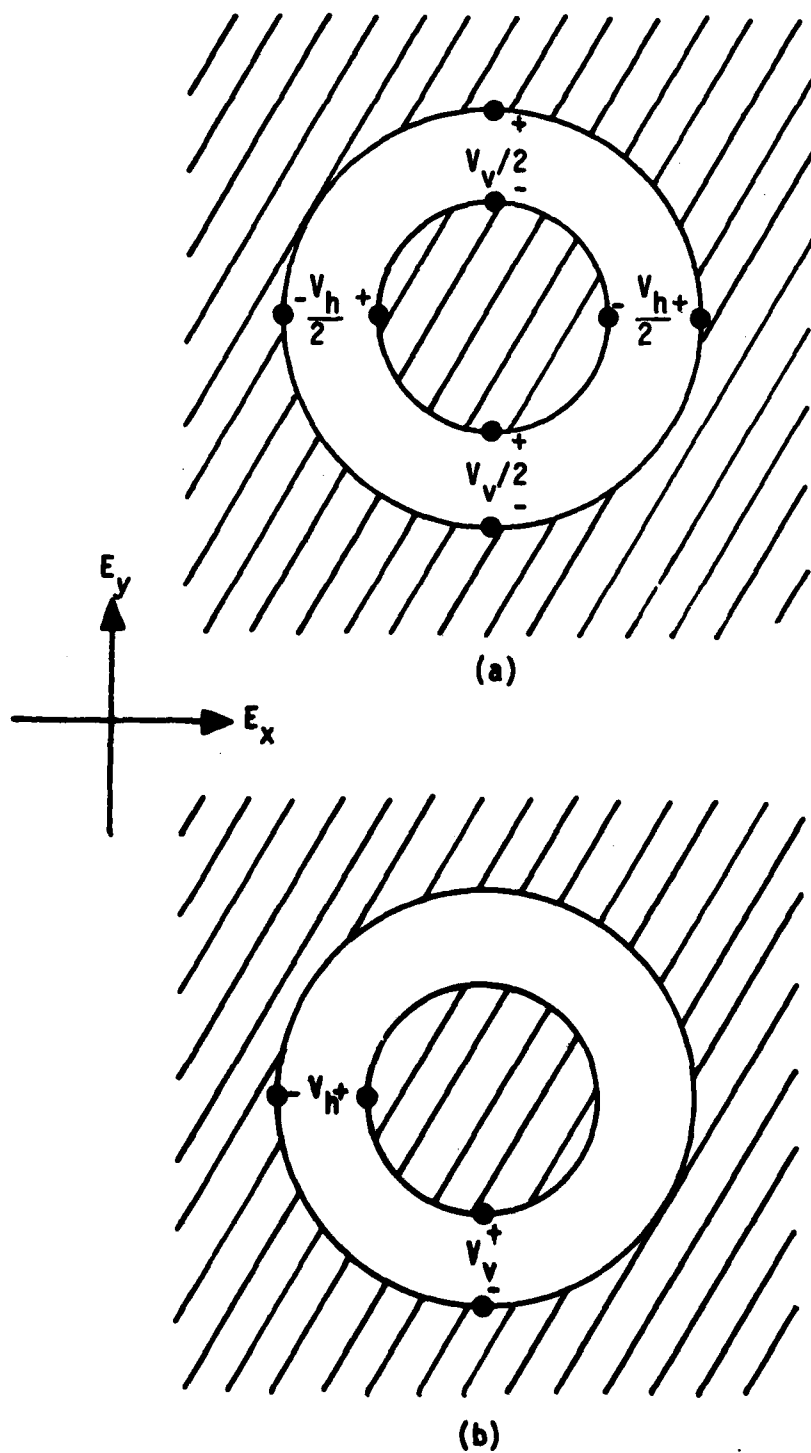


Fig. 4-2. Slot-ring antenna feeds: (a) balanced (b) unbalanced.

CHAPTER 5 : SLOT-RING MIXER THEORY

In this chapter, the area of nonlinear analysis known as mixer theory will be applied to the slot-ring mixer. Rather than attempting to predict mixer performance quantitatively, we will use the theory of mixers as a guide to improving performance criteria such as conversion loss.

By definition, a frequency converter or mixer is a nonlinear circuit. Therefore, the powerful tools of linear circuit theory must be applied with caution when dealing with mixers even though a practical small-signal model for a mixer usually can be found. While in a linear circuit analysis only one frequency at a time need be considered, a rigorous mixer analysis must consider more than just the incoming signal denoted here as the radio-frequency or RF signal. It must account for the effects produced when the RF signal encounters a continuously varying impedance changing at the local oscillator frequency rate f_{LO} . In general, this analysis involves all combinations of f_{RF} , f_{LO} , and all harmonics thereof. Fortunately for practical cases, taking only a few of the lower harmonics into account can lead to useful results as Held and Kerr have shown [1]. Both conversion loss and equivalent noise temperature can be predicted. Even though noise temperature is the more significant quantity in mixer applications, the following discussion will be limited to factors affecting conversion loss since noise temperatures were not measured.

APPROACHES TO MIXER ANALYSIS

Mixer analysis has been carried on at various levels of sophistication which are distinguished primarily by the complexity of the diode model used. Although some simple effects can be simulated by a zero-resistance switch opening and closing at the local oscillator frequency, most recent studies have included time-varying resistance and even capacitance effects. The basic one-diode mixer can be adequately simulated by the equivalent circuit in Fig. 5-1, regardless of the model.

The RF signal source is represented in this model by V_{RF} in series with a source impedance Z_s . In the mixer to be studied, Z_s is the terminal impedance of the antenna, and V_{RF} is proportional to the product of antenna gain in the direction of the incoming wave and the intensity of that wave. The input and output circuits serve to separate the intermediate-frequency (IF) signal from the RF signal, and to present the proper impedances to the diode. Note that the LO voltage appears nowhere in this model. Since its only function is to cause a periodic variation in the instantaneous impedance of the diode, it does not appear explicitly in Fig. 5-1. Since the LO voltage moves the parameters of the mixer back and forth like a child pumping a swing, the local oscillator voltage is sometimes called the pump voltage. The IF signal appears as a voltage V_{IF} across an IF load impedance Z_l . Both the RF and IF voltages are assumed to be purely sinusoidal.

Suppose the maximum power available from the RF source is defined as P_{RF} . This source is connected to a mixer whose power avail-

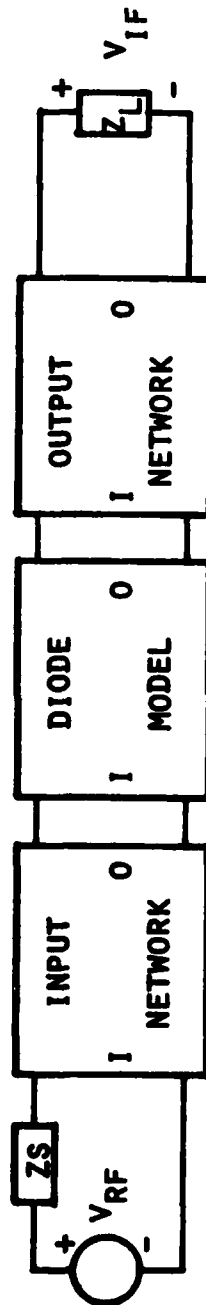


Fig. 5-1. Equivalent-circuit model of a general mixer.

able to the IF load is denoted P_{IF} . The conversion loss L of a mixer so defined is

$$L = P_{RF}/P_{IF} \quad (5-1)$$

Expressed in decibels,

$$L_{dB} = 10 \log_{10} (L) \quad (5-2)$$

Low conversion loss is normally associated with low noise temperature, so a lower L_{dB} generally means better mixer performance. To measure conversion loss experimentally, one must know both the power delivered to the IF load and the power available from the RF source. The IF power is usually easy to measure directly, but the direct measurement of RF input power may present problems, especially in the case of physically small antennas with terminals only a millimeter or so apart. These small dimensions often frustrate attempts to attach measuring equipment, and indirect means must be used to determine available input power. These means will be discussed later in detail.

All useful mixer diode models have at least one thing in common: one or more components whose parameters change periodically at the f_{LO} frequency rate. Fig. 5-2(a) shows the simplest diode model: an ideal switch that turns on and off in step with the LO voltage. This oversim-

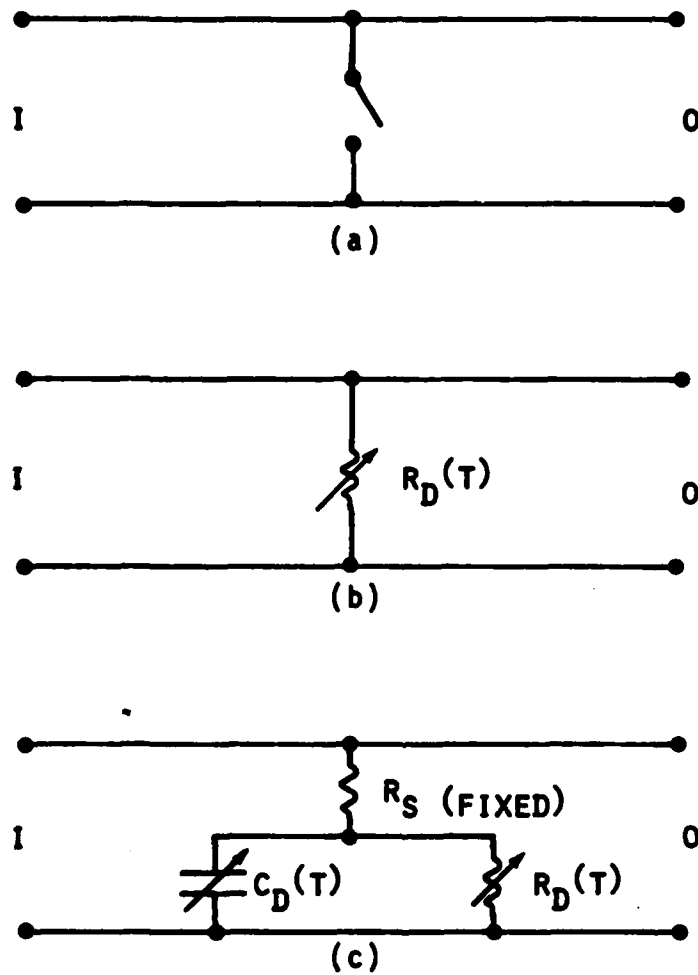


Fig. 5-2. Three diode models useful in mixer analysis:
 (a) ideal switch;
 (b) time-varying resistance;
 (c) time-varying resistance and capacitance .

plified circuit fails to account for internal diode losses and parasitic reactances. In Fig. 5-2(b) we find a model which Saleh [2] used to obtain results accounting for nonzero losses within the diode. Finally, quite realistic modeling is provided by the circuit in Fig. 5-2(c), used by Held and Kerr to simulate an actual 100 GHz mixer circuit successfully. In addition to the time-varying junction resistance $R_d(t)$ and capacitance $C_d(t)$, the parasitic spreading resistance R_s is included. This undesirable constant resistance dissipates power that could otherwise become useful IF output power. Its effects are relatively easy to calculate but hard to eliminate. Parasitic inductance normally associated with the diode package is not shown in this chip-level equivalent circuit.

The impedance presented to the diode by the parallel combination of the input and output circuits is called the embedding impedance. A rule of thumb states that the embedding impedance should conjugately match the diode impedance at the RF input and IF output frequencies for minimum conversion loss although even this simple criterion does not hold universally. Because of the harmonics generated in the nonlinear diode, the value of the embedding impedance at these harmonics is of critical importance to mixer operation as we show in the following simple example.

Consider an ideal diode connected across a voltage source V_{LO} :

$$V_{LO} = V \cos(\omega_{LO}t) \quad (5-3)$$

When we use the idealized I_d - V_d relation

$$I_d = I_s (e^{qV/kT} - 1) \quad (5-4)$$

and expand the exponential term, the resulting diode current is

$$I_d = I_s \sum_{n=1}^{\infty} (1/n!) \cdot [(qV/kT) \cdot \cos \omega_{LO}t]^n \quad (5-5)$$

The n th term in the infinite series has a component which is the n th harmonic of the local oscillator frequency ω_{LO} . In a practical circuit such as Fig. 5-1, these harmonic currents flowing through the input and output circuits create harmonic voltages which are functions of the embedding impedance at the respective harmonic frequency. When the input signal voltage is added to the situation, sums and differences $\pm f_{RF} \pm m f_{LO}$ ($-\infty < \text{integers } n, m < +\infty$) become significant and further complicate the picture. It is easy to see why the embedding impedance must be known over a very wide range of frequencies before it is even theoretically possible to predict mixer performance. Such impedance data covering many octaves is very difficult to obtain even when large scale models of mixer circuits are measured at lower frequencies. Because of these prob-

lems, it was decided that rather than attempting to predict the conversion loss of the mixer under study, mixer theory would be used qualitatively to guide certain design choices.

MIXER USING THE SLOT-RING ANTENNA

The simplest kind of mixer that can be made using a slot-ring antenna is the single-diode version shown in Fig. 5-3. Pump power is furnished to the diode by means of a local oscillator field E_{LO} irradiating the structure with the polarization shown. The input signal wave, represented by E_{RF} , arrives at the antenna with a polarization perpendicular to that of the local oscillator wave. This orientation increases the desirable isolation between the local oscillator and the RF input. Either the dielectric side of the antenna or the metal side may be used for either wave, but maximum gain results if the RF input illuminates the dielectric side.

The equivalent circuit of this simple mixer is shown in Fig. 5-4. The components of the RF and LO electric field vectors parallel to the diode produce voltages V_{RF} and V_{LO} proportional to their respective intensities. These voltages appear in series with each other and with a radiation resistance $R_{rad}(\omega)$, which is a function of frequency. The transmission lines above and below the diode represent the reactive part of the antenna's impedance which is well-modelled by these elements.

Assuming $V_{LO} \gg V_{RF}$, the diode's instantaneous impedance changes periodically at the local oscillator frequency rate. A portion of the RF

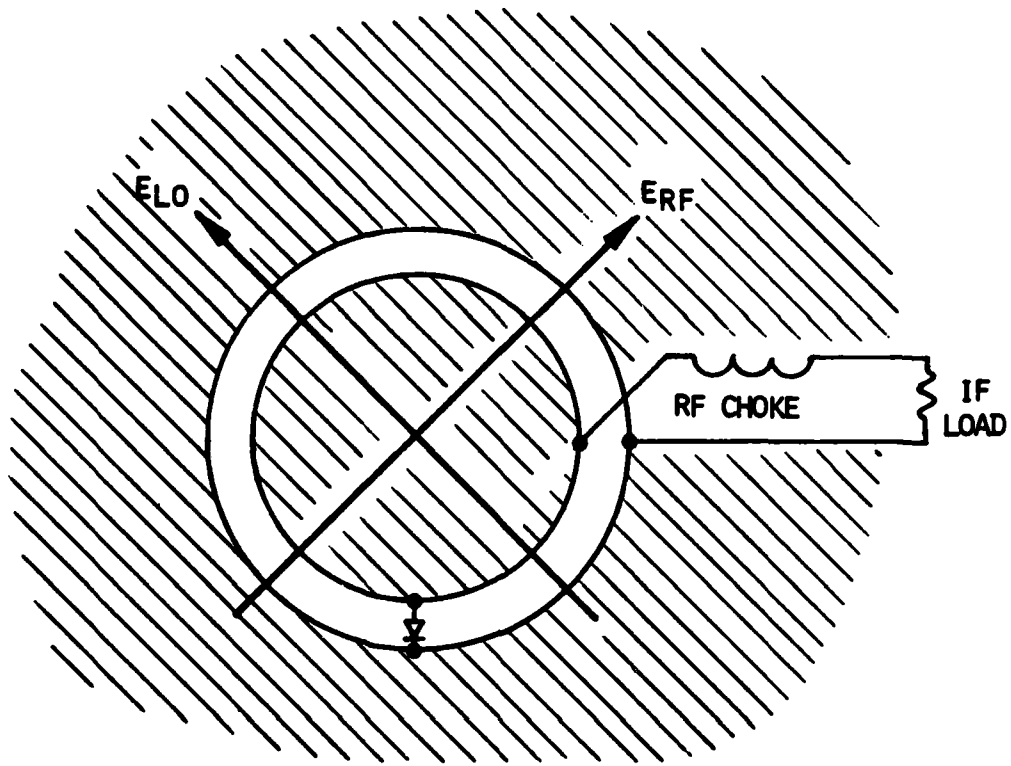


Fig. 5-3. Single-diode slot-ring mixer.

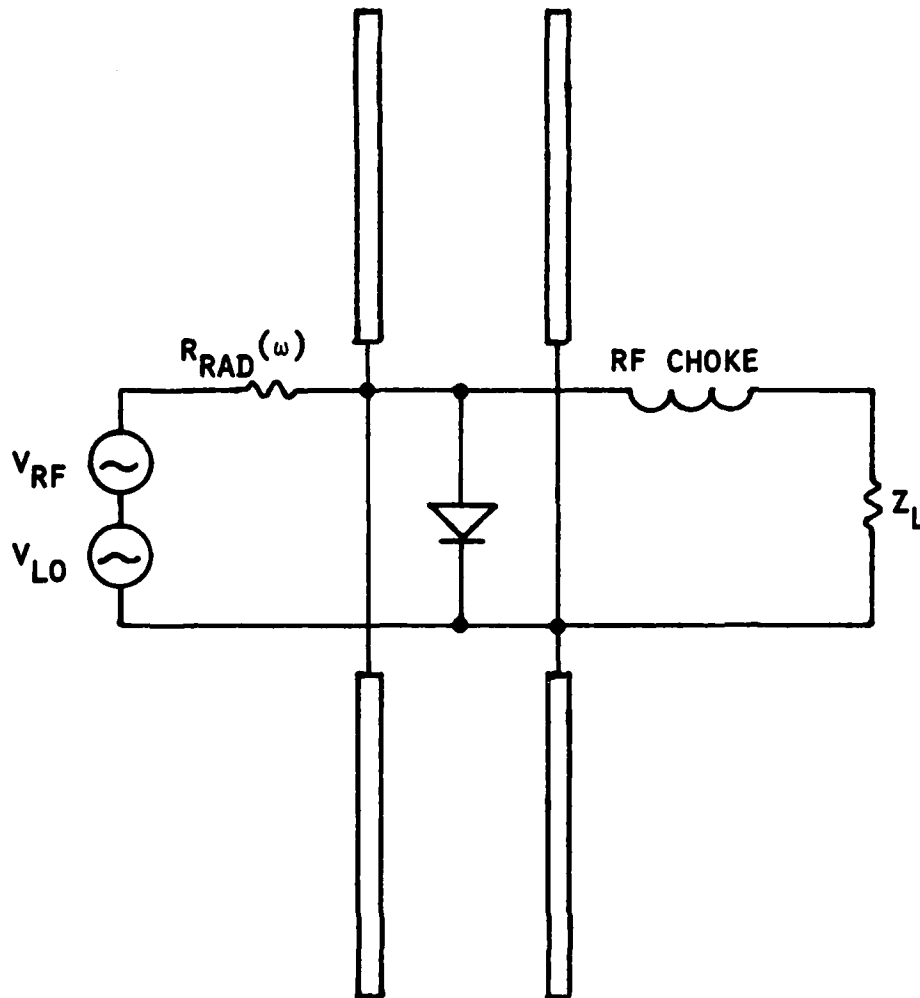


Fig. 5-4. Equivalent circuit of single-diode slot-ring mixer.

input power is converted to a much lower IF frequency, and appears across the IF load resistance Z_1 .

The following factors are especially important in designing the mixer to give an acceptably low conversion loss:

- (a) RF and LO source impedance
- (b) Diode characteristics
- (c) IF load impedance
- (d) Embedding impedance at harmonics

Each factor will now be discussed in turn.

(a) RF and LO source impedance

Because the antenna is a relatively low-Q device, its radiation impedance changes rather slowly with frequency. This means that if f_{IF} is less than 10% of f_{RF} , the impedance seen by the diode at the RF and LO frequencies will be roughly the same. The correct antenna diameter will ensure that this impedance will be substantially real, and in the neighborhood of 200-300 ohms for practical gap dimensions formed on low-dielectric-constant substrates. As long as the gap is less than ~20% of the ring diameter, its width has relatively little effect on the radiation resistance, although higher dielectric constants and thicker substrates lead to a resistance in the 500-600 ohm region.

For efficient diode pumping the antenna impedance should be the complex conjugate of the large-signal diode impedance at the pump frequency. The object of pumping is to vary the dynamic resistance as much as possible for a given LO power intensity. Maximum power transfer to the diode achieves this goal. It is here that the extreme simplicity of

the slot-ring antenna works as a drawback. A coaxial transmission line mixer can be tuned by series or shunt stubs for a good match to the diode. Adding such an impedance-matching network to the slot-ring antenna might be feasible, but in the absence of precise large-signal diode impedance data it was decided that such techniques would be a needless complication in a first attempt. Accordingly, whatever mismatch was present between the antenna terminal impedance and the mixer diode was accepted as inherent in the structure. Later we discuss the technique of using a reflecting polarization grid behind the antenna, which can be viewed as a form of impedance-matching adjustment.

The same lack of tuning adjustments affects the RF impedance matching problem as well. At a given LO drive level, there exists a certain RF source impedance which will give lowest conversion loss. Again, the approach taken was to design for an approximately real impedance of about 200 ohms to be presented to the mixer diode, and this choice did in fact give an acceptably low conversion loss figure.

(b) Diode Characteristics

An ideal exponential diode follows the I_d - V_d relationship given in Equation (5-4) above. A real diode can be modelled as an ideal diode embedded in an R-C circuit, as shown in Fig. 5-5. The junction capacitance C_j is unavoidable since it is a consequence of the way a semiconductor diode works. Its susceptance could be tuned out by a shunt inductance were it not for the presence of the spreading resistance R_s . This series resistance arising from the finite conductivity of the semiconductor itself dissipates power whenever current flows through it.

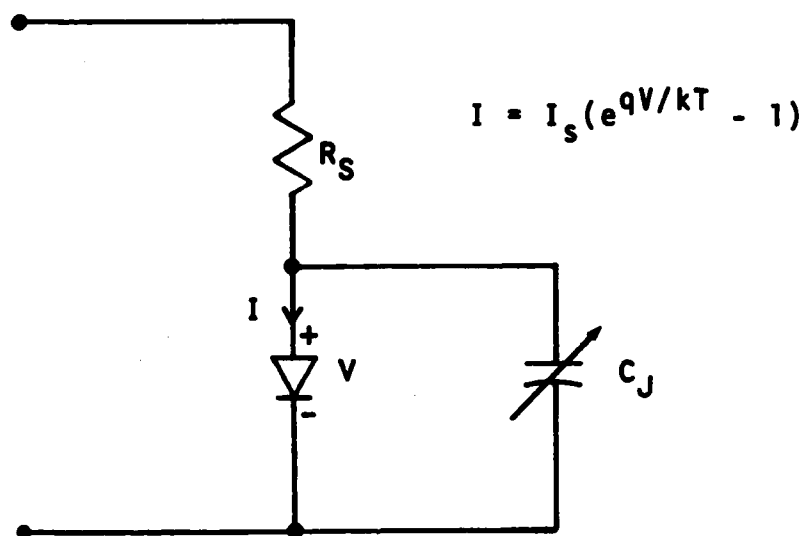


Fig. 5-5. Ideal diode with junction capacitance C_J and spreading resistance R_S .

Both RF and IF currents must pass through R_s in a mixer circuit, so it can cause substantial losses of both incoming RF power and outgoing IF power.

Held and Kerr [3] have quantified this problem by separating the overall conversion loss of a mixer into three loss components:

$$L = K_0 L' K_1 \quad (5-6)$$

where L' is the conversion loss of the intrinsic mixer with no series resistance, K_0 is the loss in the series resistance at f_{IF} , and K_1 is the series resistance loss at f_{RF} . Let Z_s and Z_1 be the RF source and IF load impedances, respectively. In general, the series resistance is a function of frequency $R_s(f)$. Held and Kerr showed that K_0 and K_1 were given by:

$$K_0 = \frac{\text{Re}[Z_1 + R_s(f_{IF})]}{\text{Re}[Z_1]} \quad (5-7)$$

and

$$K_1 = \frac{\text{Re}[Z_s + R_s(f_{RF})]}{\text{Re}[Z_s]} \quad (5-8)$$

Obviously, the higher the series resistance at the RF and IF frequencies, the higher the loss. Diodes with both high and low values of R_s were tested in the mixer to be described. The change in R_s contributed to an 11 dB improvement in conversion loss.

When the series resistance is nonzero, a cutoff frequency f_{co} can be defined for the diode:

$$f_{co} = 1/(2\pi R_s C_j) \quad (5-9)$$

Above this frequency the junction capacitance has such a low reactance that most of the available input voltage appears across R_s and is dissipated uselessly. Long before this condition is reached, however, mixer performance has begun to degrade. For this reason, low junction capacitance ranks with low series resistance as an important parameter in mixer diodes. The series inductance and shunt capacitance of the diode's mounting enclosure, called package parasitics, can also have detrimental effects, but the diodes used in these experiments had sufficiently low parasitics at X-band that no special precaution was taken to compensate for them.

(c) IF circuitry

The relatively low IF frequency allows more flexibility in the design of the network which couples the desired IF output to a load impedance. A lowpass filter is usually provided at the diode to present a reactive impedance at f_{RF} and f_{LO} , preventing loss of energy to the out-

put circuit. The exact nature of the lowpass filter is determined by the desired IF bandwidth, which can extend from 0 to 10 GHz or more in millimeter-wave mixers. Design of such filters is complicated by the diode's impedance change with frequency although for narrow IF bandwidths this effect is insignificant. A conjugate match to the diode's IF impedance is the goal here, and linear circuit theory can be used with confidence.

The mixer built in the course of these experiments was designed for a single-frequency IF of 10 MHz, permitting the use of a simple lumped-element matching network, with no concern for broadband response. Designs for broader IF bandwidths will need more sophisticated IF circuitry, but such networks are entirely conventional at this time and will not be discussed further.

(d) Embedding impedance at harmonics

In the absence of extensive measurements, nothing can be said with certainty about the exact nature of the slot-ring antenna terminal impedance at frequencies much above the first-order mode resonance. To the extent that the transmission-line model of Fig. 5-4 holds at higher frequencies, one would expect a series of alternating poles and zeroes at the resonances of the higher-order modes. These resonances are not related by the simple integer factors of the TEM transmission line case since slot line is a dispersive waveguiding structure.

It is fairly safe to assume that the embedding impedance is primarily reactive because the higher-order resonances show progressively higher radiation Q's as Kawano and Tomimuro showed both experimentally and theoretically [4]. This is good since Saleh showed [5] that mixers

whose harmonics are terminated in a reactive load are capable of lower conversion loss than those which have a broadband resistive termination. For extremely high frequencies at which the gap is an appreciable fraction of a wavelength the terminal impedance will again show a substantial real part. In practical mixers this region is ten to twenty times the operating frequency, and diode imperfections will dominate the loss mechanism long before then.

CHAPTER 6: SLOT RING MIXER EXPERIMENTS

In this section, the indirect technique chosen for measuring conversion loss is described. This technique was used in the experiments described which determined conversion loss of the isolated structure. Discussion of quasi-optical techniques which enhance mixer performance are deferred to Chapter 7.

CONVERSION LOSS MEASUREMENT TECHNIQUE

We begin with the definition of mixer conversion loss from Equation (5-1). As mentioned earlier, the output power P_{IF} is easy to measure since it requires no alteration of the mixer. This output power can be measured directly by inserting a power meter at point B in Fig. 6-1(a), or point C in Fig. 6-1(b). A conventional mixer can be treated as a two-port device allowing the RF power available at the input port to be determined by direct measurement at point A in Fig. 6-1(a).

In the case of a quasi-optical mixer, however, this method fails. An antenna does not have a clearly defined input port in the sense of a single traveling-wave mode whose magnitude is characterized by a scalar electric or magnetic field amplitude. Instead, its input is a wave which propagates in the general direction of the antenna but whose exact description and direction is unknown. To simplify the problem we

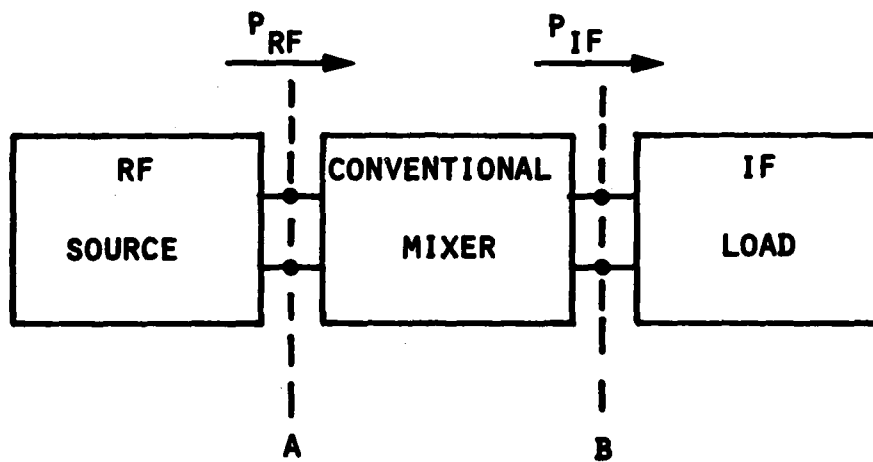
will assume the incoming radiation to be a plane wave whose direction of travel is coincident with the antenna's direction of maximum response. For an ideal slot-ring antenna this direction is the Z-axis perpendicular to the dielectric side of the antenna. A perfectly plane wave is a mathematical abstraction requiring infinite power, but it does have a well-defined intensity measured in power per unit area. In Fig. 6-1(b), this intensity is denoted by I_{RF} , and it is defined at plane P, the antenna location.

Establishing an approximate plane wave over a limited region in the laboratory is a simple matter. If D denotes the largest dimension of the transmitting antenna's aperture and λ is the free-space wavelength, the region known as the far field of the antenna begins at a distance $2D^2/\lambda$. Beyond this point, negligible error is caused by assuming the diverging spherical wave front is planar.

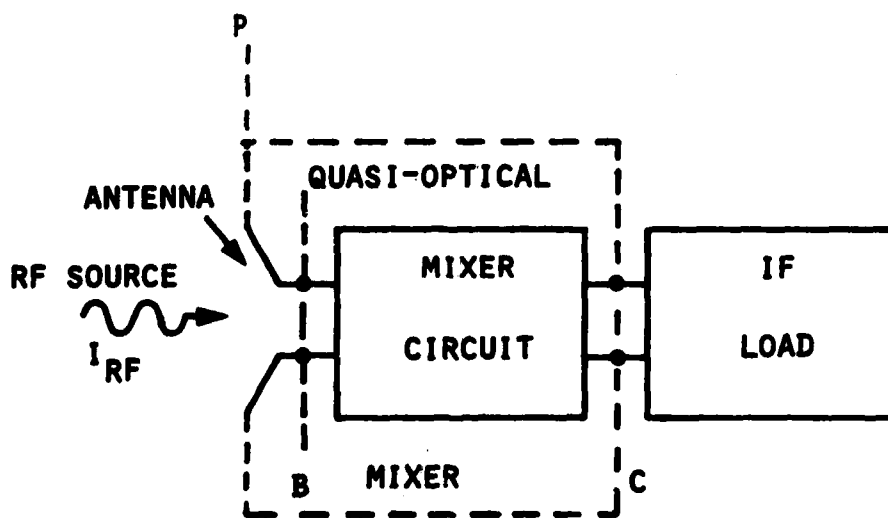
The ratio of the power P_{max} available at a lossless antenna's terminals to the incoming wave's radiation intensity I_{RF} is called the maximum effective aperture A_{em} :

$$A_{em} = P_{max}/I_{RF} \quad (6-1)$$

If I_{RF} and A_{em} can be determined, the available output power P_{max} can be found by means of Equation (6-1). Once P_{max} is found by this indirect method, the conversion loss of the diode and associated circuitry can be found using the same method that was applied to the conventional mixer in



(a)



(b)

Fig. 6-1. Comparison of (a) conventional and (b) quasi-optical mixers.

Fig. 6-1(a).

The definition of maximum effective aperture A_{em} assumes there are no losses in the antenna materials and that the antenna drives a conjugately matched load impedance. The quantity A_{em} is related to the directivity D by the effective aperture of an isotropic source:

$$A_{em} = (\lambda^2/4\pi) \cdot D \quad (6-2)$$

Kraus defines directivity in a given direction to be the ratio of radiation intensity U_d in that direction to the average intensity U_o :

$$D = U_d/U_o \quad (6-3)$$

If the equivalent intensity at unit distance is defined to be a function of angular position $U(\phi, \theta)$ then the total power W radiated is found by integrating this function over the unit sphere:

$$W = \int \int_{\text{SPHERE}} U(\theta, \phi) d\Omega \quad (6-4)$$

From this total power, average intensity U_o on the sphere can be found by dividing the total power by the area of the unit sphere:

$$U_0 = W/4\pi \quad (6-5)$$

Therefore, by measuring only the relative radiation intensity function $U(\phi, \theta)$ we can find the maximum effective aperture from Equations (6-2), (6-3), (6-4), and (6-5):

$$A_{em} = (\lambda^2 U_d)/W \quad (6-6)$$

In practice, the measurement of intensity can be performed at any distance in the far field, since the $1/r^2$ term will appear in both numerator and denominator of Equation (6-6).

Spherical integration of a power pattern can only be approximated in the laboratory since in principle the intensity at each infinitesimal solid angle must be measured. With a single-axis antenna positioner this would require an infinite set of polar patterns. Fortunately symmetries of the slot-ring antenna reduce the number of patterns required to only two: namely, the E-plane and H-plane patterns already discussed. The following discussion shows why this is so.

In the full-wave analysis in the appendices it is shown that the far-field radiation pattern functions for the first-order mode are separable into functions of r , θ , and ϕ :

$$E_{\theta}(r, \theta, \phi) = (1/r) \cdot e^{j(\phi - k_0 r)} \cdot F_{\theta}(\theta) \quad (6-7)$$

$$E_{\phi}(r, \theta, \phi) = (1/r) \cdot e^{j(\phi - k_0 r)} \cdot F_{\phi}(\theta) \quad (6-8)$$

At a fixed distance r , the problem reduces to that of finding the separate functions F_{ϕ} and F_{θ} . The double integration of a separable function reduces to two single integrals. Since in our case $F(\phi)$ is the harmonic function $\exp(j\phi)$, its integration is simple. The remaining integral with respect to θ was performed numerically using the functions $F_{\theta}(\theta)$ and $F_{\phi}(\theta)$ obtained from the pattern measurements. The cross-polarized intensities were low enough to contribute an insignificant amount to the integral and were therefore neglected. The resulting maximum directivity on the dielectric side of the antenna was thus found to be 5.5 dB. As mentioned earlier, this directivity will be numerically equal to antenna gain only for a lossless, perfectly matched structure. Actual antenna gain will always be less than this maximum since gain is related to directivity by antenna efficiency, which is always less than unity. The method we use here to measure conversion loss combines antenna losses and mismatches with the mixer circuit losses to give one overall figure for the complete system.

CONVERSION LOSS EXPERIMENTS

Once antenna patterns were obtained we constructed a single-balanced mixer using two Aertech A2S250 diodes. By feeding out-of-phase RF voltages to two single-diode mixers in parallel and reversing the polarity of one diode, the IF outputs add in phase. This balanced mode of operation cancels any incidental amplitude modulation on the local oscillator signal in addition to reducing certain other spurious responses. The basic operation of the mixer in a balanced, polarization-duplexed mode is illustrated in Fig. 6-2. In the figure the RF signal arrives as a horizontally polarized plane wave incident perpendicular to the antenna, on the dielectric side. The LO signal is vertically polarized, and can arrive from either side of the structure. The vectors E_{RF} and E_{LO} show the electric fields on the antenna plane. By resolving each vector into two perpendicular components, it is easy for one to see that mixer diode D1 receives $(V_{LO} - V_{RF})/\sqrt{2}$, while D2 receives $(V_{LO} + V_{RF})/\sqrt{2}$. In effect, each diode has its own independent mixer circuit, with the IF outputs added in parallel. The IF signal appears as a voltage between the central metal disc and the surrounding ground plane, and is removed through an RF choke. A double-balanced mixer with improved isolation between ports can be made by adding two additional diodes D3 and D4, as indicated.

The center conductor of the coaxial IF cable contacts the central disc directly. This connection was made to simulate an RF choke by terminating the far end of the cable with an adjustable reactive termi-

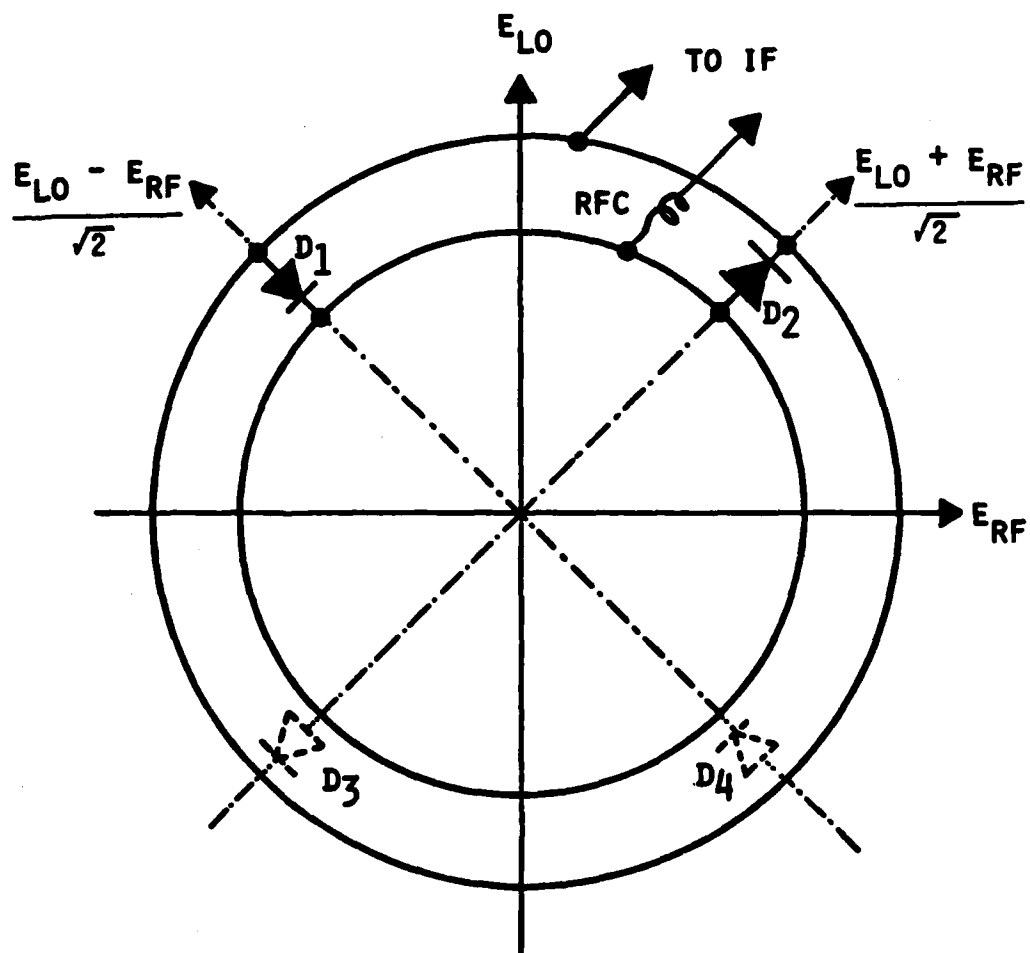


Fig. 6-2. Two-diode balanced slot-ring mixer showing diode input voltages.

nation, specifically a coax-to-waveguide transition facing a sliding short. Proper placement of the short caused a current node to appear at the end of the cable connected to the disc. This adjustment simulated a high-impedance choke at the RF frequency. Although this technique seemed to work fairly well, it was replaced in later experiments with a conventional choke at the antenna itself.

Fig. 6-3 shows the apparatus used in determining conversion loss. A coaxial bypass capacitor at the coax-to-waveguide transition passed the 10 MHz IF signal without disturbing the microwave energy, to which the bypass capacitor appeared as a short to the waveguide wall. The capacitor's 260 pF was included in the input side of a 10 MHz pi-network matching circuit diagrammed in Fig. 6-4. This network could be adjusted to transform real impedances of 100 to 500 ohms to the 50-ohm level required by the spectrum analyzer IF load.

To create a known field strength at the RF frequency, we directed the output of a Gunn-diode oscillator through an isolator and attenuator to a high-gain horn. To measure the radiation intensity from this source, the mixer under test was momentarily replaced by another horn of known gain and the received RF power measured. Dividing this power by the effective aperture of the receiving horn gave the radiation intensity at the mixer location directly. The distance R_1 between the RF horn and the mixer was 183 cm, well into the far field.

Providing enough local oscillator power to a quasi-optical mixer without unduly disturbing the mixer's radiation pattern requires a compromise. The local oscillator energy in this test came from a horn

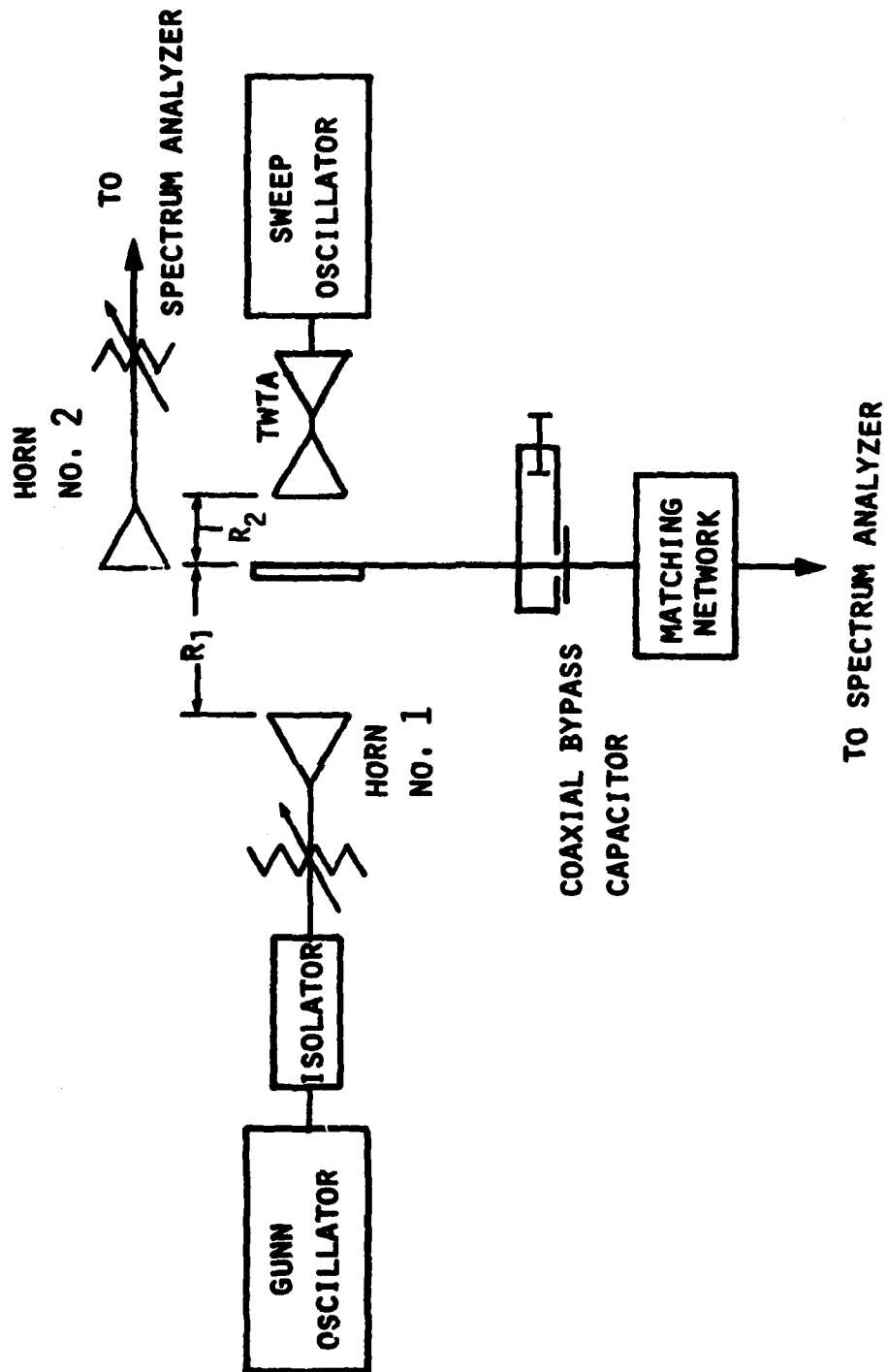


Fig. 6-3. Slot-ring mixer conversion loss measurement apparatus.

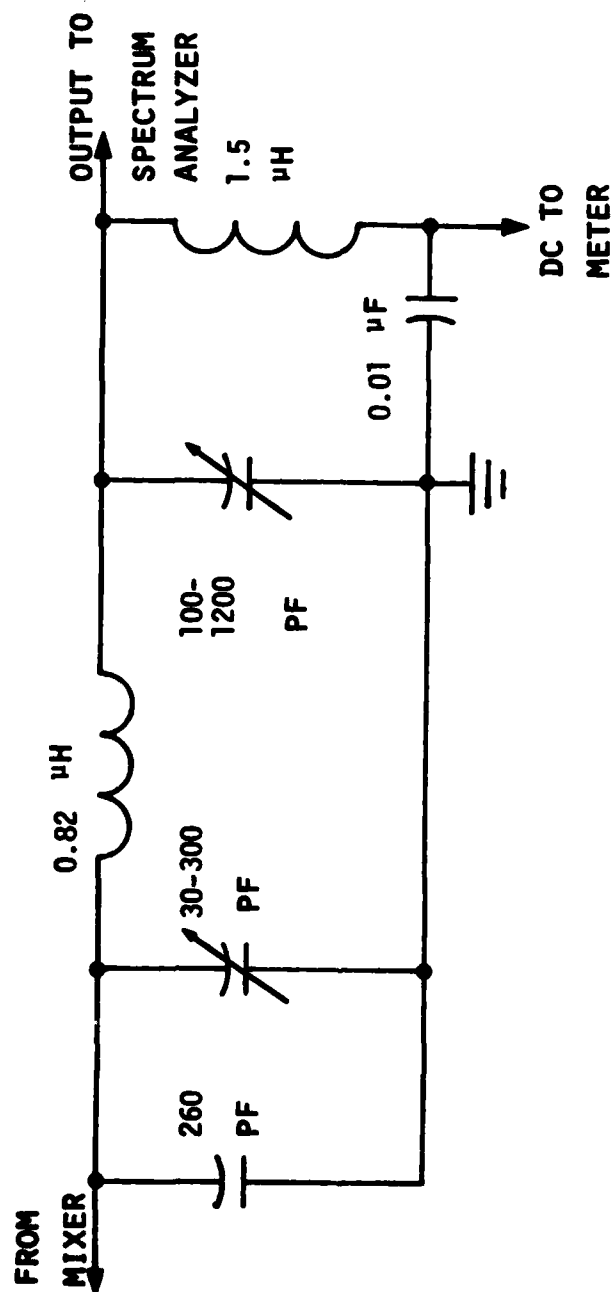


Fig. 6-4. Matching network for 10 MHz IF.

mounted directly behind the mixer that illuminated the metal side. Since the mixer ground plane was relatively small and some incoming RF radiation penetrated through the antenna slot, a substantial RF field was present behind the mixer. If the LO feed horn was brought too close, reflected RF power caused an oscillation in the IF output power as the reflected wave added first in and then out of phase with the incident wave. This effect decreased with increased R2 while too large a distance lowered the available LO power below the optimum value and conversion loss increased rapidly. A compromise distance of $R2 = 25$ cm allowed sufficient LO drive without altering the free-space radiation pattern of the antenna excessively.

Once the LO power was applied, its frequency was adjusted to produce an IF of 10 MHz. The IF output power was measured with a spectrum analyzer calibrated with the same power meter used for the RF power measurements. Using the same instrument for both RF and IF power measurements ensured that the critical power ratio yielding the conversion loss depended only on the accuracy of the meter's relative calibration and not upon the absolute accuracy of two different instruments.

Initial results were somewhat discouraging. The calculations involved in finding the conversion loss are shown in Table III. The figures are averages taken from two trials. The conversion loss of 17.4 ± 2.1 dB was much higher than the 5 to 7 dB typical of commercial practice. The reason for this high loss was found to be the excessively high series resistance of the Aertech diodes used.

Modern microwave diodes can be optimized for a certain type of

TABLE III
SLOT-RING MIXER CONVERSION LOSS
CALCULATIONS

	Average of Two Trials	Estimated Error
RF power received at Horn #2	= -22.6 dBm	± 0.3 dB
<u>-(Horn #2 gain over slot ring</u>	<u>= 14.5 dB)</u>	<u>± 1.5 dB</u>
= P _{RF} available from slot ring	= -37.1 dBm	± 1.8 dB
P _{RF} available from slot ring	= -37.1 dBm	± 1.8 dB
<u>-(P_{IF} measured at mixer output</u>	<u>= -54.5 dBm)</u>	<u>± 0.3 dB</u>
= L _{dB} with Aertech diodes	= 17.4 dB	± 2.1 dB
L _{dB} with Aertech diodes	= 17.4 dB	± 2.1 dB
<u>-(Improvement obtained by</u>		
<u>substituting NEC diodes</u>	<u>= 10.9 dB)</u>	<u>± 1.0 dB</u>
= L _{dB} with NEC diodes	= 6.5 dB	± 3.1 dB

service. The demands made on a detector diode in many ways run counter to the requirements for a good mixer diode. Especially if it is to work without DC bias, a detector diode must have a very large dynamic resistance at small RF signal levels to produce a high output voltage for a given detected current. Detector diodes typically drive low-frequency amplifiers with input impedances exceeding 100 kilohms so low series resistance is not an important quality. On the other hand, mixer circuits require the series resistance to be as low as possible for best conversion loss.

A curve tracer test showed that the DC series resistance of the Aertech diodes was about 350 ohms. If we assume typical values of RF source and IF load impedances of 200 ohms, Equations (5-7) and (5-8) tell us the added loss due to this series resistance is about 9 dB. This is a minimum figure since skin effects and other factors tend to make the microwave series resistance higher than the value measured at low frequencies.

After the initial experiment was completed, some NEC type ND4141 diodes were obtained. They were designed expressly for mixer service, and their measured series resistance was 12 ohms. The same setup was arranged as in Fig. 6-2, except that the test area was an enclosed laboratory room about 5 m X 7 m, instead of the long, empty hall used originally. In the initial test, the hall acted as an anechoic chamber for the small volume occupied by the mixer. In the test about to be described, all that was required was a ratio between the mixer conversion losses using Aertech and NEC diodes so the exact nature of the local

field was not important as long as it remained the same during the test.

An IF output was obtained from the mixer using Aertech diodes, and its relative level noted. Then, disturbing nothing else, we replaced the Aertech diodes with NEC units, remounted the mixer, and measured the IF output again. It had increased by 10.9 ± 1 dB. Subtracting this figure from the first measured conversion loss of 17.4 dB gives a figure for the NEC diodes of 6.5 ± 3.1 dB, which was the best conversion loss obtained. This loss is quite comparable to those encountered in conventional mixers, and shows the practical feasibility of this type of mixer.

CHAPTER 7: SLOT-RING MIXER AND POLARIZING FILTERS

Heretofore, the slot-ring mixer has been studied in isolation as it interacts with plane waves. By adding quasi-optical elements such as polarizing filters, we can enhance the performance of the mixer by increasing the forward gain of the antenna in the RF direction, and by reducing the LO power leakage into the RF region. Experiments verifying these effects will now be detailed beginning with the design of the polarizing filters.

POLARIZATION FILTER DESIGN

The history of polarizing filters in electromagnetics goes back to Hertz, who used grids of unidirectional parallel wires to demonstrate the similarity between polarized radio waves and polarized light. Although rather tedious to build now that photolithographic etching is possible, a wire grid is still an effective means of reflecting linearly polarized waves whose electric vector is parallel to the wires. If the wires are thin enough compared to the spaces between them, waves polarized perpendicular to the wires pass through the grid with virtually no attenuation.

The wire grid received considerable theoretical study before 1900, and Lamb [1] was one of the first to originate an expression for

the power reflection coefficient of such a grid. He assumed that the distance d between adjacent wires was much smaller than a wavelength which is a reasonable assumption if diffraction effects are to be avoided. He then applied conformal mapping techniques to the resulting electrostatic problem and derived this expression for the power reflection coefficient r_p for parallel-polarized waves:

$$r_p = \frac{1}{1 + [(2d/\lambda) \cdot \ln(d/2\pi a)]^2} \quad (7-1)$$

where a is the radius of the wires in the grid. A good polarizer will have an r_p approaching unity. If there are no losses in the wires and no scattering in other directions, conservation of power tells us that the power transmission coefficient t_p is:

$$t_p = 1 - r_p \quad (7-2)$$

If the wire spacing is too large with respect to either the wavelength or the wire radius, the squared term in Equation (7-1) exceeds unity and the filter becomes ineffective. The logarithmic term allows fairly small wire to be used without compromising performance.

Basing the design on these factors, we constructed a pair of polarizing filters. Fig. 7-1 shows how a framework was made from two

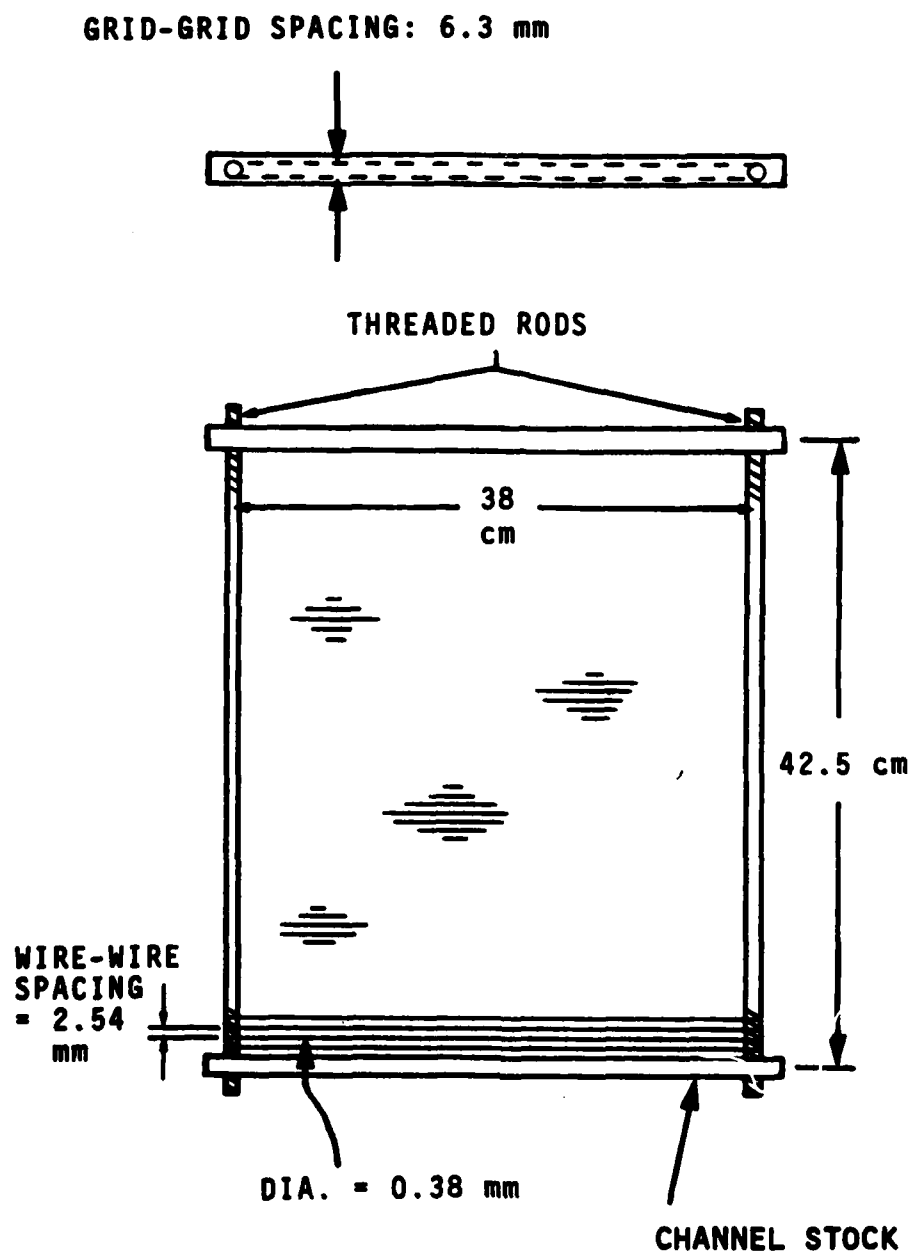


Fig. 7-1. Polarizing filter for use at X-band.

threaded rods and two sections of extruded aluminum channel stock. A wire was fixed to the end of one rod and wound around the outer side of both rods in an elongated spiral pattern. Alternate threads were skipped to produce a wire-to-wire spacing of 2.54 mm. This method of winding the wire on each frame produced two grids separated by the rod diameter of 6.35 mm.

Using Equations (7-1), (7-2), and the dimensions given in Fig. 7-1, we find that a single grid should attenuate a parallel-polarized plane wave by about 20 dB at 10 GHz. To measure the attenuation experimentally, one of the double-grid frameworks was interposed between two co-polarized horns facing each other. The horn gain and spacing to the polarizing screen was such that the screen intercepted most of the main-lobe power. The increase in the space loss between the horns when the screen was inserted was about 30 dB which is somewhat less than double the single-screen calculated attenuation of 20 dB. Since the two screens are less than a quarter-wave apart, coupling between the two screens probably reduced the attenuation below 40 dB. A 30-dB attenuation of the undesired polarization along with an unmeasureably small attenuation to waves polarized perpendicular to the wires was judged to be satisfactory performance for the quasi-optical experiments to follow.

FRONT POLARIZATION FILTER

Several advantageous effects can be achieved by placing a polarizing filter in front of the mixer's dielectric side between it and the

AD-A135 252

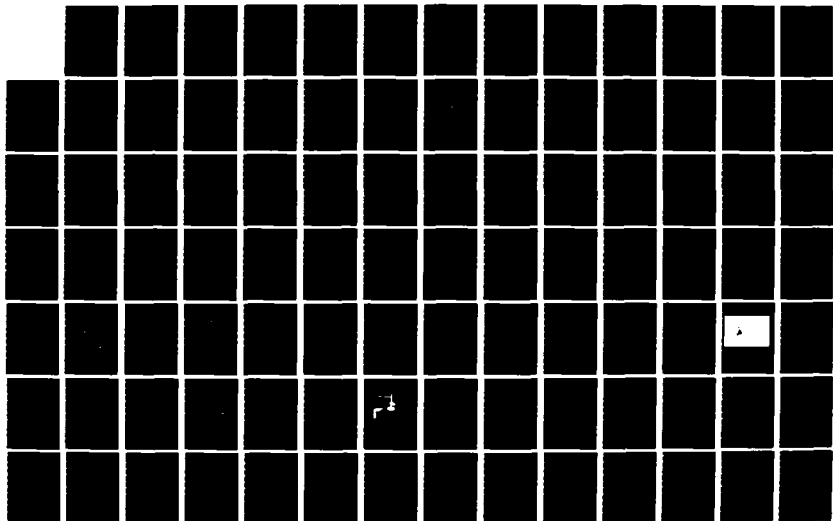
A STUDY OF MICROWAVE AND MILLIMETER-WAVE QUASI-OPTICAL
PLANAR MIXERS(U) TEXAS UNIV AT AUSTIN MICROWAVE LAB
K D STEPHAN ET AL. 31 AUG 83 MW-83-2 ARO-17735.25-EL
DAG29-81-K-0053

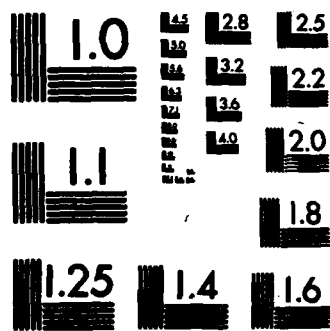
2/3

UNCLASSIFIED

F/G 9/5

NL





MICROCOPY RESOLUTION TEST CHART
NATIONAL BUREAU OF STANDARDS-1963-A

source of RF energy. The most significant effect is an increase in the LO-RF isolation of the mixer system.

In a conventional mixer an important practical figure of merit is the LO-RF isolation which is expressed as the ratio of LO power emerging from the RF port, to the LO power available at the LO port. Poor isolation allows substantial LO power to travel back along the RF path where its presence may not be desired. This is especially true with electronic intelligence receivers where emission of signals can alert the enemy that he is being spied upon. A less dramatic but more common reason to achieve high LO-RF isolation is to prevent radiation of LO power to other receivers in a large system where it can cause interference with desired signals.

The LO-RF isolation figure of a quasi-optical mixer is difficult to define for the now familiar reason that no single-mode ports are available at which the ratio of two unique voltages can be determined. In the absence of a better definition, then, let us describe an experiment that gives a ratio I_q analogous to the LO-RF isolation of a conventional mixer. At a distance R from the mixer, suppose we measure the power density of LO radiation leaking around it from the LO source. Call this intensity I_1 . If we now remove the mixer structure but leave the LO source in position, the LO power density at R will rise to a reference level I_2 . We then define I_q to be

$$I_q = I_2/I_1 \quad (7-3)$$

In this way, the distance between the mixer and the measuring point is made to cancel, and I_q is essentially the degree to which the mixer structure shields the LO feed radiation from the RF region.

The polarization duplexing of the slot-ring mixer presents a further complication. Assume that, as in Fig. 7-2, the RF wave is horizontally polarized and the LO wave is vertically polarized. Even without any polarization filters, the symmetry of the system insures that there will be no horizontally-polarized LO energy present in the RF region. Hypothetically, then, the LO-RF isolation is infinity if vertically-polarized LO energy is sought in the RF region with a horizontally-polarized probe. However, there will be considerable vertically-polarized energy which was not intercepted by the mixer, and this energy can cause trouble just as easily as horizontally-polarized radiation can. In a practical sense, the LO-RF isolation of the bare mixer is poor when polarization is disregarded. It is this figure which the front polarizing filter improves.

When a vertical grid is placed in front of the mixer structure as in Fig. 7-2, its reflection coefficient of nearly unity returns most of the LO power that was not absorbed by the mixer. This experiment was tried with the double-grid polarization filter described above, and the LO-RF isolation as defined in Equation (7-3) was measured with the RF horn both co-polarized and cross-polarized with respect to the LO polarization. The isolation in the co-polarized configuration was 27 dB, and

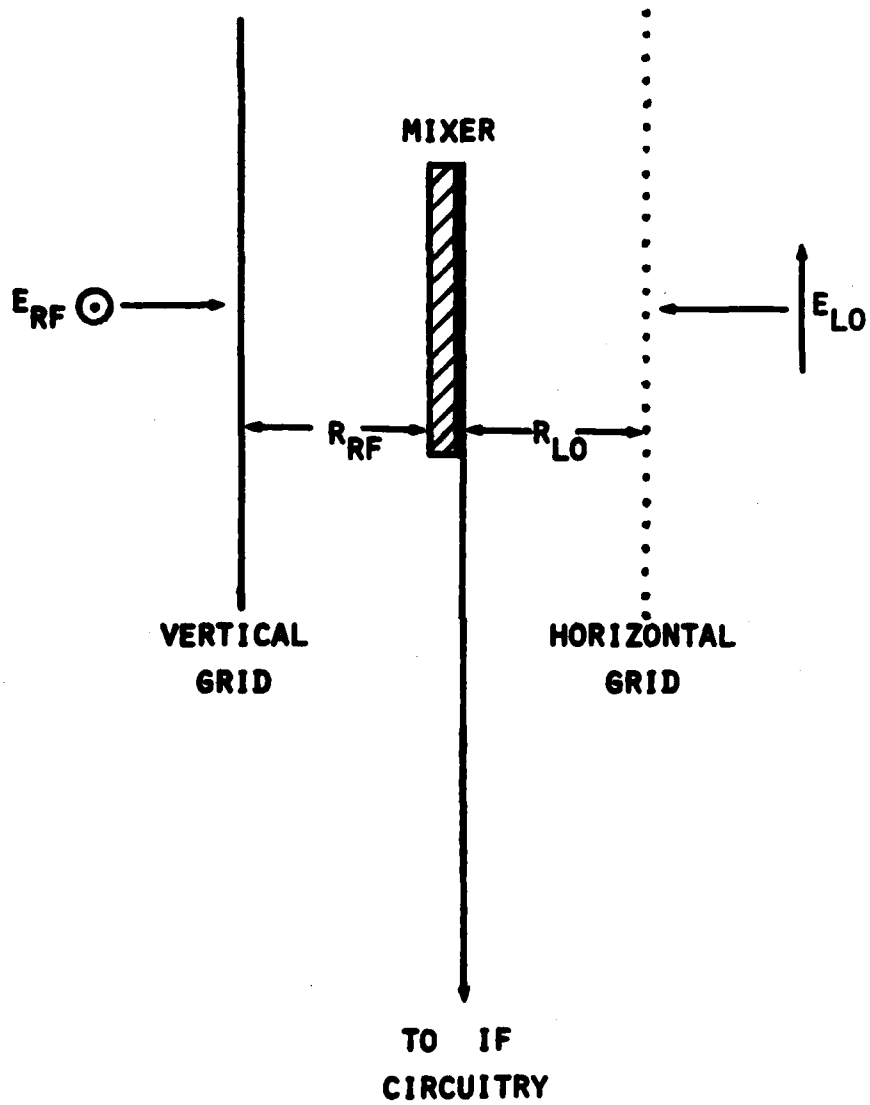


Fig. 7-2. Use of polarizing filters with slot-ring mixer.

cross-polarized isolation was 30 dB. For the moderate size of screen used, these figures were quite good and compare favorably with isolation attained in commercial practice.

An antenna-related figure of merit which interests microwave systems engineers is cross-polarization rejection. Communications systems, especially those involving satellites, presently use a form of polarization duplexing in which half the channels in a given band are polarized orthogonally with respect to the other half. This allows frequency re-use within the band, almost doubling its capacity. Of course, the antennas used for reception of these signals must be able to discriminate between the two polarizations. The ratio of the antenna's response to the desired polarization compared to the undesired response is called the cross-polarization rejection R_{cp} . Typical values of R_{cp} for earth-station receiving antennas are 25-35 dB.

The front polarization filter can improve the slot-ring mixer's already good cross-polarization rejection in the following way. If the mixer structure is perfectly balanced (symmetrical mechanical structure and identical diodes), the cross-polarization rejection is infinity even without a front filter. In reality, perfect balance can never be achieved, and in the absence of a front filter, the mixer under discussion had a cross-polarization rejection of 15 dB. Inserting the vertical grid in front of the mixer had the effect of reducing the cross-polarized RF signal incident on the mixer, and improved the cross-polarization rejection somewhat, to 20 dB. The full 30 dB of rejection that the isolated screen can give was not realized in this

experiment. It is possible that near-field effects are occurring since the screen-mixer distance R_{RF} in Fig.7-2 was only 5 cm. Nevertheless, the front screen did improve the cross-polarization rejection by 5 dB, a significant amount.

A third advantage of the front polarization filter is that it can reduce the amount of LO power required. No experimental confirmation of this was made, but it is clear that, as the distance R_{RF} is made smaller, the LO wave reflected back to the mixer will combine with the incoming wave. At intervals of about one-half wavelength, the incident and reflected waves will add in phase, producing a higher available LO voltage for the mixer diodes. Depending on the relative magnitudes of the incident and reflected waves, this improvement can be 3 dB or more.

Conversion loss is a very sensitive function of LO power below a certain minimum. A typical curve relating conversion loss to LO power in an experimental mixer is given in Fig. 7-3. Minimum loss occurs at an LO power of about +7 dBm with a gradual falloff above this level due to diode breakdown effects. Below the optimum power level loss increases gradually at first, and then very swiftly as the diodes cease to act as switches and their off-on resistance ratio falls precipitously. In the case of single-ended mixers, reasonable conversion loss can be maintained at low LO power levels (<0 dBm) by proper DC biasing, but such "starved" mixers suffer from increased noise figure and reduced dynamic range. Without greatly complicating the circuit, it is impossible to provide DC bias for single- or double-balanced mixers.

Required LO power is primarily a function of the number and kind

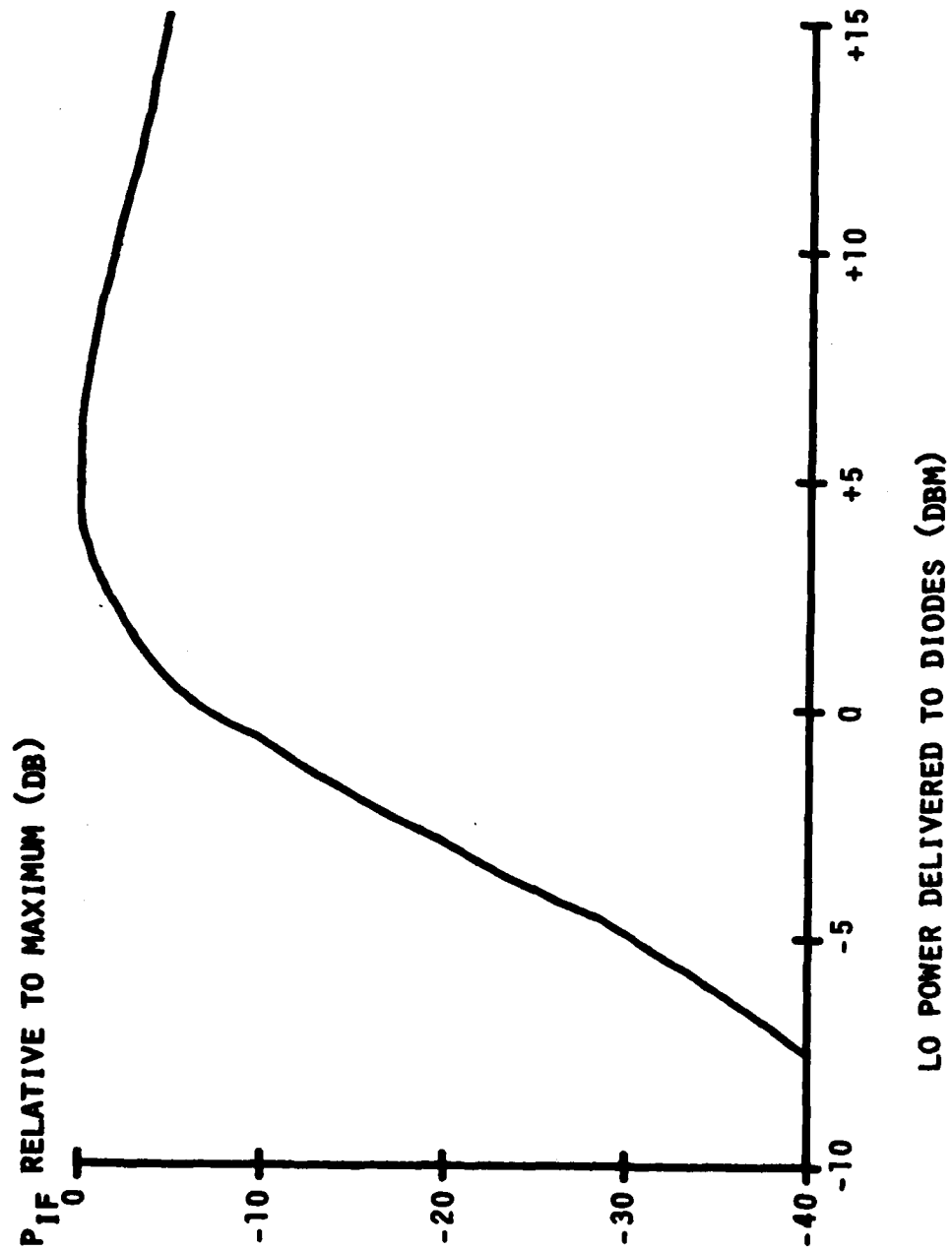


Fig. 7-3. Typical dependence of conversion loss on LO power delivered to diodes.

of diodes used and does not depend on the mixer circuit itself as long as losses are not considered. In common with other single-balanced mixers, the slot-ring mixer needs about +4 to +7 dBm delivered to its diodes for optimum conversion loss. To provide this much power to the diodes requires a much greater power to be radiated from the LO horn since the free-space method of coupling LO power is very inefficient. This feed method was chosen with array configurations in mind, since it is the simplest possible way to feed many mixers at once. Typical values of power delivered to the LO horn in these experiments to obtain optimum conversion loss were +20 to +25 dBm. Most of the power went into the space surrounding the mixer even though the horn-mixer distance was only 25 cm. Every dB of gain in the LO direction caused by the front polarization filter means a 1 dB reduction in the required LO power. At X-band, powers approaching the one-watt level (+30 dBm) are relatively easy to generate, but such a requirement at millimeter-wave frequencies is usually prohibitive. Conservation of LO power by the front filter can thus make a vital difference in arriving at a practical design.

REAR POLARIZATION FILTER

In the same manner that the front polarization filter increases antenna gain in the LO direction, a horizontal filter placed behind the mixer as shown in Fig. 7-2 can increase the forward gain in the RF direction. The orthogonality of the RF and LO waves allows independent adjustment of the two gains. This procedure was also tried exper-

imentally and yielded a 6 to 8 dB increase in IF output power compared to the mixer performance without the filter. Strictly speaking, this increase is not a reduction in conversion loss of the mixer circuit as defined in Equation (5-1). Rather, the rear filter changes the radiation pattern so as to increase forward gain in the RF direction at the expense of the lobe on the opposite side which serves no useful purpose.

CHAPTER 8: PROPOSED USES AND CONCLUSIONS

The rudimentary polarization filter experiments just described are only a sample of the wide variety of quasi-optical techniques applicable to the slot-ring mixer. A few of the more obvious and useful ones will be briefly outlined here to guide further investigations and applications in this area. We conclude Part I with a summary of the findings concerning the slot-ring mixer.

FURTHER PATHS

The goal of this research program was to devise a mixer simple enough to form an element in a large planar array of identical mixers. One inescapable problem in any such array arises when we try to connect to the multiple IF output lines without causing severe crosstalk between channels, or interference with the RF performance of the array. Three-dimensional connections to the rear of the array, for example, would be straightforward but mechanically awkward. One solution which retains the planar format is shown in Fig. 8-1. Each IF output is in the form of coplanar line which leads to the edge of the array. If the split in the ground plane is found to disrupt the RF currents excessively, another thin dielectric layer could be deposited and another metallization formed as shown in Fig. 8-2. The thin dielectric layer would act as

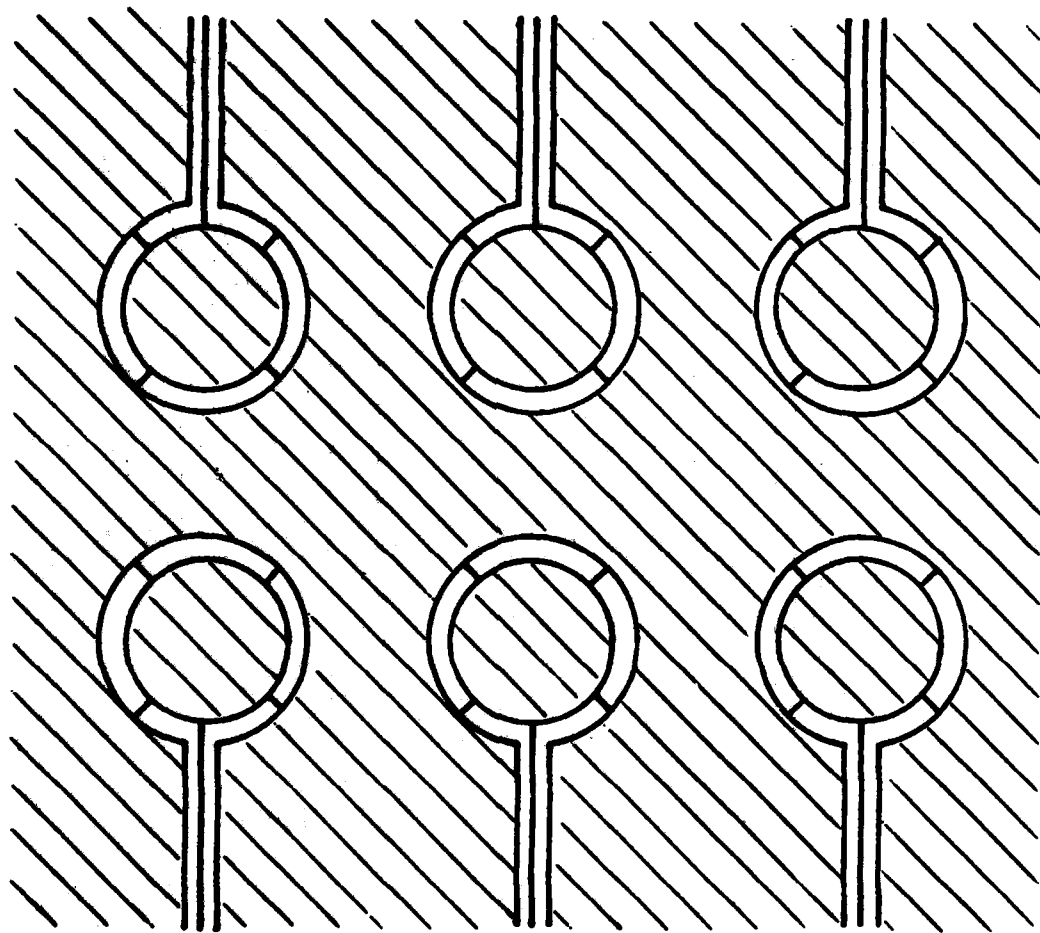
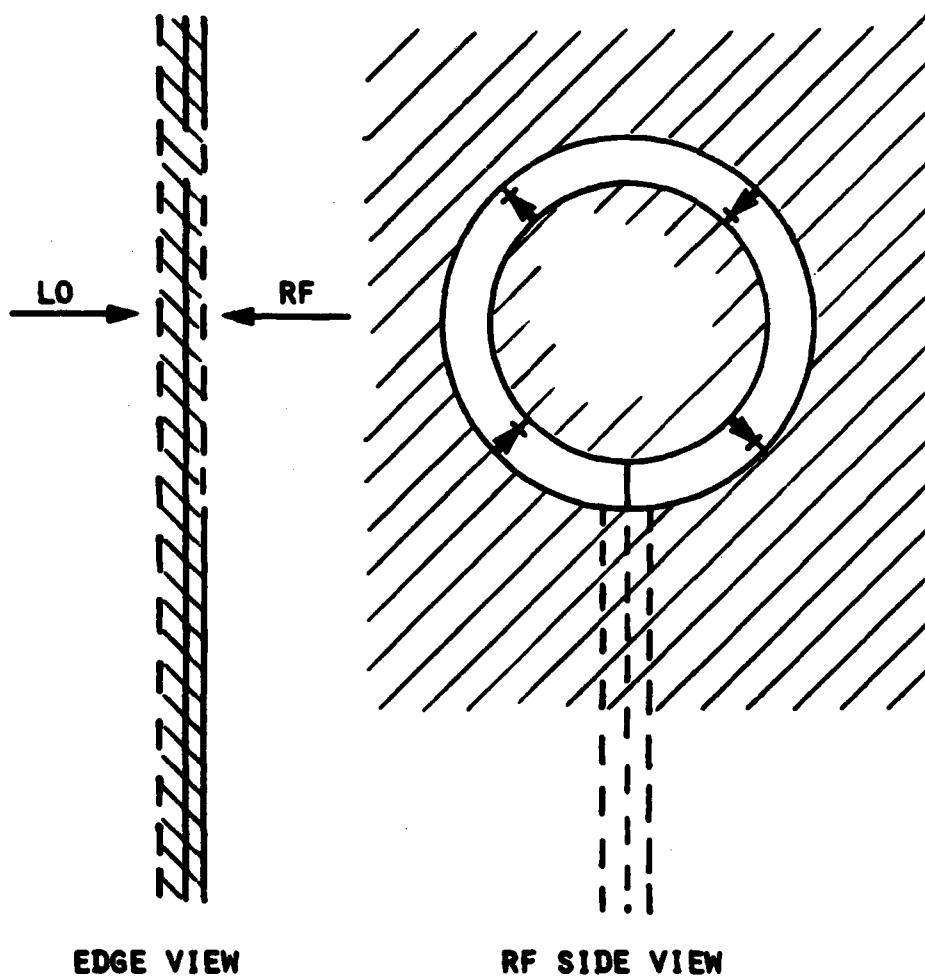


Fig. 8-1. Proposed array of slot-ring mixers.



**Fig. 8-2. Shielded coplanar-line IF outputs
for mixer array.**

a short circuit to the millimeter-wave RF signal, and the second metallization would present uniform circular rings to the RF currents without any interruption on the RF side.

In any array configuration, mutual impedances between antennas must be considered since they can cause the array pattern to depart drastically from a simple superposition of individual isolated antenna patterns. This is a fertile area for further study.

Images can be formed with either reflective or refractive devices. A parabolic or spherical dish is an example of the reflection technique while a dielectric lens forms an image by refraction. Fig. 8-3 illustrates one way that the LO power could be provided to a slot-ring array at the focus of a dish. A solid reflector plate behind the array maximizes the gain of both polarizations in the direction of the dish. The relatively broad pattern of the slot-ring antenna makes it especially suitable for illumination of dishes with a low f/D ratio where other devices might encounter problems.

An example of a dielectric-lens imaging system is given in Fig. 8-4. At millimeter wavelengths, an electrically large lens is not difficult to make and provides very high gain. The wide radiation pattern of the array would lead to good illumination of such a lens.

Applications of phased-array technologies have thus far mostly been limited to X-band and below where reliable and low-loss phase shifters are possible. By converting the incoming RF wave down to a frequency where phase shifting is again an easy matter, quasi-optical mixers could open the door to millimeter-wave phased arrays.

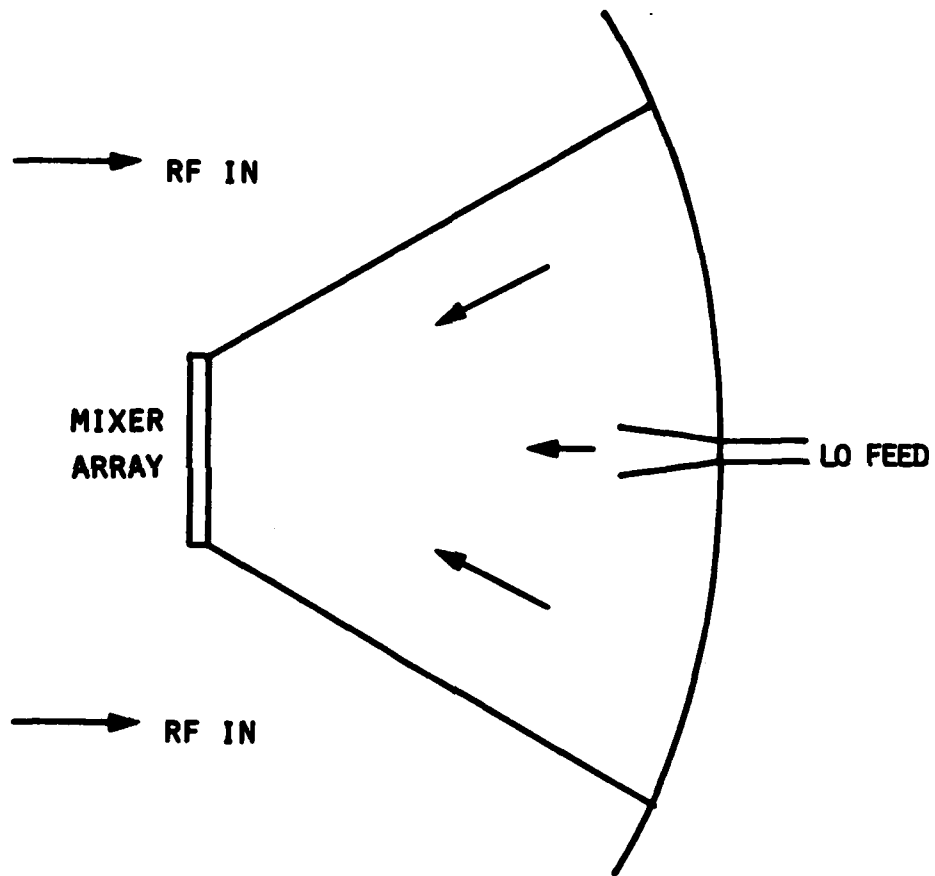


Fig. 8-3. Dish used for imaging.

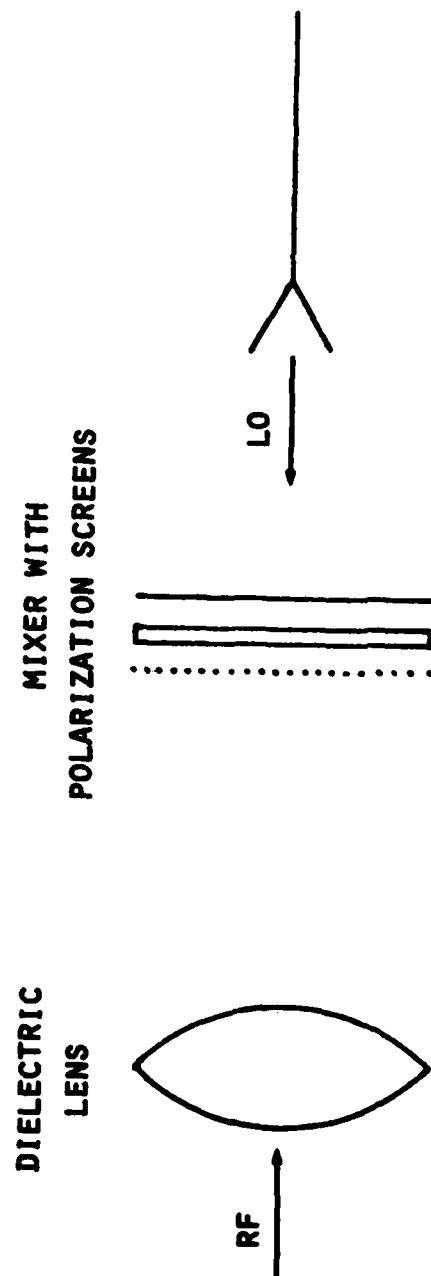


Fig. 8-4. Dielectric lens used for imaging.

CONCLUSIONS

Part I has traced the theoretical development of the slot-ring antenna operated in its first-order resonant mode. Explicit and easily evaluated expressions for the radiation patterns and terminal resistance of the antenna were derived, and it was shown that by using the two orthogonal modes of the antenna, a simple and effective balanced mixer was possible. The theories were confirmed by extensive experiments investigating the radiation impedance, antenna patterns, and the operation of a model X-band mixer. The mixer tested gave a best conversion loss of $6.5 \text{ dB} \pm 3 \text{ dB}$, and straightforward frequency scaling indicates that millimeter-wave mixers should have similar performance, if diodes of sufficient quality can be made. Some techniques for using arrays of such mixers for imaging and phased-array purposes were proposed, and further areas of study were outlined.

PART II : THE BOWTIE ANTENNA SUBHARMONIC MIXER

CHAPTER 9: INTRODUCTION

In Part I, we saw how a very simple planar metal pattern on a dielectric sheet can be used as a quasi-optical mixer. We also noted a significant limitation: the free-space LO coupling method requires large amounts of LO power for optimum conversion loss. This demand for high local oscillator levels is relatively easy to satisfy below about 30 GHz but becomes increasingly burdensome in the millimeter-wave range.

The cost of generating a given level of microwave energy generally goes as the frequency raised to a power between 1.5 and 2.5. That is, a source designed to deliver 10 mW at 20 GHz will cost about four times as much as a 10-mW source at 10 GHz. Carrying this rule into the millimeter-wave range leads to high prices very rapidly. Asking for a given power at higher and higher frequencies eventually carries one past the present state of the art, beyond which no single device is available at any price. One can then resort to power-combining techniques, but this alternative is inconsistent with the appealing simplicity of the quasi-optical mixer. A much better choice, and one which inspired the work to be described later, is to develop a mixer circuit using roughly the same LO power as before but at a much lower frequency. If the new f_{LO} is a subharmonic ($1/2$, $1/3$, $1/4$, . . .) of the original f_{LO} , such a mixer is said to be subharmonically pumped. Suitable circuits can make such a subharmonic mixer nearly as efficient as a conventional mixer.

In this part, we will trace the theoretical and experimental

development of a broadband antenna suitable for use in a quasi-optical subharmonic mixer. The special mixer circuit used to achieve efficient subharmonic mixing will then be described. Finally, a series of experiments similar to those of Part I will show that the conversion loss of this mixer was as low as 8.6 ± 3 dB at 14 GHz, depending on the diodes used. The same device performed well in the millimeter-wave frequency range. The antenna used for this subharmonic mixer is a variant of one that is familiar to many UHF television viewers: the bowtie. This simple structure is especially suitable for quasi-optical subharmonic mixer service, as the following chapters will show.

CHAPTER 10: THE INFINITE FIN ANTENNA

The metallic bowtie antenna in Fig. 10-1 is not new. Its antecedents can be traced to early attempts to broaden the inherently narrow bandwidth of a thin wire dipole. Thicker conductors were found to lower the radiation Q considerably, allowing a wider range of frequencies to be used for a given maximum standing-wave ratio on the antenna's transmission line.

Extending the distance r_0 in Fig. 10-1 to infinity creates what we call the infinite fin antenna. It is one of a class of structures which are characterized entirely by angles. A drawing of the structure to any scale can be superimposed on the original and it will fit. No linear dimensions are needed to describe it. Such antennas have very interesting properties as broadband radiators, and in 1957 V. H. Rumsey showed [1] that the performance of such an antenna was in fact independent of frequency. The main drawback to such hypothetical devices is that some part must extend to infinity, since cutting the structure at some finite point gives it a characteristic length and destroys the frequency-independent property.

Fortunately, several antennas of this type were found in which the surface currents decayed quite rapidly, faster than $1/r$, as one went farther from the feed point. For these antennas, truncating them at a large radius where the currents had died away had only a small effect on the frequency-independent property. Many successful designs grew from

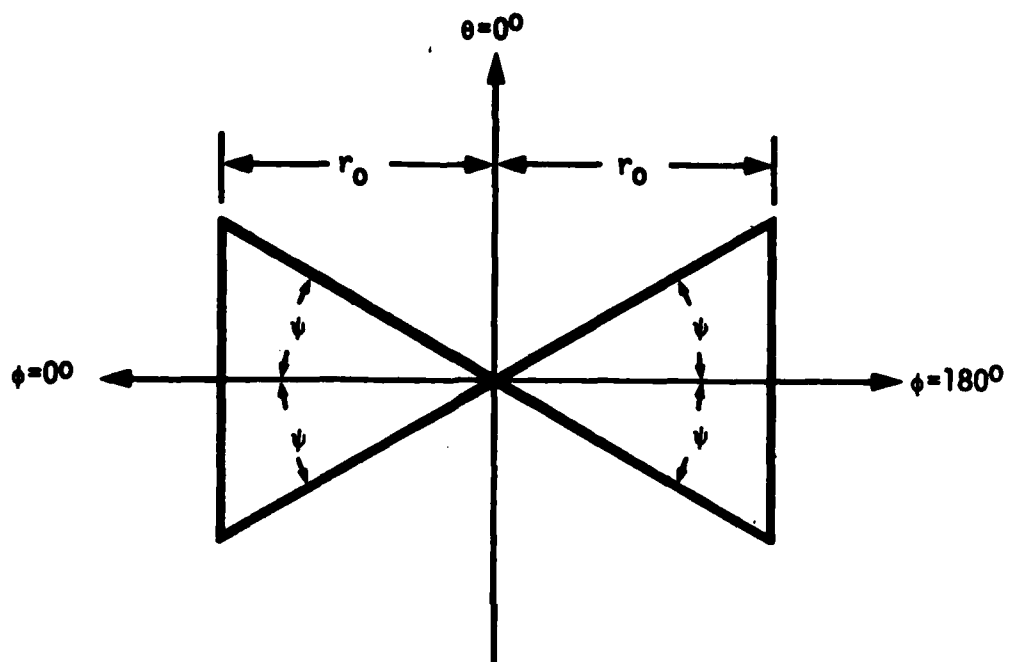


Fig. 10-1. The metal-only bowtie antenna.

this work, including the equiangular spiral antenna and the log-periodic antenna. As part of his investigation of infinite structures, R. L. Carrel studied the properties of the infinite fin antenna and found a mathematically exact expression for its impedance [2]. In his paper, he assumed vanishingly thin lossless conductors, but such a qualification is quite acceptable in most antenna work of this kind.

When r_0 goes to infinity, the resulting structure is characterized by ϕ , the half-angle of the fin. Carrel generalized his work to include asymmetrical antennas with different fin angles on each side, but we will restrict our discussion to structures having mirror symmetry about the plane perpendicular to the fin axis.

A complete recapitulation of Carrel's derivation will not be given here. Briefly described, his analysis took the form of a three-stage conformal mapping of the infinite fins into a finite two-dimensional parallel-plate structure. The characteristic impedance of the latter was trivially easy to calculate, and thus the problem was solved exactly.

Carrel's analysis showed that the infinite fin antenna was actually a constant-impedance TEM transmission line having a characteristic impedance Z_0 given by

$$Z_0 = \frac{\eta K(\cos\phi)}{4 K(\sin\phi)}$$

(10-1)

where the function $K(x)$ is the elliptic integral defined by

$$K(x) = \int_0^1 [(1-t^2)(1-x^2t^2)]^{-1/2} dt \quad (10-2)$$

This function is tabulated extensively and was used to derive the plot of the infinite fin antenna's impedance shown in Fig. 10-2. It should be mentioned that because of the fin antenna's mirror symmetry, the impedance of the structure is halved when half of the antenna is mounted and driven against a ground plane, as in Fig. 10-3. This is exactly true for both the infinite-fin and the truncated bowtie structures provided that the ground plane exactly coincides with the antenna's plane of mirror symmetry. Although both Carrel's study and some impedance measurements studied later dealt with the unipole against ground, all discussions to follow will concern only the balanced two-fin antenna, since this is the practical form in which the antenna is used.

By straightforward differentiation of the potential function that Carrel found, it is easy to derive the fields anywhere in the space surrounding the infinite fin antenna. Fig. 10-1 shows the spherical coordinate system we will use. One fin lies in the $\phi = 0^\circ$ half-plane, the other in the $\phi = 180^\circ$ half-plane. Both fins extend for an angle ψ above and below their respective axes. To develop the exact expressions for the fields surrounding the antenna, we must evaluate certain constants arising from the mapping operations.

Given the angular dimensions just defined, these auxiliary con-

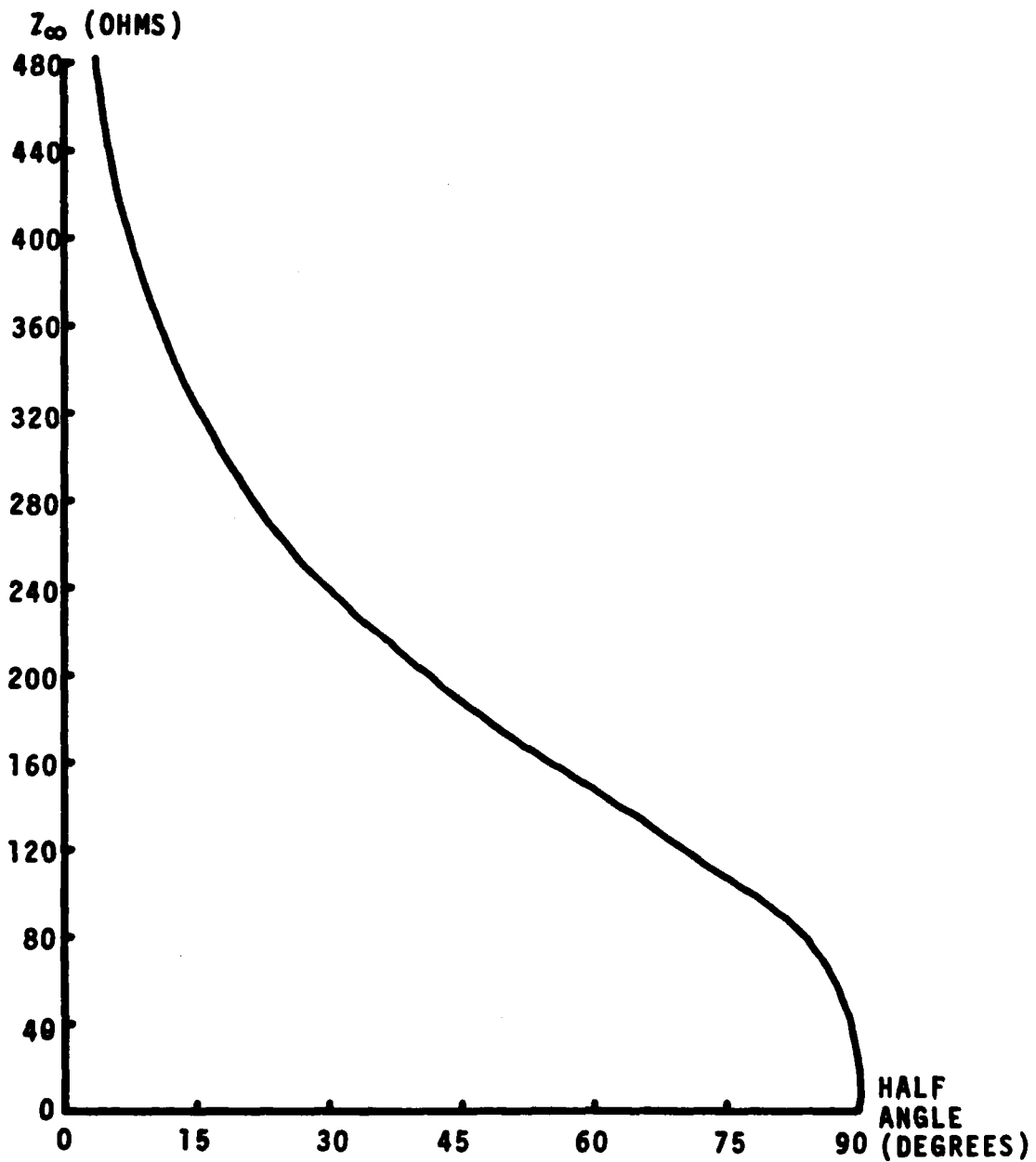


Fig. 10-2. Infinite fin antenna Z_{∞}

versus half-angle ψ .

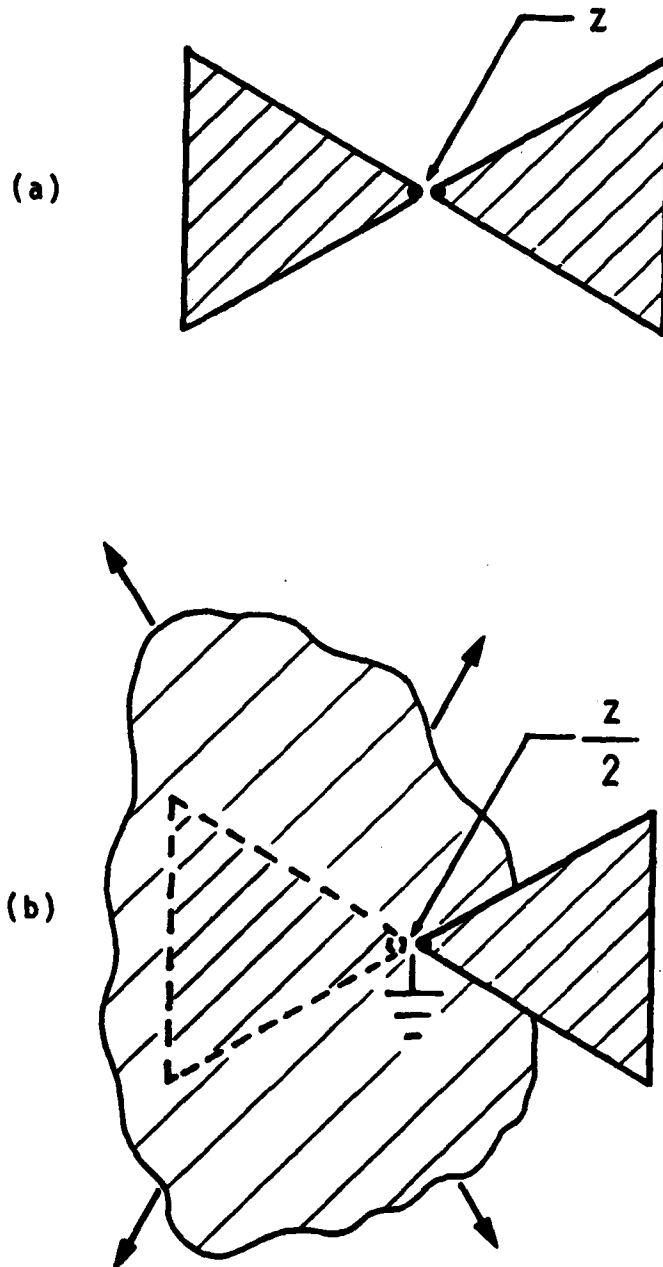


Fig. 10-3. (a) Symmetrical dipole (b) Unipole and ground.

stants may be determined:

$$D = \cot[1/2(\pi/2 - \phi)] \quad (10-3)$$

$$k = \frac{1 - \sin\phi}{1 + \sin\phi} \quad (10-4)$$

$$K_k = K(k) \quad (10-5)$$

All the constants above are real and fixed for a given set of dimensions.

Now we define a complex auxiliary function

$$\sigma(\phi, \theta) = D \cdot \tan(\theta/2) \cdot e^{j\phi} \quad (10-6)$$

and we assume the voltage present at the input terminals is of the form $V_{LD} \cdot \exp(j\omega t)$. If the free-space propagation constant of the uniform medium surrounding the antenna is k_0 and the medium's impedance is η , then the electric and magnetic fields everywhere are given by:

$$E_{\theta}(r, \theta, \phi, t) =$$

$$- \frac{V_0 D e^{j(\omega t - k_0 r)}}{2K_k r (1 + \cos 2\theta)} \cdot \operatorname{Re} \left[\frac{e^{j\phi}}{\sqrt{(1 - \sigma^2)(1 - k^2 \sigma^2)}} \right]$$

(10-7)

$$E_{\phi}(r, \theta, \phi, t) =$$

$$- \frac{V_0 D \tan(\theta/2) e^{j(\omega t - k_0 r)}}{2K_k r \sin \theta} \cdot \operatorname{Re} \left[\frac{j e^{j\phi}}{\sqrt{(1 - \sigma^2)(1 - k^2 \sigma^2)}} \right]$$

(10-8)

$$H_{\theta}(r, \theta, \phi, t) = -E_{\phi}/\eta$$

(10-9)

$$H_{\phi}(r, \theta, \phi, t) = +E_{\theta}/\eta$$

(10-10)

$$E_r = H_r = 0$$

(10-11)

As in any TEM structure, the transverse electric fields are simply related to the magnetic fields by the impedance of the surrounding medium η .

So far, the fields found are of little practical interest, since the structure creating them is impossibly large to build. The equations

tell us that the antenna currents decrease with radial distance only as $1/r$, so truncation can be expected to have a significant effect. Nevertheless, these fields constitute the only outward-traveling mode excited in a bowtie antenna of finite length. As we shall now show, they form an integral part of the analysis of such a practical structure.

CHAPTER 11: BOWTIE ANTENNA THEORY

In this chapter, the modal expressions in spherical coordinates for outward-traveling waves are briefly described. An analysis technique for finding the radiation patterns and terminal impedance of the bowtie antenna is outlined, and an equivalent circuit for the antenna is derived. Despite its simplicity, this model is shown to give surprisingly good results.

MODES OF FREE SPACE

Harrington [1] shows how any AC field in a homogeneous source-free region may be expressed as a combination of two sets of modes. All the magnetic fields in one set are transverse to the radial unit vector (TM to r), and the other set is composed of modes in which the electric fields are transverse to r (TE to r). These modes are generated in the following way.

Let $P_{nm}(\cos\theta)$ represent the associated Legendre function of the first kind. Let $h_n^{(i)}(kr)$ be the spherical Hankel function defined in terms of the Hankel function of the i th kind $H_n^{(i)}(kr)$:

$$h_n^{(1)}(kr) = [\pi kr/2]^{1/2} \cdot H_n^{(1)}(kr) \quad (11-1)$$

With these functions in mind, we can now define a scalar potential function A_{mn} :

$$A_{mn} = P_{mn}(\cos\theta) \begin{Bmatrix} \cos(m\phi) \\ \sin(m\phi) \end{Bmatrix} \cdot \begin{Bmatrix} h_n^{(1)}(kr) \\ h_n^{(2)}(kr) \end{Bmatrix} \quad (11-2)$$

where $n = 1, 2, 3, \dots$ and $m = 0, 1, 2, 3, \dots$. Either the cosine or the sine function can be chosen for the longitudinal dependence. The spherical Hankel functions of the first and second kind generate inward- and outward-traveling waves, respectively. If these scalar potentials are multiplied by the radial unit vector u_r , they satisfy the vector Helmholtz equation. The functions thus generated in spherical coordinates are solutions to Maxwell's equations in spherical coordinates. The TM fields are developed by the vector equations:

$$H_{mn}^{TM} = \nabla \times u_r(A_{mn}) \quad (11-3)$$

$$E_{mn}^{TM} = (1/j\omega\epsilon) \nabla \times H_{mn}^{TM} \quad (11-4)$$

where ϵ = dielectric constant of the surrounding medium. Similarly, the TE fields are found by using the following set of equations, which are the duals of Equations (11-3) and (11-4) above:

$$E_{mn}^{TE} = -\nabla \times u_r(A_{mn}) \quad (11-5)$$

$$H_{mn}^{TE} = -(1/j\omega\mu) \nabla \times E_{mn}^{TE} \quad (11-6)$$

where μ = permeability of the medium. In principle, this set of modes can be used to represent the radiation field from any structure, providing the relative excitation of the various modes can be determined. Practically, this problem is very difficult, and the elaborate computer-aided techniques necessary to solve it give no guarantee of success in a finite time. Fortunately, the bowtie antenna appears to excite only a few of these modes in the frequency range of interest.

MODES THE BOWTIE ANTENNA EXCITES

A time-domain thought experiment will make clear the basic method used to analyze the bowtie antenna. Referring to Fig. 11-1, suppose that a bowtie antenna is suddenly excited at its terminals by a sinusoidal voltage. The only propagating mode to be excited will be the TEM

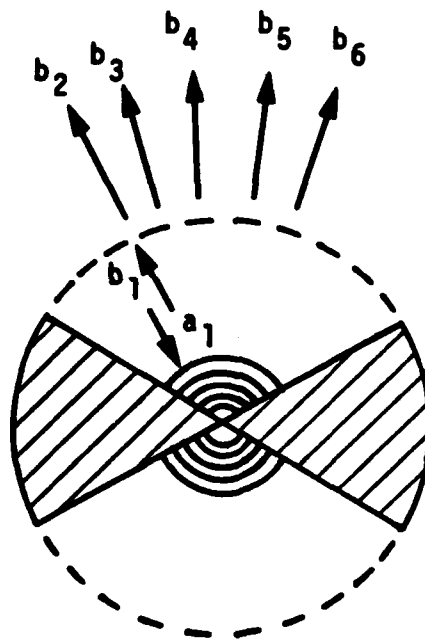


Fig. 11-1. Bowtie antenna exciting modes of free space.

mode developed in Chapter 10. This TEM wave will travel uniformly outward at the speed of light in the surrounding medium. Until the wave reaches the edges of the fins at r_0 , the fields are the same as those in an infinite-fin antenna. But the similarity ends when the the outgoing wave meets the edges. There the discontinuity caused by the ends of the conductors will excite many of the higher-order TE and TM modes. Their relative levels will be proportioned so as to satisfy the boundary conditions at the edges of the fins, as well as everywhere on the sphere $r = r_0$. These modes are represented by the $b_3, b_4, b_5 \dots$ coefficients shown radiating away from the sphere. The sum of these outgoing modes may generally not be the same as the fields of the TEM mode, although in some directions the change will be small. In addition to the radiating modes, reactive energy will be stored in evanescent modes near the fin edges. Finally, propagating modes will be reflected toward the origin, but only one of these is of the proper form to propagate all the way back to the source. This mode is the TEM mode already described. The presence of this reflected wave means that the reflection coefficient Γ measured at the terminals will be nonzero:

$$\Gamma = b_1/a_1 \tag{11-7}$$

This reflection will cause the input impedance to deviate from the infinite-fin antenna's impedance Z_∞ , although for small reflections this change will also be small.

In Fig. 11-2, we have attempted to model the bowtie antenna with an equivalent circuit, which is exact only for the portion of the circuit representing the fins. This portion is the leftmost section of transmission line, having impedance Z_{∞} and length r_0 . The coupling of the outgoing TEM mode to a given TE or TM mode outside the sphere is represented by an ideal transformer with turns ratio N . If a particular mode is not excited strongly, N is high, which means that its series impedance presented to the outgoing TEM wave is small. If for reasons of symmetry a mode is not excited at all, N goes to infinity and the series impedance at the primary vanishes. Determining the impedance representing a particular mode requires more detailed knowledge of its nature.

If we divide the magnitude of E_{θ} by the magnitude of H_{ϕ} for the wave of a particular mode, we can define a wave impedance Z_w for that mode:

$$E_{\theta}/H_{\phi} = Z_w \quad (11-8)$$

As we noted earlier, Z_w for the TEM mode of the infinite fin antenna is real and constant, equal to η everywhere. If the same operation is performed on the transverse field components of the TE and TM modes, the resulting Z_w is a function of r only [2]:

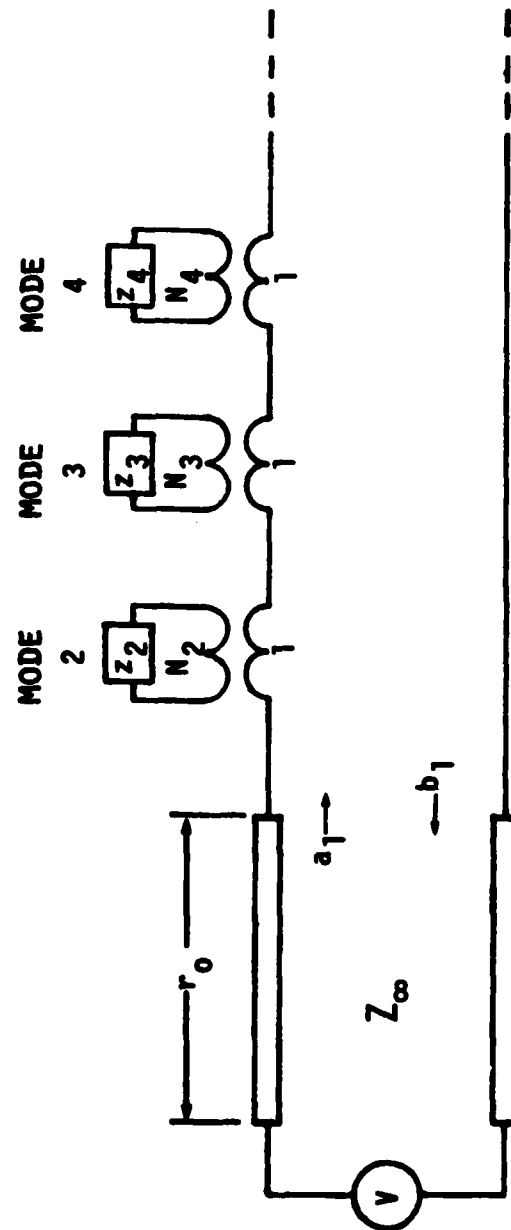


Fig. 11-2. General equivalent circuit of bowtie antenna.

$$Z_w^{TM} = j \eta \frac{h_n^{(2)'}(kr)}{h_n^{(2)}(kr)}$$

(11-8)

$$Z_w^{TE} = -j \eta \frac{h_n^{(2)}(kr)}{h_n^{(2)'}(kr)}$$

(11-9)

where the prime denotes the first derivative of the function with respect to the argument. By using the recurrence relations for spherical Bessel functions, L. J. Chu [3] found that these impedances could be synthesized by simple L-C ladder networks terminated in a resistor. The reactive components model the energy stored in the fields, and the resistor absorbs the power radiated to infinity. In principle, then, by replacing each impedance Z_n in Fig. 11-1 with the equivalent ladder network corresponding to its mode, the radiation impedance at the antenna terminals could be found for any frequency, once the transformer ratios were determined. Such a complex model is unnecessary, since in the frequency range of interest, the impedance is adequately modelled by using only one TM mode.

Simplifying things even more, we notice that the significant mode is the same as the field radiated by an elemental dipole. Specifically, it is the TM_{11} mode that results when $\cos(\phi)$ is used in the generating scalar potential:

$$A_{11} = P_{11}(\cos\theta) \cdot \cos\phi \cdot h_1^{(2)}(kr) \quad (11-10)$$

The transverse electric and magnetic fields of this mode are easily found to be:

$$H_{\theta} = (1/r) \cdot \sin\phi \cdot h_1^{(2)}(kr) \quad (11-11)$$

$$H_{\phi} = (1/r) \cdot \cos\theta \cdot \cos\phi \cdot h_1^{(2)}(kr) \quad (11-12)$$

$$E_{\theta} = +Z_{w11} \cdot H_{\phi} \quad (11-13)$$

$$E_{\phi} = -Z_{w11} \cdot H_{\theta} \quad (11-14)$$

where the wave impedance is given by

$$Z_{w11} = \eta \cdot \left\{ \frac{1}{jkr} + \frac{1}{\frac{1}{jkr} + 1} \right\} \quad (11-15)$$

The equivalent circuit yielding this wave impedance is shown in Fig. 11-3, for the case in which the impedance is evaluated at the fin-air interface sphere $r = r_0$. It is a simple high-pass filter whose impedance at low frequencies is dominated by the capacitance ($\epsilon \cdot r_0$). As the frequency goes to infinity, the reactive part will decrease in favor of the real part, which at $\omega = \infty$ will be equal to the free-space wave impedance η . This behavior agrees with the intuitively reasonable idea that, at a given radius r_0 , the low-frequency wave impedance is mainly reactive. As the cutoff frequency $k_0 r = 1$ is passed, radiation becomes easier as the wave impedance approaches its free-space value of η .

If we assume that the TM_{11} mode just described is the only radiating mode excited, the antenna's radiation patterns are then given simply by the mode expressions (11-11) through (11-14). For distances more than a few wavelengths away from the origin ($kr \gg 1$), the spherical Hankel function approaches a simple asymptotic form:

$$h_1^{(2)}(kr) \rightarrow -e^{-jkr} \quad (11-16)$$

allowing us to write the far-field radiation expressions as

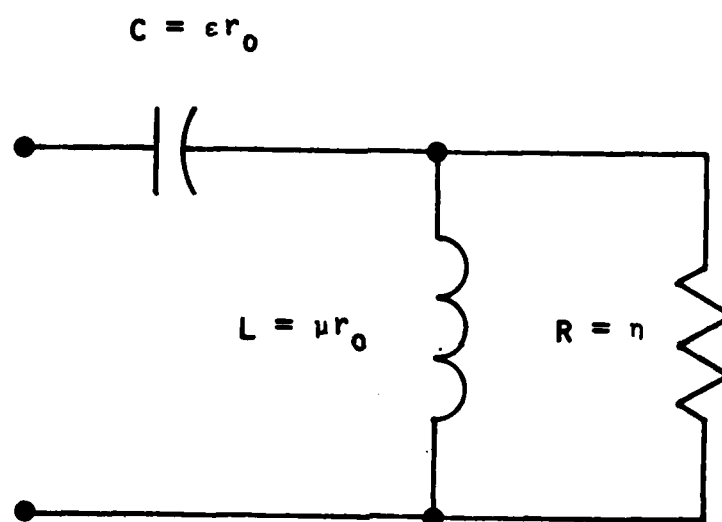


Fig. 11-3. Equivalent circuit of TM_{11} mode wave impedance.

$$H_{\theta} = -(1/r) e^{-jkr} \sin\theta \quad (11-17)$$

$$H_{\phi} = -(1/r) e^{-jkr} \cos\theta \cos\phi \quad (11-18)$$

and the E_{θ} and E_{ϕ} fields still derivable from Equations (11-13) and (11-14), respectively.

Even though other modes are not excited, the stored energy in the vicinity of the antenna will excite evanescent modes, and they will contribute capacitive reactance to the load seen by the TEM transmission line in Fig. 11-1. Lumping these reactances into a single capacitor C_f , we arrive at the simplified equivalent circuit of the bowtie antenna shown in Fig. 11-4. The only unknowns in the model are the value of the fringing capacitance C_f and the turns ratio N of the transformer.

CONFIRMATION OF SIMPLE THEORY

The theory developed so far is not distinguished by its mathematical rigor. A complete analysis would take the form of a boundary-value problem at the spherical surface $r = r_0$. The field outside the sphere would be expressed in terms of unknown coefficients of the various modes, and the problem would then consist of solving for the coefficients so that the continuity of electric and magnetic fields would be preserved in the presence of the known TEM mode coming from the

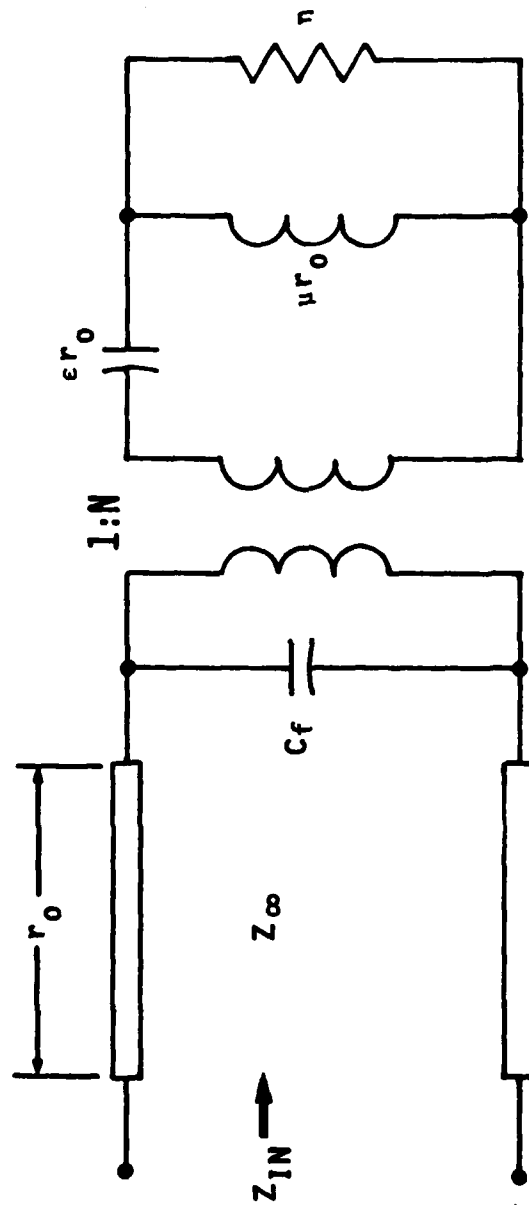


Fig. 11-4. Simplified equivalent circuit of bowtie antenna using only TM_{11} mode.

origin. Various methods such as mode matching are suitable for this type of problem, but the solutions require extensive computation and results are not guaranteed.

Such a procedure is unnecessary in this case, since it was found empirically that the simple one-mode model accounted for all the antenna features of engineering significance. In 1952, Brown and Woodward [4] of RCA undertook an exhaustive series of radiation-pattern and impedance measurements of the triangle antenna, which is the unipolar version of the bowtie. Their research was directed at developing a simple receiving antenna capable of use over the nearly 2:1 frequency range of the newly authorized UHF television band (470-890 MHz). By comparing the predictions of the one-mode model with their experimental results, we found that the model gave entirely satisfactory predictions over an octave bandwidth. This range corresponds to an edge-to-edge electrical length of from 190° to 360° , or roughly one-half wavelength to one wavelength. Using an electrical length of 240° as an example, we compare in Fig. 11-5 the E-plane and H-plane patterns measured by Brown and Woodward to the simple sinusoidal shapes predicted by the one-mode theory. Agreement is reasonably good.

An even better agreement can be found for impedance by empirically adjusting the remaining unknown parameters in the simplified equivalent circuit of Fig. 11-4. If we use $C_f = 0.211 \cdot \epsilon r_0$ and $N = 1.9$, the impedance Z_{in} is easily calculated with the lossless transmission line equation. An order-of-magnitude justification for this choice of N is that the ratio of the free-space impedance η to the fin impedance Z_{in}

MEASURED E-PLANE, EDGE VIEW OF FINS
MEASURED E-PLANE, BROADSIDE TO FINS ———
CALCULATED FROM TM_{11} MODE — — — — —

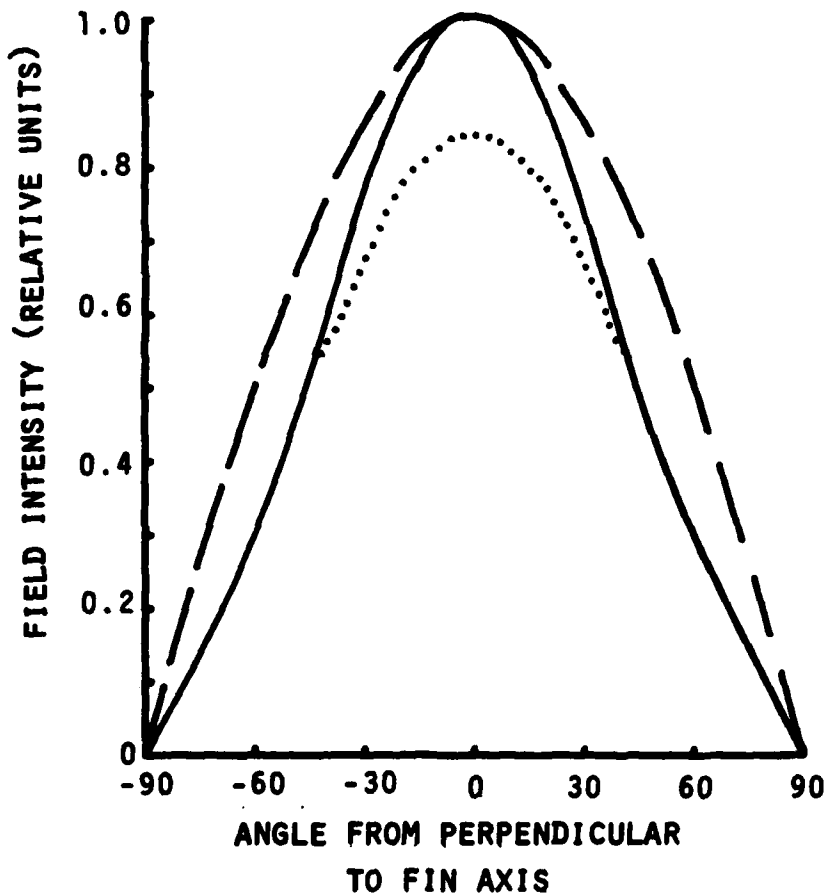


Fig. 11-5. Comparison of measured patterns of metal-only bowtie antenna of electrical length = 240° with calculated TM_{11} mode pattern.

is 1.5. When the resulting values of Z_{in} are plotted along with those measured by Brown and Woodward in Figs. 11-6 and 11-7, the agreement seen is quite impressive for such a simple model.

SUBHARMONIC MIXER USING THE BOWTIE ANTENNA

It has been shown both empirically and analytically that the metallic bowtie antenna has a broad frequency range over which its impedance is predominantly real. In this range, the radiation pattern is fairly well approximated by that of an elementary dipole. These properties make it especially suitable for use as the receiving antenna of a quasi-optical subharmonically-pumped mixer for the following reasons.

The mostly real terminal impedance over a 2:1 frequency range makes it easy to transfer power from the antenna to the mixer circuit at both f_{RF} and f_{LO} , which is about one-half of f_{RF} . A resonant structure such as a wire dipole or even a slot-ring antenna will generally have a much narrower usable bandwidth making it very difficult to receive both RF and LO energy without using separate antennas for each frequency. The relatively broad pattern of the bowtie meets the requirements of quasi-optical imaging service, as the slot-ring pattern did in Part I. While not rigorous, the simple one-mode theory developed for the bowtie accounts for the essential design characteristics of the device and furnishes a basis on which to found more elaborate analyses in the future.

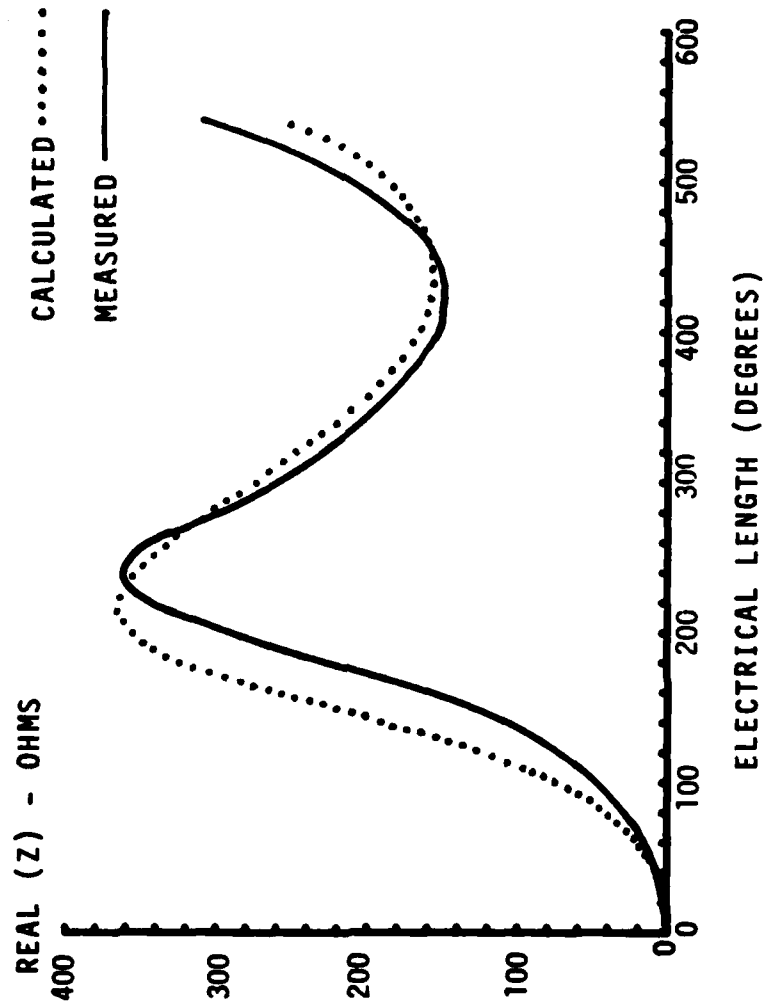


Fig. 11-6. Calculated and measured real part of metal-only bowtie antenna impedance versus electrical length.

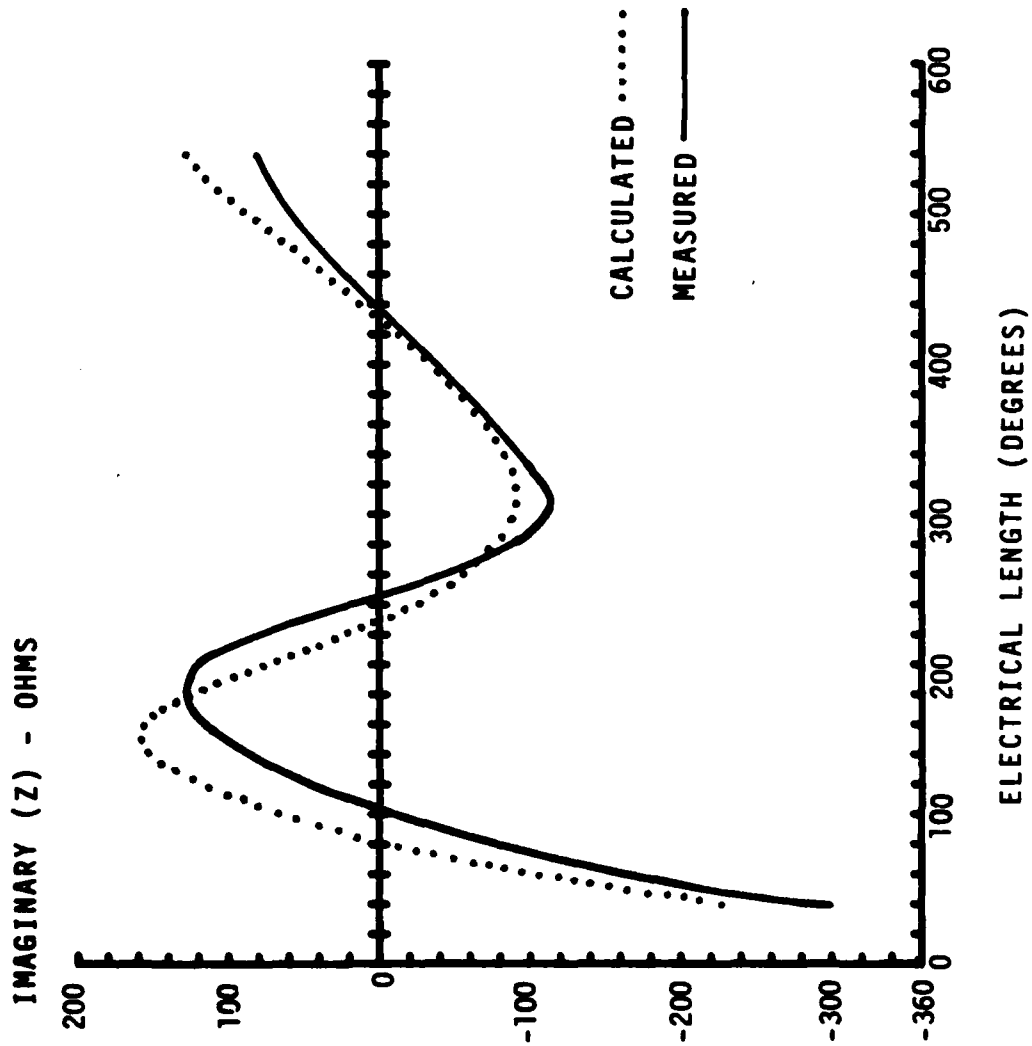


Fig. 11-7. Calculated and measured imaginary part of metal-only bowtie versus electrical length.

DIELECTRIC-SUPPORTED BOWTIE

In common with the slot-ring antenna, the bowtie antenna is mechanically awkward in its purely metallic form. The entire antenna mass is supported at the terminals unless some form of dielectric support is used. A practical version suitable for photolithographic fabrication is shown in Fig. 11-8. The bowtie structure is now supported on one side by a dielectric sheet. Several identical antennas were made with the following dimensions: width $W = 9.45$ mm, length $L = 22.6$ mm, and thickness $T = 1.57$ mm. The terminal spacing at the center was rather hard to control, but averaged about 0.4 mm. Antennas of these dimensions were used in all the antenna and mixer experiments. Angle $\psi = 30^\circ$.

As long as the usual precautions of avoiding high-order surface waves are observed, little difference in radiation patterns or impedance should be noted between the all-metal and the dielectric-supported structures. The impedance will show a slightly higher reactive part due to the greater amount of energy stored in the dielectric, but for dielectric constants typical of microwave substrates presently in use ($2 < \epsilon_r < 3$), the effect should be small. The pattern changes should be only a slight increase in the dielectric-side radiation, and measurements to follow confirm this. Using GaAs as a substrate would have a more marked effect because of its higher dielectric constant of about 13.

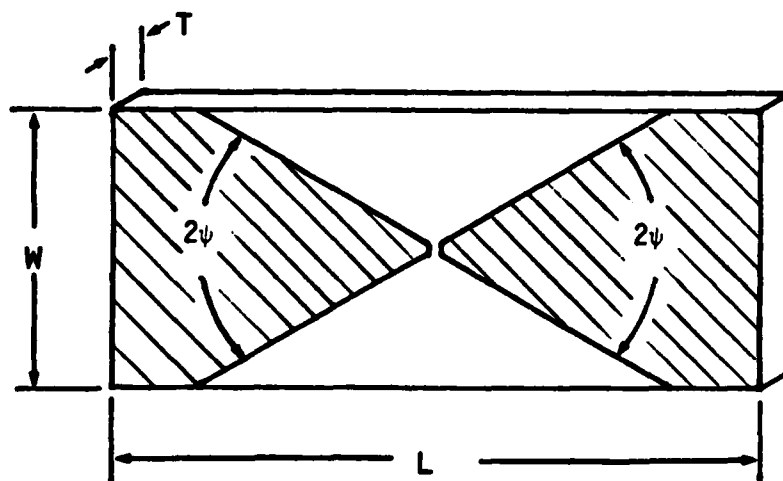


Fig. 11-8. Bowtie antenna on a dielectric substrate.

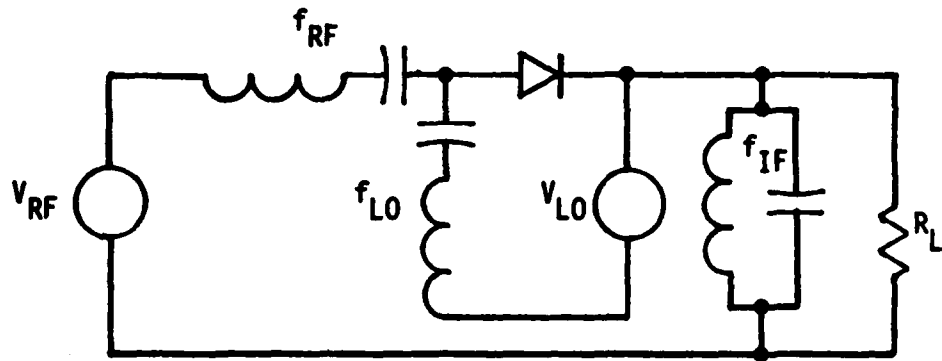
CHAPTER 12: SUBHARMONIC MIXER OPERATION

BACKGROUND AND THEORY

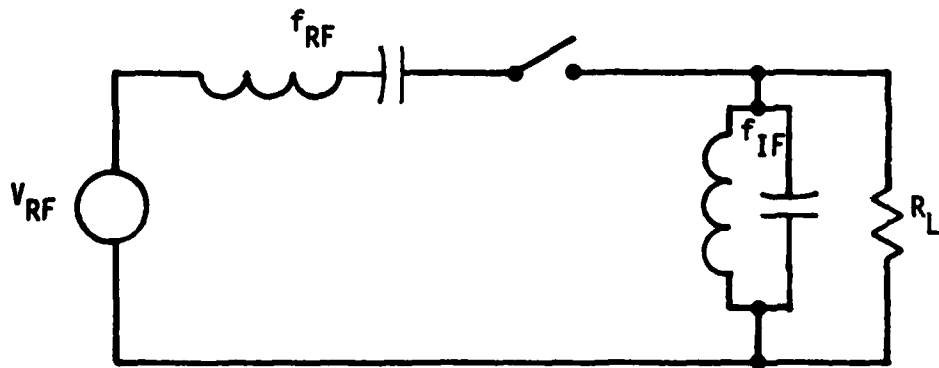
Although mixers using a harmonic of the pump frequency have been used for many years, their popularity has been limited by several drawbacks. Since most of them were merely conventional single-ended mixers driven hard enough to show adequate response near the desired LO harmonic, the conversion loss and noise performance was generally poor. The mixer circuit itself had no inherent rejection for any harmonic response so noise converted down from the many sidebands degraded the signal-to-noise ratio at the IF output.

Things began to change around 1974 when Schneider [1], Cohn [2], and others reported results from a type of mixer circuit expressly designed to be driven at a subharmonic of the usual LO frequency. The concept is quite simple and can be best explained in terms of the simplified view of mixer diodes as ideal switches.

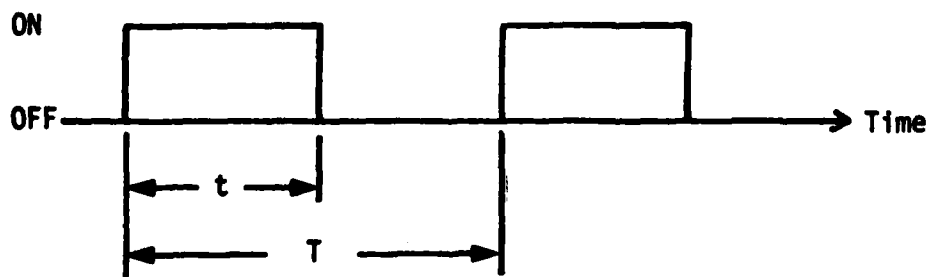
In Fig. 12-1 a simplified version of a single-ended mixer is diagrammed. The various bandpass filters have been idealized in the following way. The RF filter is a series tank circuit having infinite Q . This means that it behaves like a short circuit at the RF frequency and an open circuit at all other frequencies. The LO filter is similar, but tuned to f_{LO} . The IF filter is a parallel-tuned tank which is open at f_{IF} but shorted at all other frequencies.



(a)



(b)



(c)

Fig. 12-1. Equivalent circuits of conventional single-diode mixer showing: (a) diode (b) ideal switch (c) switch waveform.

If the drive power from the local oscillator is great enough, the diode behavior will be adequately modelled by a switch, and the LO circuit can be eliminated as in Fig. 12-1(b). An important factor in the operation of such a mixer is the switch duty cycle $\tau = t/T$, in Fig. 12-1(c). Although nothing too definite can be said about the relationship between the LO power and the effective duty cycle of the diode, some limiting cases are easy to derive. In the absence of LO power, the diode is off, or in a relatively high-resistance state. As LO power gradually increases, the diode turns on for an increasing percentage of the cycle, and the switch model becomes a good approximation.

In his thorough monograph on resistive mixers, Saleh showed [3] that the optimum duty cycle for such a mixer is $\tau = 0.5$. The circuit he used had more complex filters than those illustrated here, but the principle was the same. A duty cycle either greater or less than this led to increased conversion loss.

The circuit in Fig. 12-2(a) is a simple form of subharmonic mixer using an antiparallel diode pair. Antiparallel means that the diodes are connected together head-to-tail: when one is forward-biased, the other is reverse-biased. If the LO power is sufficient, each diode may be replaced by a switch, as in Fig. 12-2(b). Driving the antiparallel pair, an LO voltage of half the former frequency can yield the same switching waveforms as before. Note that because of the antiparallel connection, the diodes conduct on alternate half-cycles of the LO voltage, effectively doubling the number of switch times per LO cycle. The effects of this can be seen in Fig. 12-3, where the switching waveforms are shown.

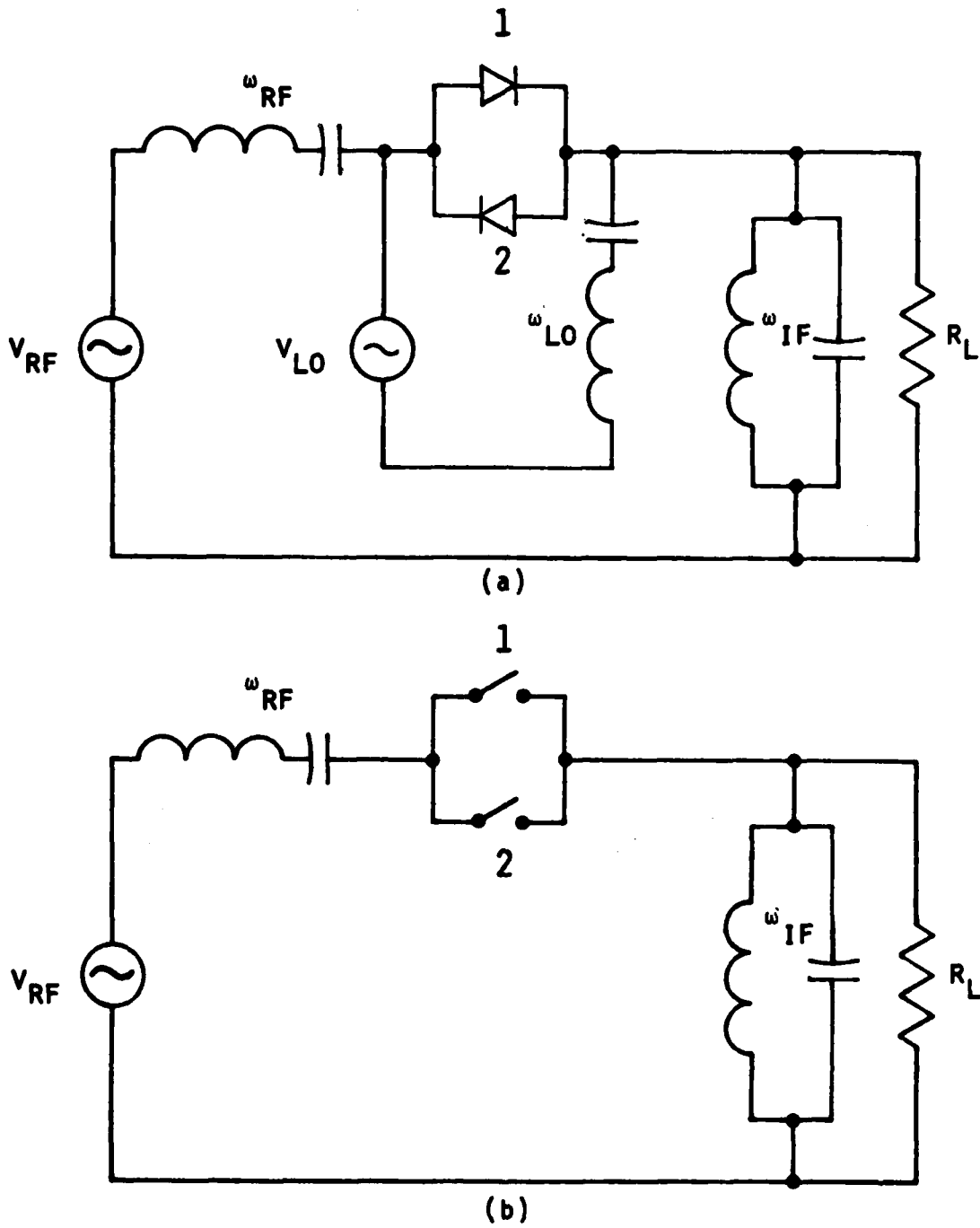


Fig. 12-2. Equivalent circuits of subharmonic mixer showing (a) diodes (b) ideal switches.

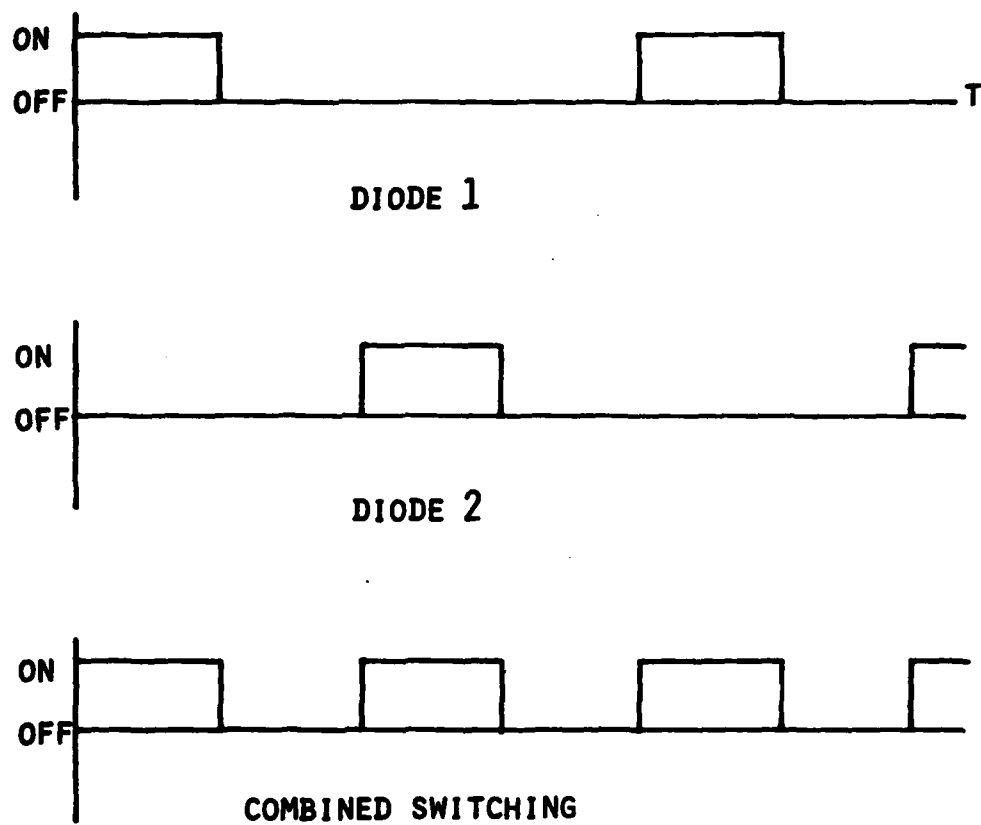


Fig. 12-3. Switching waveforms of subharmonic mixer.

A duty cycle of only 0.25 for each diode now gives an effective duty cycle of 0.5 for the mixer, since the diode switches are in parallel. Unlike the conventional harmonic mixer, the subharmonic mixer of Fig. 12-2 does not respond to signals near the LO frequency. This means that noise and signals in this range are rejected, improving the noise figure.

More elaborate theoretical work by Kerr [4] has followed the same path as single-ended mixer analysis. His study confirmed many of the advantages exhibited by the simple model just presented. In the same work, Kerr noted some precautions to be observed for best subharmonic mixer performance. Some of these caveats will now be discussed.

FACTORS IN SUBHARMONIC MIXER DESIGN

Most of the problems in subharmonic mixer design are the same that designers of conventional mixers must face. Diode series resistance has the same detrimental effect as it does in a conventional mixer, and should be reduced for the same reasons. Also, Kerr [5] showed that the loop inductance of the path between the diodes has a more marked effect on the subharmonic mixer's performance than an equivalent inductance has on the conventional mixer. For certain inductance values, Kerr's computer model showed a resonance which caused each diode to conduct twice per cycle, leading to greatly increased conversion loss. Whether this effect is of significance in practice remains to be seen, but it is worth bearing in mind during design. Beam-lead diodes, if used, should be mounted so as to reduce the lead inductance to an abso-

lute minimum.

A feature that makes subharmonic mixer circuitry easier to design is the wide separation between RF and LO frequencies. This greatly eases the task of designing separating filters and is advantageous even when quasi-optical techniques are used.

Finally, there is the possibility of reduced LO power requirements in addition to the lower LO frequency needed with subharmonic operation. As we have seen, a lower duty cycle compared to conventional mixer operation can yield good mixer performance in the simple model considered, and lower incidental losses at the lower LO frequency make it easier to deliver a given amount of power to the diode junctions. These desirable properties of the subharmonic antiparallel-diode mixer were explored in the series of experiments described in the following chapters.

CHAPTER 13: BOWTIE ANTENNA MEASUREMENTS

The same basic procedure used with the slot-ring antenna was followed to establish a directivity figure for the bowtie antenna. Since the experiments of Brown and Woodward showed that the antenna impedance changed so slowly over a broad frequency range, we decided not to construct low-frequency models for impedance tests. Instead, we designed the dielectric-supported bowtie shown in Fig. 11-8 for the intended frequency of operation: 14 GHz. The bandwidth we desired to cover was about 7 to 14 GHz since a powerful LO source was available at 7 GHz. Unlike the patterns of the slot-ring antenna, the bowtie antenna's field patterns are not separable into independent functions of θ and ϕ . This meant that the two conventional E-plane and H-plane patterns would not suffice for performing the numerical spherical integrations needed. A reasonable compromise permitting sufficient accuracy with a reasonable number of measurements is shown in Fig. 13-1.

Suppose that the bowtie antenna is radiating and the measurement point is moved along the line labeled $\delta = 0^\circ$. This is the so-called E-plane plot, since it is parallel to the dominant polarization vector of the antenna. Next, let the measurement plane be tilted so that now $\delta = 30^\circ$. Because of the asymmetry of this path with respect to the antenna, electric field measurements both parallel and perpendicular to the measurement plane must be made if the total power density along the circle is desired.

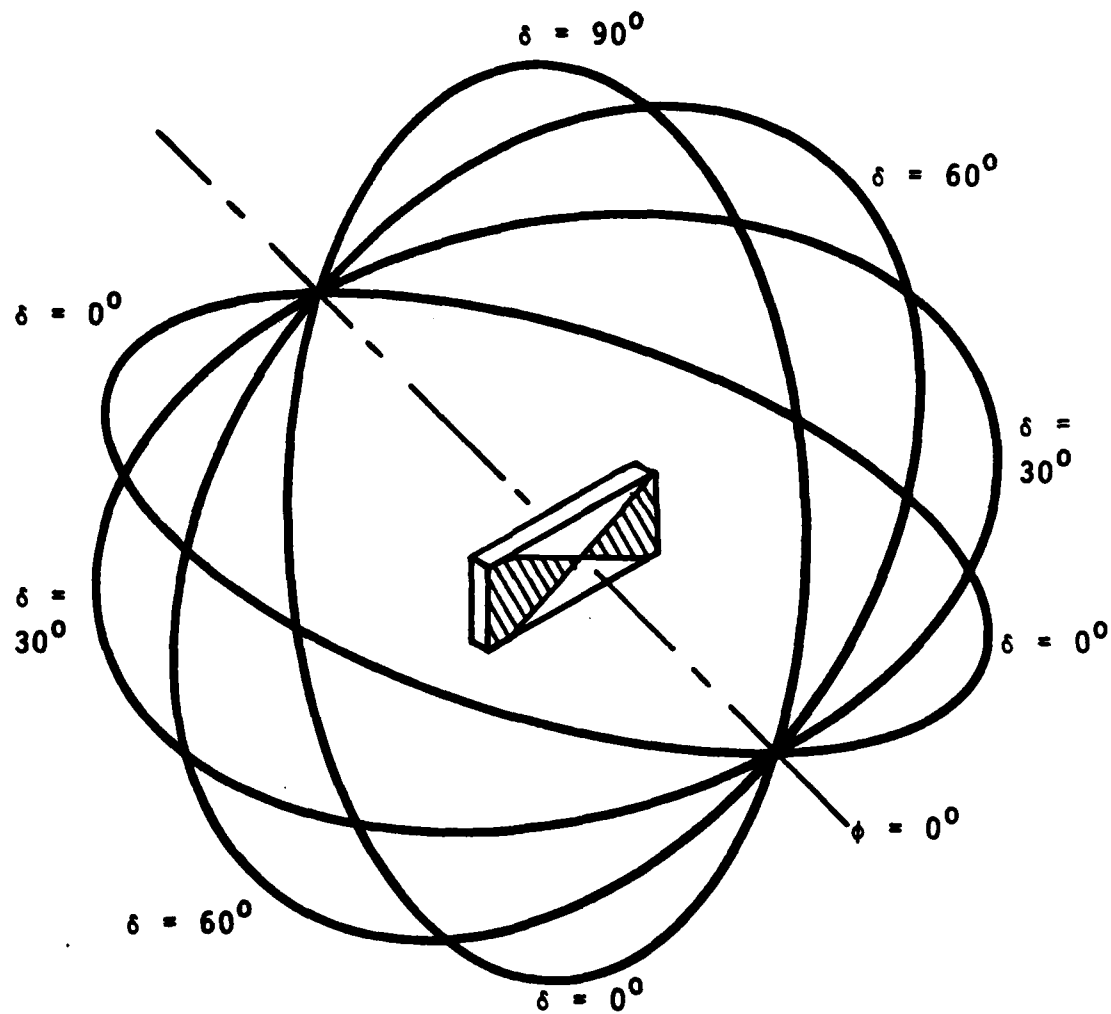


Fig. 13-1. Plan of radiation pattern measurements for bowtie antenna.

Continuing in this way, we tilt the measurement plane an additional 30° to $\delta = 60^\circ$, and the power density along this circle is measured. Measurement along the $\delta = 90^\circ$ circle gives the H-plane pattern. No circles are shown for $\delta = 120^\circ$ or $\delta = 150^\circ$, because the bilateral symmetry of the bowtie assures us that the data would be identical to the $\delta = 60^\circ$ and $\delta = 30^\circ$ circles, respectively. In this way, the sphere of measurement is girdled by eight circles along which the power density is known. The two polar points common to all of the circles are regions of strong intensity, where relative calibrations for the various circles may easily be established. The slot-ring radiation patterns of Part I were taken by hand at 10° or at best 5° intervals. Automation of the measurements for the bowtie antenna increased resolution to 1° or better. This gave 2160 data points per spherical integration which is probably more than sufficient for good accuracy.

The improved radiation pattern setup is shown in Fig. 13-2. As in the previous measurements, a wave analyzer was used to monitor the audio-frequency output of the antenna's detector diode when it was irradiated by modulated RF energy. The output of the wave analyzer was proportional to the logarithm of the AC input amplitude, so a range of 50 to 60 dB was easily compressed to fit within the 0-10 volt output of the analyzer.

Instead of manually maintaining a fixed level as in the past, the varying wave analyzer output was fed to the Y input of an X-Y plotter. We replaced the manual antenna rotator with a motorized one having a ten-turn precision potentiometer geared to the platform. The potentiom-

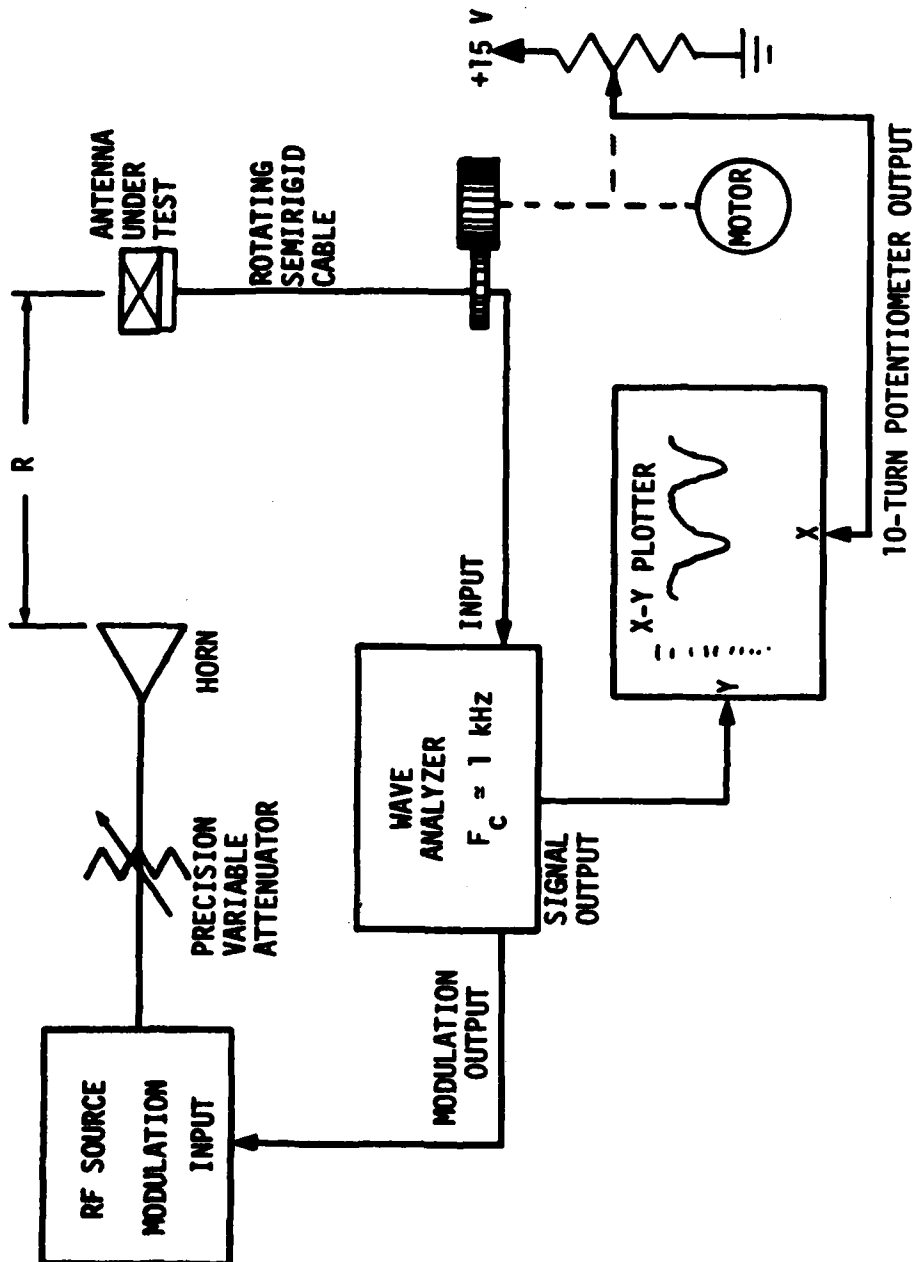


Fig. 13-2. Bowtie antenna radiation pattern measurement apparatus.

eter produced a DC voltage proportional to antenna rotation, which drove the plotter's X-axis. As the antenna turned, the varying detector output traced a continuous record of relative output versus azimuth.

To make the plots thus obtained readable in decibels, calibration points were taken every 2.5 dB, from the maximum output down to the noise floor of the system. These points were made by positioning the antenna for maximum output and setting the precision variable attenuator to 0 dB (no attenuation). A mark was made at this level on one side of the X-Y plot, the attenuation increased by 2.5 dB, another mark made, and so on. This created a series of calibration levels between which the continuous record could be interpolated. The X-axis azimuth coordinate was linear by virtue of the potentiometer's linearity, but an ambiguity remained as to the location of the zero-degree direction. This was remedied by causing a cam-operated switch to lift the plotter pen once each revolution at exactly the same angular position. By dividing the horizontal distance between pen-lifts into 360 parts, we calibrated the X-axis in degrees. An example of the raw data generated by this method is given in Fig. 13-3.

The tedium of manually taking numbers from such raw data would be little improvement over completely manual measurements so the digitizing feature of an HP-85 desktop computer was set to work. By following the raw curve with the plotter's cursor we could reduce a data sheet to a set of 360 linearly interpolated data points in the computer memory in about five minutes. Once in memory, the data could be used either to perform the spherical integrations or to generate polar plots. Fig. 13-4 is the

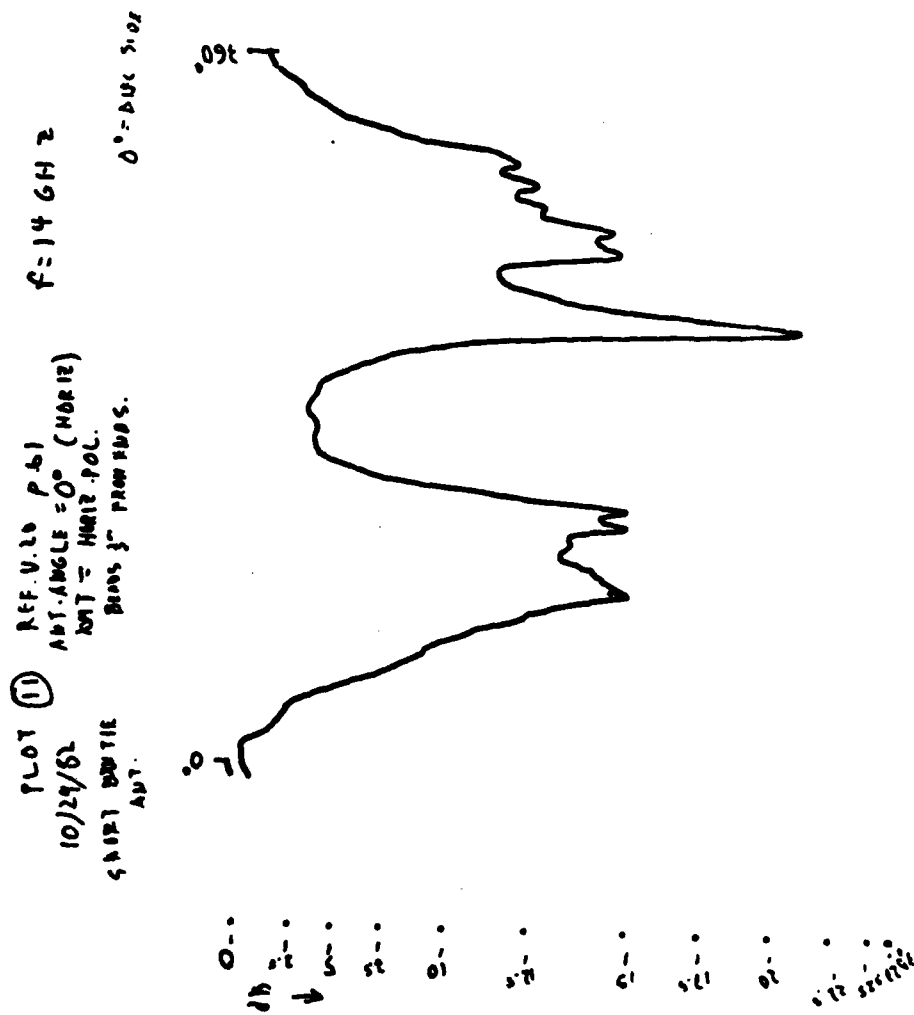


Fig. 13-3. Raw plot of bowtie antenna radiation pattern.

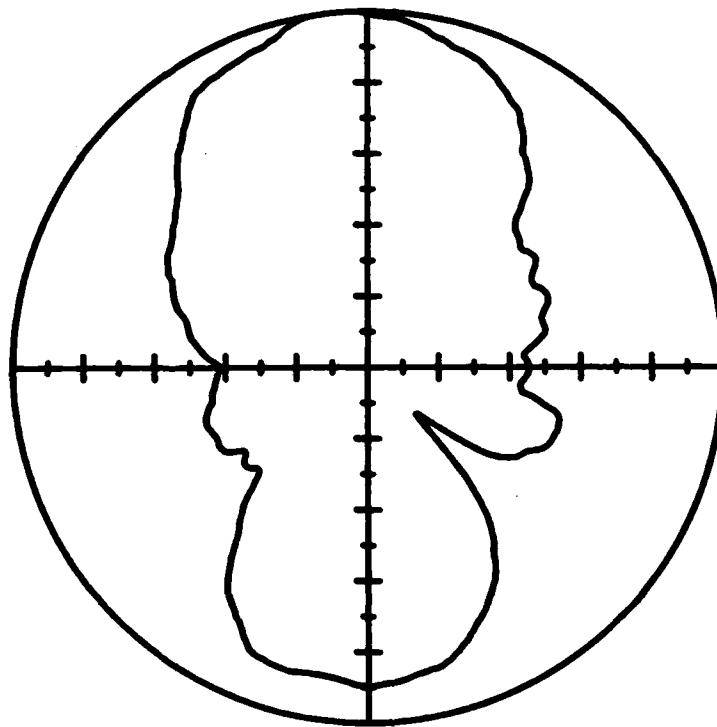


Fig. 13-4. Data of Fig. 13-3 as processed and plotted by HP-85 computer.

data of Fig. 13-3 reduced to polar form. No great advance in antenna measurement technology is claimed for this system, but it is a good example of what can be done when there is no money in the budget for analog-to-digital converters.

Patterns were taken at 7 and 14 GHz. Fig. 13-5 superimposes the E-plane patterns for those two frequencies, and Fig. 13-6 shows the H-plane patterns. As before, all patterns are dB down from maximum, so no conclusions may be drawn from these plots about the relative sensitivity at the two frequencies. The eight spherical integration patterns (four vertical polarization and four horizontal) were made by tilting the bowtie in its styrofoam support, but the effect was the same as if the measurement system were tilted instead, as in Fig. 13-1. Some slight ripples in the patterns were traced to reflections from the edges of the rotating table, but because integration is an averaging process, these were felt to be inconsequential. The directivity at 14 GHz was calculated on the dielectric side to be 4.5 dB with respect to an isotropic radiator. This gives good agreement with Brown and Woodward's value of about 4-5 dB for their metallic fin antenna at the equivalent frequency.

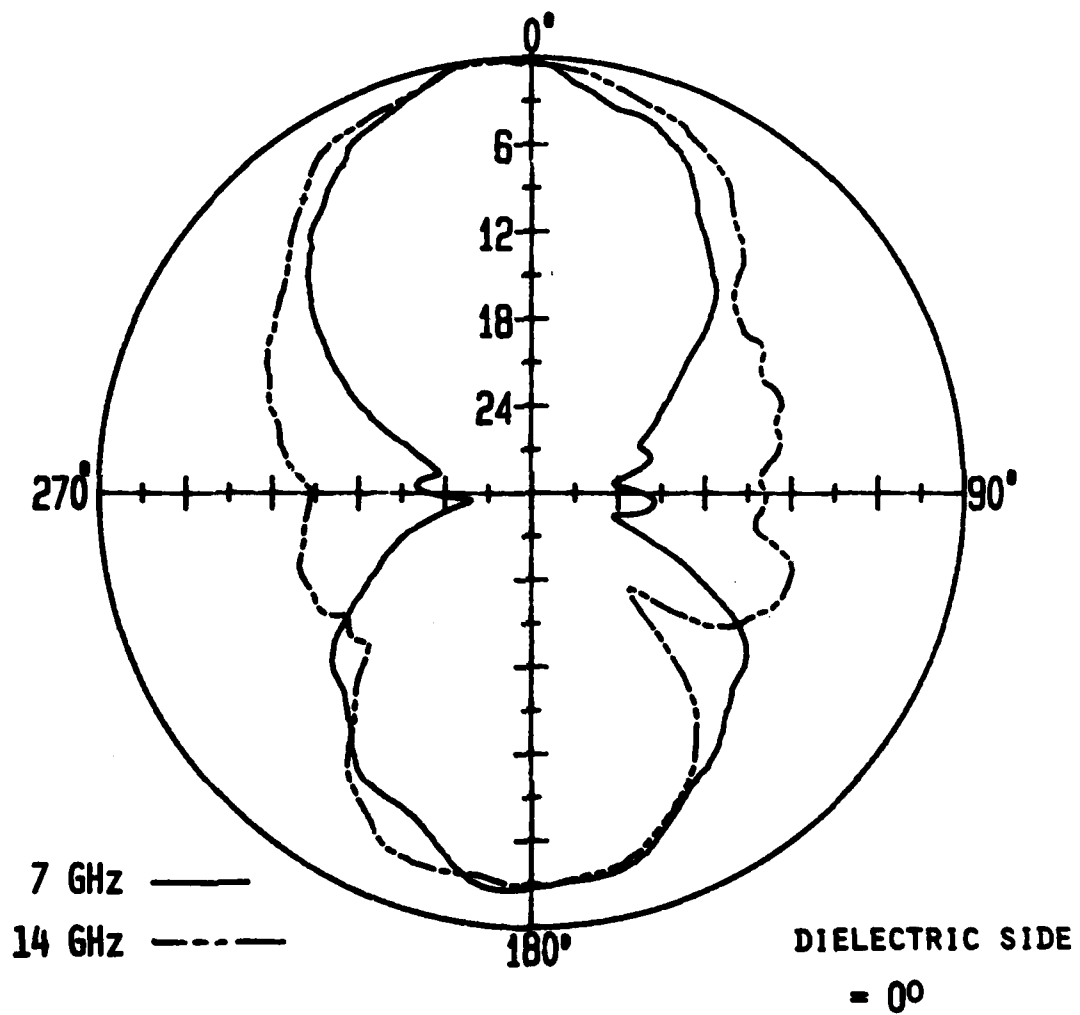


Fig. 13-5. E-plane patterns, 7 and 14 GHz,
bowtie antenna.

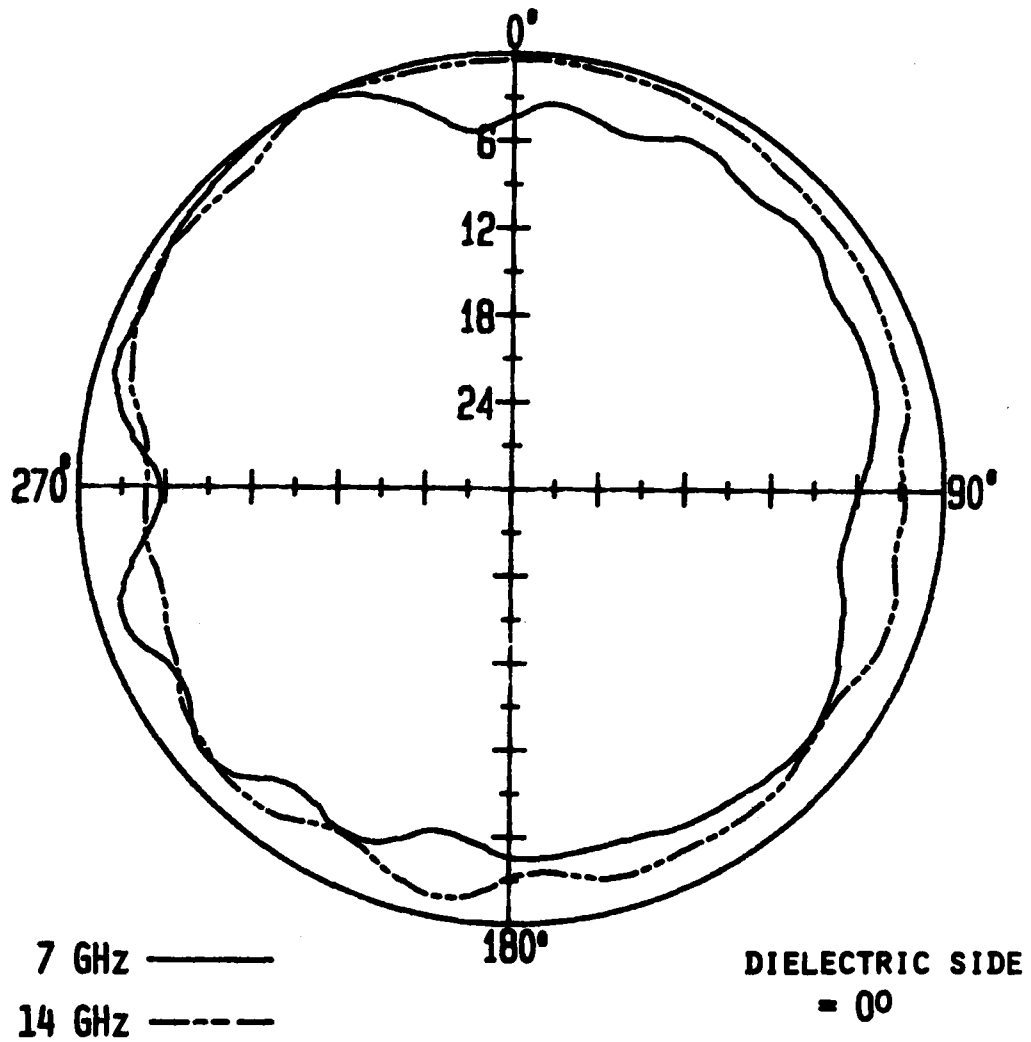


Fig. 13-6. H-plane patterns, 7 and 14 GHz,
bowtie antenna.

CHAPTER 14: MAKING THE BOWTIE MIXERS

Before discussion of the bowtie mixer tests, we shall outline the methods used to make them. The bowtie structures used in both the antenna pattern and mixer experiments were made by etching masked strips of copper-clad microwave substrate material. Although photolithographic techniques could have been used, we found that a simpler method sufficed. A mask was made by cutting adhesive plastic film in the desired pattern. It was then applied to the copper side of the substrate. Exposure of the unprotected copper to ammonium persulfate etchant produced several usable antennas, with the only problem being that the central tips forming the terminals were not separated, causing a short. Applying a charged 4000 μ F capacitor to the opposite ends of the antenna usually cleared the short neatly, leaving slightly fused copper terminals separated by a gap averaging 0.4 mm across. Too small a gap might short the metallization on the diode, but too wide a gap would leave the diode's leads exposed for their full length, adding to the series inductance.

After several unsuccessful tries, both one- and two-diode mixers were made by soldering the diodes across the gaps in two antennas. The entire procedure was carried out under a 30-power stereoscopic microscope since the diodes were only about 0.7 mm long and 0.3 mm wide! Soldering was achieved by first tinning the antenna terminals with indium solder. Then the substrate was cooled, the diode or diodes placed in the desired position on top of the tinned terminals with a little flux,

and the entire assembly heated again on a hotplate just above the solder's melting temperature of about 150°C. As soon as the solder wetted the diode leads, the substrate was gently but quickly removed from the hotplate to cool it. Any attempt to manipulate the diodes while the solder was molten generally led to disaster, since the solder's surface tension exhibited a powerful pull on the diodes. Also, the substrate used tended to become gummy at soldering temperatures. Future work should use a Teflon® substrate such as RT-Duroid® which does not soften below about 250° C. Once mounted, the diodes are sensitive to static discharges and power line potentials from ungrounded equipment, as we found to our grief. Fig. 14-1 is a photograph of two diodes mounted at the bowtie terminals.

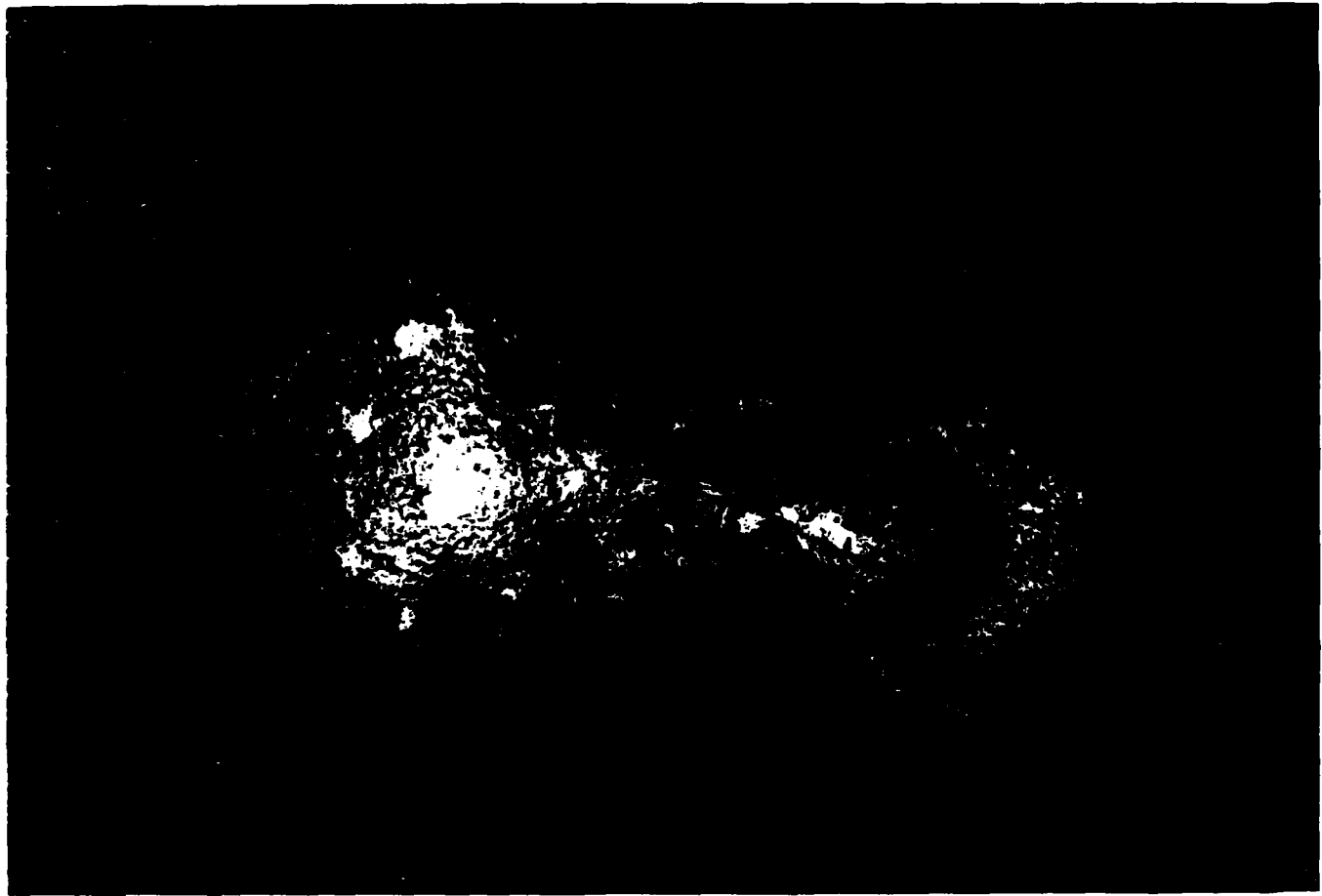


Fig. 14-1. Photograph of diode pair at
bowtie antenna terminals.

CHAPTER 15: BOWTIE MIXER EXPERIMENTS

14 GHZ TESTS

Only minor modifications were made to the conversion loss measurement method described in Chapter 6. Additional measurements were made to determine gains of the horns used at 14 GHz, and a low-noise GaAs FET IF amplifier was obtained. This allowed an IF in the 300-450 MHz range, eased the oscillator stability requirements, and made the IF matching network more compact. Difficulties in obtaining sufficient LO power led to very short mixer-LO horn distances. This had the unfortunate effect of distorting the antenna pattern and altering the effective directivity of the mixer from its free-space measured value. In light of this problem and the impracticality of measuring spherical patterns of the bulky mixer-LO feed system, a case is made in Chapter 16 for adopting effective mixer aperture as the criterion of quasi-optical mixer performance. To measure either conventional conversion loss or effective mixer aperture, one requires a mixer test arrangement similar to the one we shall now describe.

Fig. 15-1 shows the setup used for the 14 GHz measurements. Starting from the left, the RF signal in the 13-14 GHz range was fed through a variable attenuator to a pair of calibrated directional couplers. The purpose of these was twofold. First, measurement of power at R gave the amount of power radiated from horn #1. By adjusting the

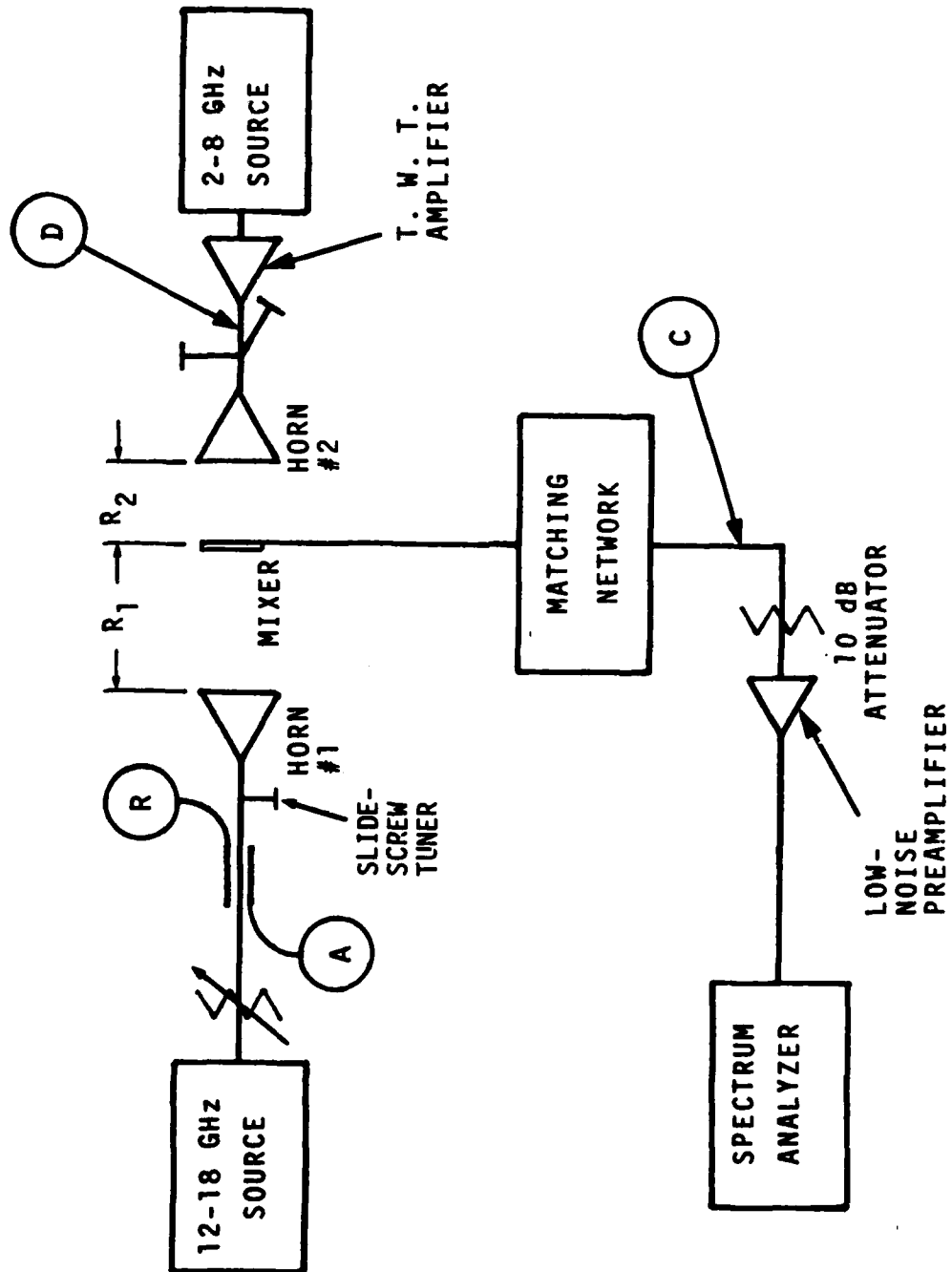


Fig. 15-1. Apparatus for 14 GHz conversion loss measurements.

slide-screw tuner and monitoring the reflected power at A, we determined that virtually all the incident power was in fact radiated by the horn. The horn gains were measured by the three-antenna method [1]. Knowing the radiated power and the transmitting antenna gain, we easily calculated the intensity at the mixer distance R1 without needing to actually receive the power with another horn.

The LO energy from a 2-8 GHz sweep oscillator was amplified by a traveling-wave-tube amplifier and fed through an E-H tuner to LO horn #2. Approximate determination of LO power used could be made by inserting a power meter at point D.

The bowtie mixer was mounted on a piece of semirigid coaxial cable by two wires forming a fork or yoke. Both one- and two-diode units were tested to observe the improvement in mixer performance by direct comparison. To avoid pickup of the RF fields by the support wires, a ferrite bead was mounted on each wire. Experiments showed these beads to have little effect on IF currents below 1 GHz, but they substantially reduced microwave pickup. The goal was to cause the bowtie antenna to have the same radiation pattern as it did during the pattern measurements, but it is likely that this goal was only partially met.

The IF current went through the semirigid cable to the IF matching network, whose schematic is shown in Fig. 15-2. The combination of pi-network and series-shunt stub matching enabled a conjugate match to be obtained for any impedance in the shaded region of the Smith chart in Fig. 15-3. Since the IF impedance of a mixer is usually mostly real and between 20 and 200 ohms, this network was judged more than adequate for

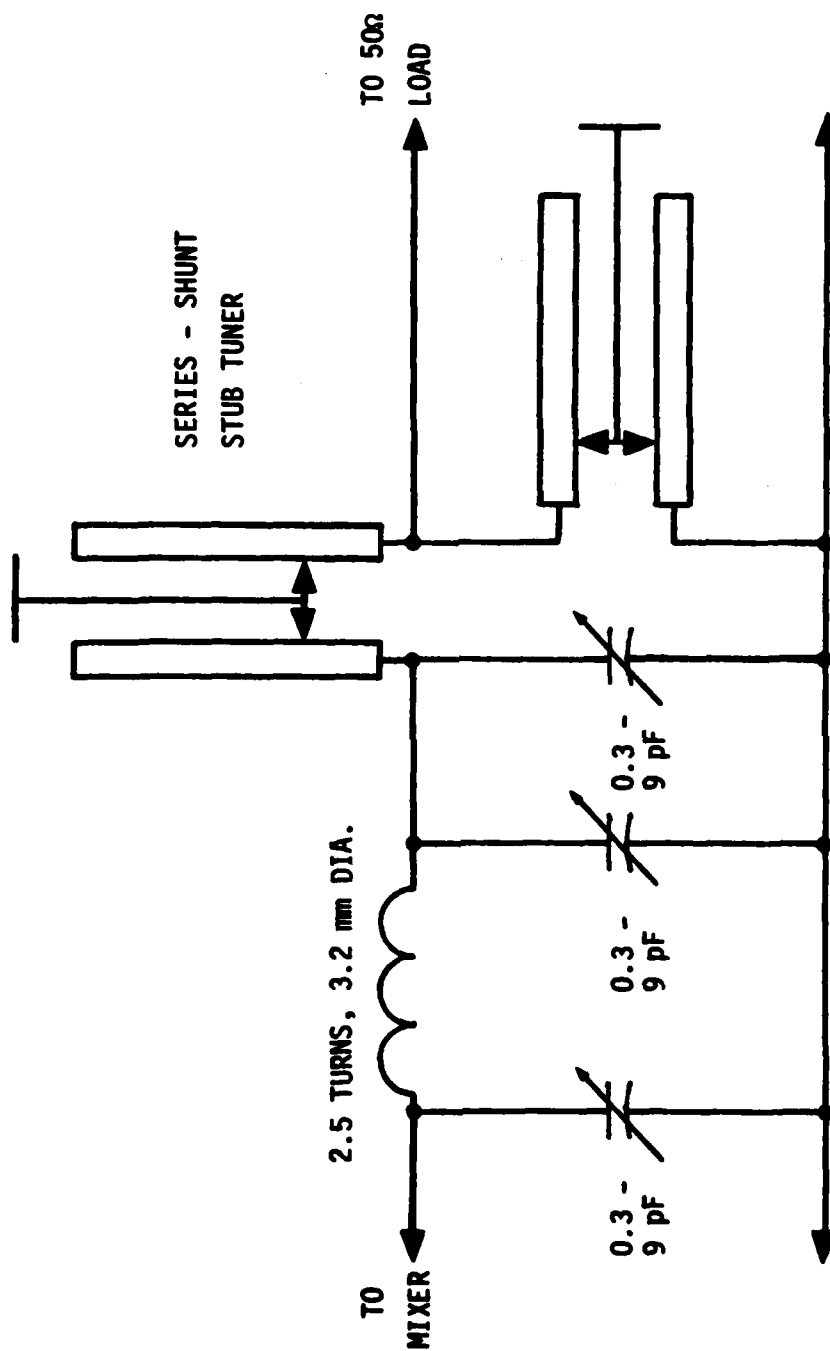
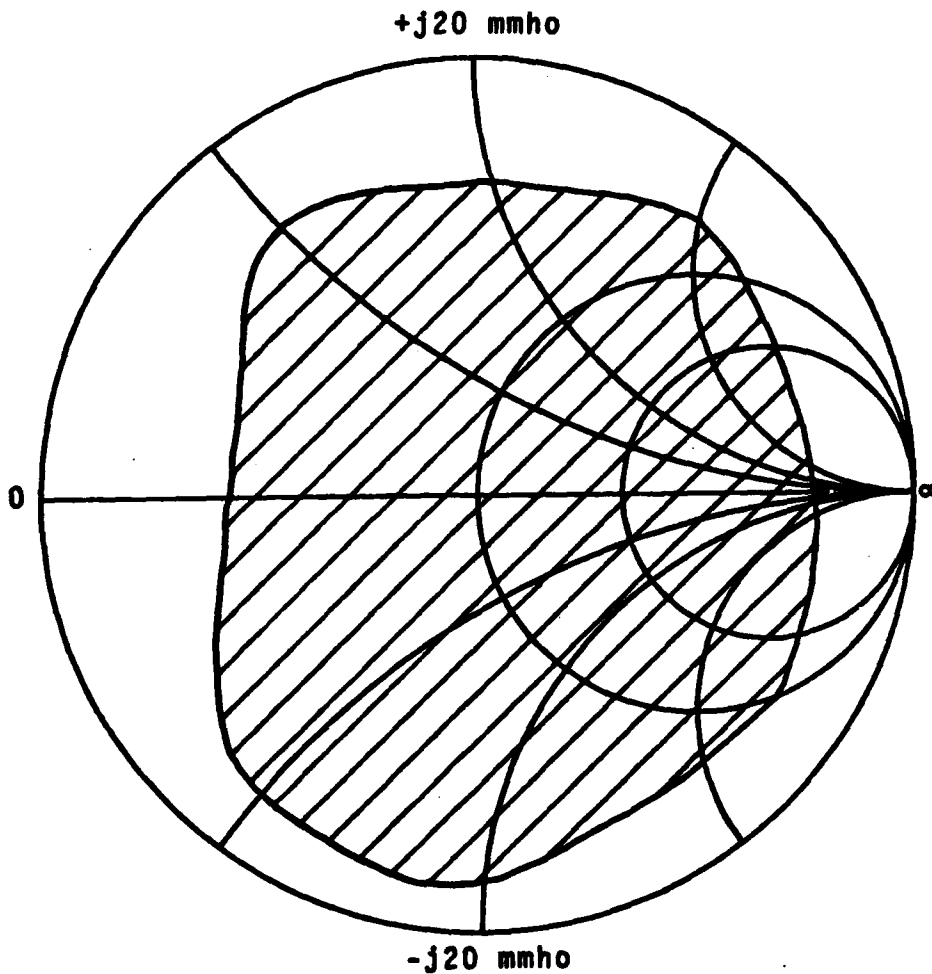


Fig. 15-2. Matching network used in bowtie mixer conversion loss experiments.

ALL ADMITTANCES WITHIN HATCHED REGION
CAN BE CONJUGATELY MATCHED BY NETWORK



ADMITTANCE COORDINATES NORMALIZED TO 20 mmho

Fig. 15-3. Impedance-matching capability of
matching network in Fig. 15-2 at 400 MHz.

the task. Its insertion loss of 0.3 dB was corrected for in the conversion loss calculations of the next chapter.

To ensure that power was delivered to a known load resistance, we inserted a 10 dB fixed attenuator between the matching network and the low-noise IF amplifier. The very poor return loss of the amplifier input (less than 3 dB) made this configuration necessary, unfortunate as it was from a sensitivity point of view. The attenuator presented a 50-ohm load to the matching network within narrow limits, and rendered the input impedance of the amplifier largely irrelevant. Its ~2 dB noise figure maintained adequate sensitivity in the face of attenuator losses.

To perform a measurement, we adjusted the RF and LO frequencies to give a desired IF output frequency and measured the power at R while making sure the reflected power at A was negligible. After the relative IF output level on the spectrum analyzer was noted, the IF path was interrupted by substituting a calibrated signal generator at point C. Its output level and frequency were adjusted to give the same indication on the analyzer as the actual IF output, and the generator's power was then measured. Measuring the substituted power with the same meter used for the microwave measurement rendered absolute power standards unnecessary, since only the ratio of powers on the same meter was desired. Direct measurement of IF power at point C was impractical because of out-of-band interference, mostly from UHF TV stations. A broadband power meter at point C would see these signals and give erroneous readings, while the method used essentially calibrated the spectrum analyzer at the IF frequency of interest. Discussion of the data obtained will be

deferred to the next chapter.

35 GHZ TESTS

The only differences between the arrangement for 14 GHz tests and those at 35 GHz concerned the sources and horns used. The LO source of Fig. 15-1 was unchanged except for the substitution of a 12-18 GHz sweep oscillator for the 2-8 GHz unit. Although the traveling-wave-tube amplifier's specified frequency range was only 7.0-12.4 GHz, it still showed some gain at the intended LO frequency of 17 GHz, so it was left in the circuit. The LO horn used in the 14 GHz experiments had an elliptical aperture of about 10 cm X 14 cm. To increase the available LO power density, a smaller horn with an aperture about 2.5 cm X 3 cm was used for the 35 GHz work. The smaller aperture was a better physical match for the small bowtie mixer. Fig. 15-4 is a photograph of the LO horn behind the mixer. The stub tuner shown was used to obtain maximum power transfer to the horn, which was being used somewhat above its design frequency.

The RF signal source was a klystron protected by an isolator, with a directional coupler for continuous monitoring of the transmit horn's radiated power. A wavemeter was also included in the signal path. The RF source-mixer distance R1 was reduced to 61 cm, which was still in the far field of the smaller Ka-band horn used.

A very useful innovation in the 35 GHz setup was made by substituting a bias tee for the stub tuner in the IF matching network (Fig.

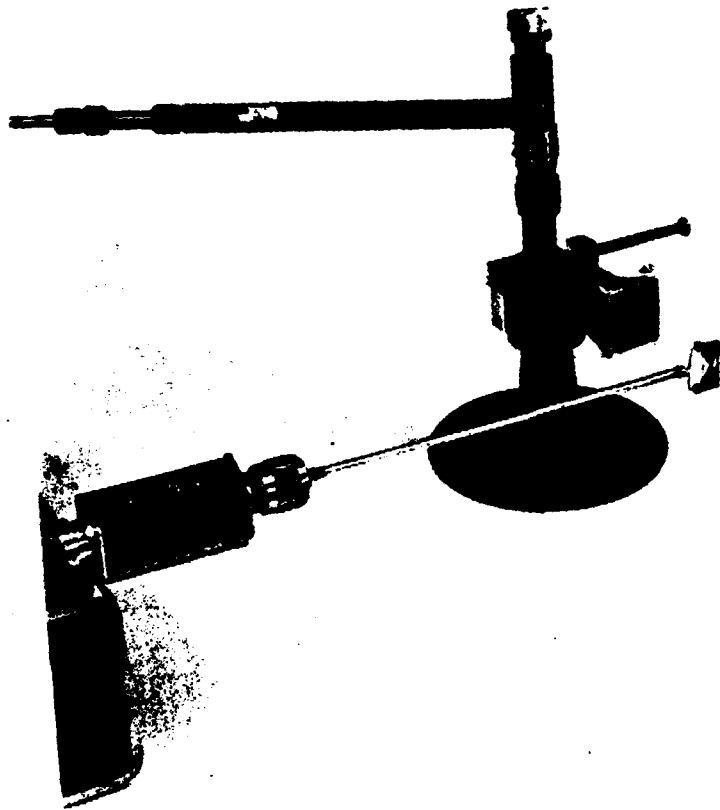


Fig. 15-4. Photograph of bowtie mixer in front of LO horn.

15-5). The pi network alone matched the mixer impedance well, and the bias tee now allowed the connection of a curve tracer to the diodes.

The absence of external DC bias current in this type of subharmonic mixer is generally regarded as an advantage, but one drawback is that the rectified current cannot be used as a relative indication of LO power delivered to the diodes. Workers at Hughes Aircraft [2] get around this problem by using a curve tracer to place a low-frequency AC voltage on the diodes. With no LO excitation, the I-V relation thus obtained is just the juxtaposition of the two diodes' individual curves. Fig. 15-6 shows a series of curves taken with various LO powers delivered to the small horn described above. The curve labeled NO LO POWER was taken without LO excitation, and shows the exponential relations typical of low-barrier Schottky diodes. The diodes used in the 35 GHz experiments were HP 5082-2264 types, which have a slightly lower specified capacitance than the HP 5082-2299 variety used at 14 GHz (0.1 pF as opposed to 0.15 pF).

As the LO power increased in 3 dB steps beginning with -5 dBm, the slope of the curve at $I = 0$ started to rise, indication that the slight forward current in each diode was decreasing its effective dynamic resistance. For higher powers, the resistance continued to fall, and the region of linearity about $I = 0$ extended until for +10 dBm the curve was that of a 30-ohm resistor, up to the maximum measured current of 5 mA. This state of affairs indicated that each diode was so forward-biased during its conduction cycle that the junction resistance was negligible compared to the series resistance of about 30 ohms, which

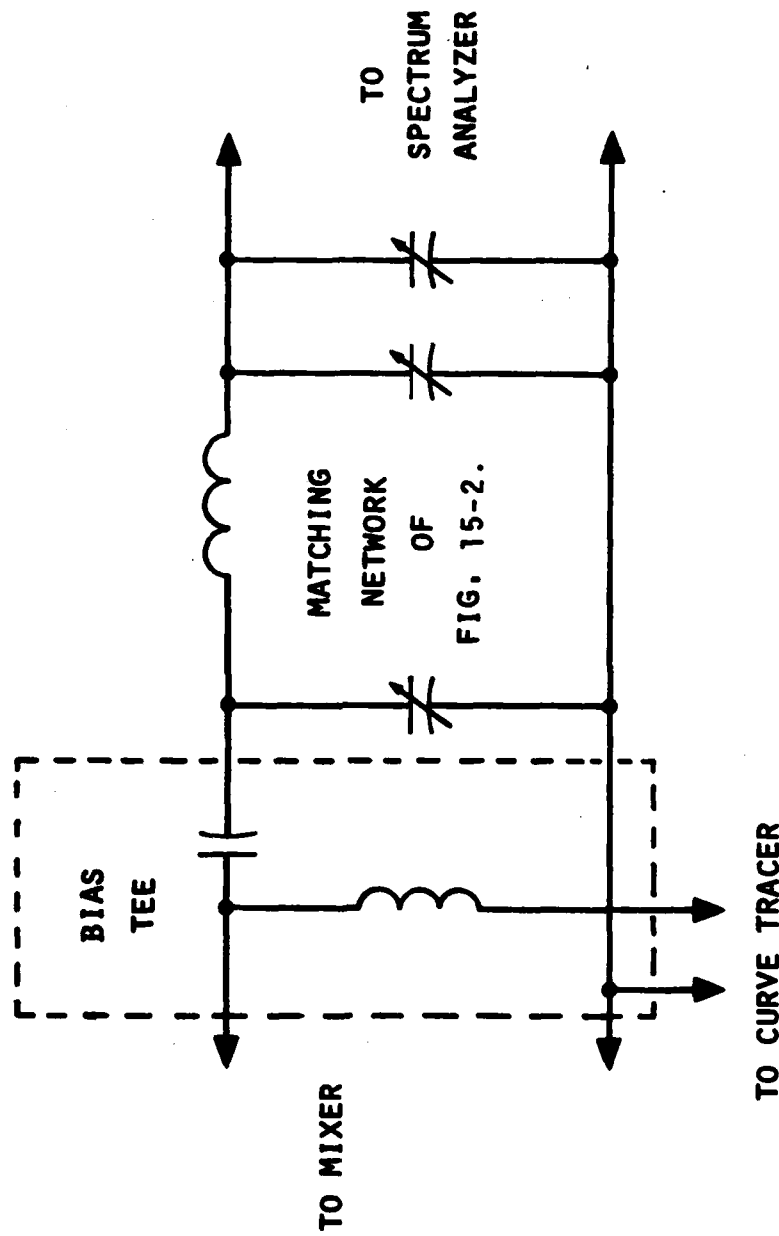


Fig. 15-5. Circuit used for impedance matching and DC diode tests in 35 GHz conversion loss work.

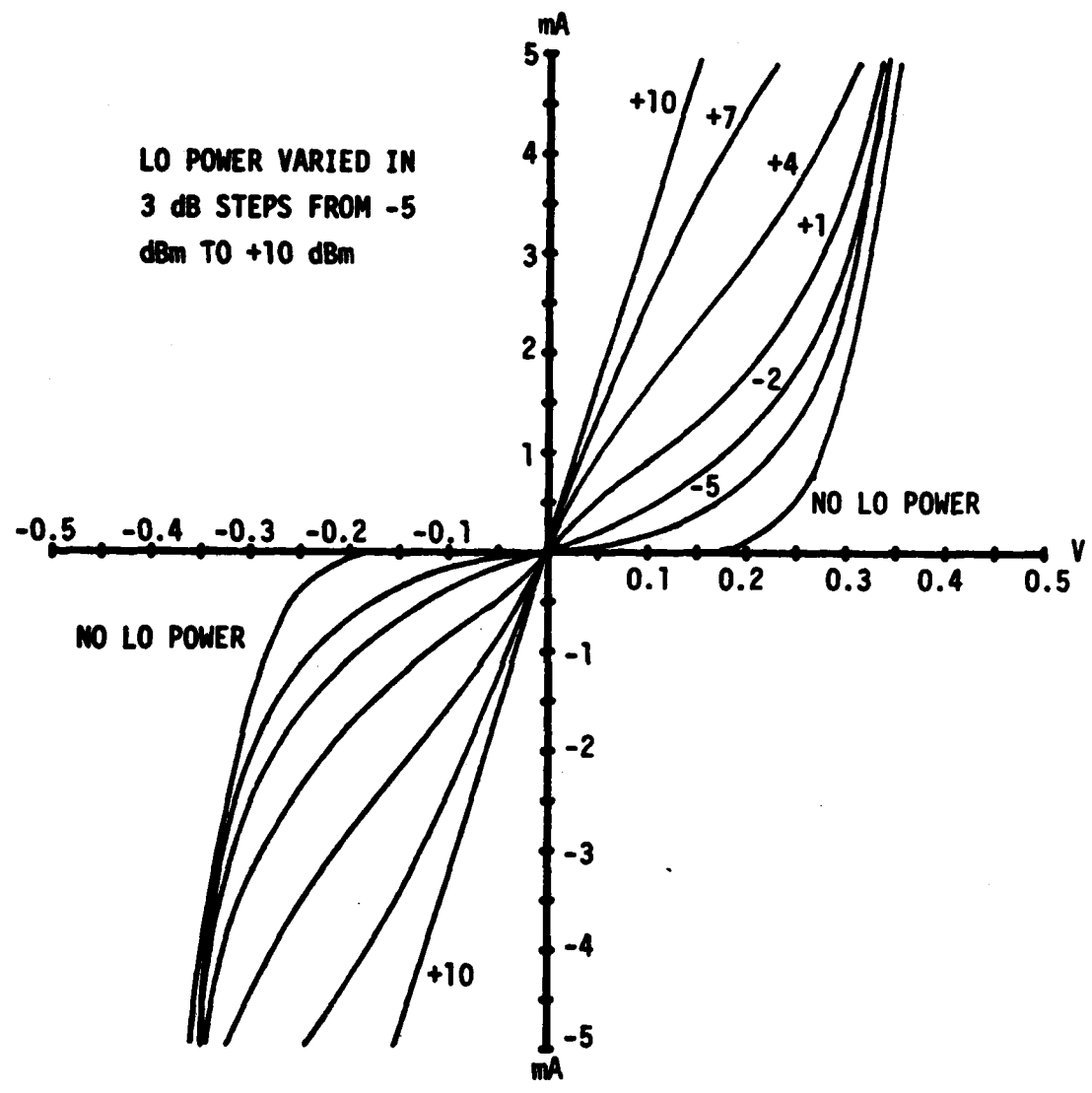


Fig. 15-6. Current-voltage characteristics of bowtie mixer with power delivered to LO horn as parameter.

is a limiting value for each diode. Such high drive power implies a duty cycle approaching 0.5, which is higher than the optimum value of 0.25 for the simple switch model of a subharmonic mixer. The experiments confirmed that the LO power for optimum conversion loss gave an I-V curve more like the one for -2 dBm in Fig. 15-6. It should be noted that the curve tracer was disconnected during actual conversion loss tests, since the AC voltage would cause severe modulation of the IF signal.

The I-V curve gives an unequivocal indication of the relative LO power reaching the mixer. A given power level can be repeated at will by adjusting the incident power and LO horn-mixer distance R2 to give the same I-V curve. The distance R2 has two independent effects: (1) it varies the LO power delivered to the mixer in a rather complicated way, and (2) reflections from the LO horn lead to variations in available RF power at the mixer terminals. Both (1) and (2) influence the IF output level, and so adjustment of R2 for minimum conversion loss becomes a complex business, especially if no IF output is initially visible. Since the curve tracer furnishes an independent means of monitoring LO power, the adjustment procedure is considerably simplified.

Lacking a suitable 35 GHz detector diode with which to make Ka-band pattern measurements, we made no directivity measurements at 35 GHz. Nevertheless, the conversion loss data can be used to find the mixer's 35 GHz effective aperture, which is probably a better indicator of quasi-optical mixer performance. Before discussing results of both the 14 GHz and the 35 GHz tests, we shall treat the problems involved in quasi-optical mixer measurements. The solutions we found follow in the next chapter.

CHAPTER 16: METRICS FOR QUASI-OPTICAL MIXERS

DIFFICULTIES IN MEASURING QUASI-OPTICAL MIXER CONVERSION LOSS

As in any antenna experiment involving distances of more than a few wavelengths, a high degree of repeatability was not always attainable. In these experiments, the positioning of the LO horn behind the mixer was especially critical since RF reflections from it can cause available RF power variations of ± 3 dB or more. Since this effect is so unpredictable, no attempt has been made to correct for it although it represents a significant source of error if accurate conversion loss figures are sought.

EFFECTIVE MIXER APERTURE

The difficulty of determining available RF power can be entirely avoided by quoting quasi-optical mixer performance in terms of effective mixer aperture A_q . Effective mixer aperture is merely an extension of the concept of effective antenna aperture A_e . If P_{RF} is the power delivered to the load of an antenna irradiated with a power density I_{RF} , the effective antenna aperture A_e is

$$A_e = P_{RF}/I_{RF}$$

(16-1)

Dividing power by power per unit area gives an area which can be thought of as the aperture of a hypothetical antenna that absorbs 100% of the power entering its aperture. Since all real antennas have internal losses and hence deliver less power than they absorb from the radiation field, the A_e of a real antenna is always less than the maximum effective aperture A_{em} of an ideal one.

By including the mixer conversion loss in the definition of effective mixer aperture, we arrive at a figure of merit which can be determined without needing to know the available RF power. No direct or indirect RF power measurement involving the mixer's antenna is required. No antenna patterns are needed to obtain directivity. The practical difficulties of pattern integration have already been noted, and they become even more severe when we try to measure a larger structure including the LO feed. The effective mixer aperture A_q characterizes the mixer just as well as does conversion loss, and A_q is much simpler to determine.

To find effective mixer aperture, one sets up a known power intensity I_{RF} at the mixer under test and measures the available IF output power. Simply dividing the IF power by the RF power intensity yields A_q :

$$A_q = P_{IF}/I_{RF}$$

(16-2)

To be exact, one must specify the direction of RF power incidence, but this is the only reference to antenna patterns needed. Comparisons between mixers at different RF frequencies should be made with care since the effective apertures of two mixers having identical directivities and conversion losses are proportional to the inverse square of the frequency ratio. The effective aperture of an isotropic radiator is proportional to the inverse square of the frequency, and when directivity is held constant, the effective mixer apertures are constrained to follow this same rule. The higher-frequency mixer will have the smaller effective aperture.

ISOTROPIC CONVERSION LOSS L_{ISO}

Effective areas are inconvenient to use in system calculations which are normally performed in decibels. For these calculations, a dimensionless number is more convenient. By assuming the antenna gain is 0 dB (that is, the antenna is isotropic), we can find an artificially low available RF power P_{ISO} from the known power intensity at the mixer. Dividing this power by the IF output power gives a quantity we call isotropic conversion loss L_{ISO} :

$$L_{iso} = P_{iso}/P_{IF} \quad (16-3)$$

Assuming an available power eliminates the need to measure it through independent antenna gain measurements, which can be awkward or impossible with the types of antennas we are considering. All we need to know is the incoming wave power intensity I_{RF} and the IF output power P_{IF} , both of which are easy to measure. Unlike effective mixer aperture A_q , L_{iso} can be used for direct comparison of mixers at different frequencies since the hypothetical isotropic antenna's aperture scales automatically with frequency. The quantity L_{iso} is the inverse of the familiar antenna gain G , if the mixer's frequency-changing property is ignored. The measurement technique is precisely the same as for antenna gain measurements except that the much more accessible IF output port is used instead of the usually inaccessible RF terminals of the mixer's antenna.

Since the effective mixer aperture A_q lumps the antenna and mixer into one black box, one can conceive of two radically different systems which could nevertheless be characterized by the same value of A_q . These systems are (1) a high-gain antenna connected to a lossy mixer and (2) a moderate-gain antenna connected to a low-loss mixer. If the product of antenna gain and conversion loss is the same in the two cases, the same A_q will result. Unless the radiation pattern of the high-gain antenna is so narrow that the quasi-optical feed is poorly illuminated, the microwave system engineer does not care how a given A_q is achieved. Planar single-element antennas rarely show gains perpendicular to the antenna plane of greater than 6 to 8 dB. This being the case, comparing

one-antenna quasi-optical mixers on the basis of A_q or L_{iso} still reflects primarily differences in conversion loss, and simplifies the laboratory work needed to establish performance figures. It also clears up some confusion which is caused when workers report conversion loss calculated by different methods.

CHAPTER 17: BOWTIE MIXER CONVERSION LOSS RESULTS

TABLE COLUMN HEADINGS

With these ideas in mind, let us turn to Table IV. In this table, the results of the conversion loss measurements performed with the quasi-optical bowtie mixer are summarized. When several trials were executed under similar conditions, the best of the trials is shown. The column labeled "No. of Diodes" shows whether a single diode or an anti-parallel-connected pair was used. The "Diode Type" column indicates whether the diodes were Hewlett-Packard 5082-2299 types with a $C_T = 0.15$ pF ("Hi-C") or 5082-2264 types with a $C_T = 0.10$ pF ("Lo-C"). "Mode of Operation" indicates whether the fundamental or the second harmonic of the LO was used to mix with the RF signal. This information is also implied in the next three columns which give the RF, LO, and IF frequencies used. Next is the column listing the incident RF power density. The IF power output resulting from this intensity follows, and division gives effective mixer aperture A_q discussed above.

The maximum effective aperture A_{em} in the next column is calculated from the antenna's measured directivity D at a wavelength λ by this equation:

TABLE IV
BOMTIE MIXER CONVERSION LOSS DATA

Trial No.	No. of diodes	Diode type	Mode of operation	f_{RF} (GHz)	f_{LO} (GHz)	f_{IF} (MHz)	I_{RF} ($\mu W/cm^2$)	P_{IF} (nW)	A_q of mixer (cm^2)	A_{em} of ant. (cm^2)	P_{max} (nW)	L (dB)	L_{150} (dB)	
1	1	Hf-C	Fund.	10.5	10.13	367	0.57	240	0.42	1.6	913	5.8	2.1	
2	1	Hf-C	Subh.	13.68	7.02	367	0.26	7.1	$27.0 \cdot 10^{-3}$	1.08	281	16.0	11.5	
3	2	Hf-C	Subh.	13.68	7.02	367	0.25	10.0	$40.6 \cdot 10^{-3}$	1.08	270	14.3	9.8	
4	2	Lo-C	Subh.	14.29	7.00	290	9.74	1335	0.137	0.989	9633	8.6	4.1	
5	2	Lo-C	Subh.	13.68	7.00	313	6.64	861	0.130	1.08	7171	9.2	4.7	
6	1	Hf-C	Subh.	34.52	17.09	348	13.8	2.5	$0.184 \cdot 10^{-3}$	--	--	--	25.1	
7	2	Lo-C	Subh.	34.52	17.11	300	12.3	31.9	$2.59 \cdot 10^{-3}$	--	--	--	13.6	
								Estimated errors:		± 1 dB	± 0.5 dB	± 0.5 dB	± 2 dB	± 1.5 dB

$$A_{em} = D \cdot (\lambda^2 / 4\pi) \quad (17-1)$$

A_{em} is related to the actual effective antenna aperture A_e by the same factor which relates directivity to gain, namely effectiveness ratio E :

$$A_e = A_{em} \cdot E \quad (17-2)$$

A lossless, conjugately matched antenna has an effectiveness ratio $E = 1.0$, and this figure will be assumed for the bowtie, since the losses in its wide conductors are probably small compared to the mixer loss. Mismatch losses are therefore ascribed to the mixer circuit rather than the antenna. The 10 GHz value for A_{em} was extrapolated from the 14 GHz figure, which in turn was obtained from the extensive pattern measurements made at that frequency. No antenna gain measurements were made at 35 GHz, so no actual conversion loss figures can be calculated for trials 4 and 5.

Continuing to the right, we find the available RF power P_{max} which was obtained by multiplying the incident intensity I_{RF} by the maximum effective aperture A_{em} . The loss figure L is the ratio of this RF power to the measured IF power. The isotropic-antenna conversion loss L_{iso} was obtained by assuming an antenna gain of 0 dB, as explained in Chapter 16.

NUMERICAL RESULTS

We shall now discuss the measurement data in detail. Trial 1 was a fundamental-mixer test at 10 GHz to see how well a single diode worked as a normal mixer in the bowtie circuit. The conversion loss of 5.8 dB is quite comparable to commercially available mixers using much more complex circuitry. It indicated that the diode parasitics were small enough to permit efficient fundamental-mode operation, which is a prerequisite to good subharmonic mixer performance.

In Trial 2 the same diode was used in the harmonic mode by raising the RF frequency to 13.68 GHz and lowering the LO frequency to 7.02 GHz. The effective mixer area decreased by about an order of magnitude, and was matched by a rise in conversion loss to 16.0 dB. This clearly shows the relative inefficiency of the single-diode subharmonic mode as compared to the fundamental mode, if we assume that the antenna impedance is relatively constant with respect to frequency.

Trial 3 used a two-diode mixer otherwise identical to the one used in the previous two trials. The improvement in conversion loss from the one-diode mixer of Trial 2 was not great (from 16.0 dB to 14.3 dB) but it is possible that the lower average impedance of the two-diode mixer was not matched well to the antenna's terminal impedance. Still, an improvement of 1.5 dB was noted in this direct-comparison test.

After the rather poor performance in the trial just described, better diodes having a maximum specified capacitance of 0.1 pF were substituted for the original diodes which had a C_T of 0.15 pF. This appar-

ently slight change in diode characteristics improved mixer operation substantially. With the other parameters essentially unchanged from Trial 3, the mixer now showed a conversion loss ranging from 8.6 to 9.2 dB in Trials 4 and 5, depending on which sideband was measured. The difference between the upper and lower sideband is probably due to a minor shift in the radiation pattern from 13.68 GHz to 14.29 GHz. While not as good as the slot-ring mixer, these conversion losses are quite acceptable for a prototype device.

Trials 6 and 7 were performed with the 35 GHz RF source, and since no bowtie antenna gains were measured at that frequency, only the A_q and L_{150} figures can be given. In a sense, apples and oranges are being compared here, because a one-diode subharmonic mixer using a high-capacitance diode was compared to a two-diode antiparallel pair of lower-capacitance types. The 11.5 dB improvement, from $L_{150} = 25.1$ dB to $L_{150} = 13.6$ dB, cannot therefore be attributed exclusively to the superiority of either the 2-diode circuit or the lower capacitance of the diodes. It is likely that both factors contributed.

The bottom line of the table shows estimated errors of the various quantities measured. These errors are probably dwarfed by the RF reflection errors introduced by the LO horn, but since there is no easy way to eliminate these from the conversion loss data, they are merely indicated. The A_q or L_{150} figures can be stated with greater confidence since RF reflections are included in these system figures.

The feed horn used for Trials 1 through 4 had a large elliptical aperture measuring about 7 cm by 10 cm. It is possible that the rela-

tively high conversion losses in Trials 2 and 3 are due to insufficient local oscillator power as well as the use of the higher-capacitance diodes.

Starting with Trial 5, a smaller LO feed horn was used whose aperture more nearly matched the size of the mixer. The mixer in front of this smaller horn is shown in Fig. 15-4. Its more concentrated aperture field coupled better to the mixer and allowed us to measure relative IF output power versus LO power at the LO horn input during Trial 5. This dependence is plotted in Fig. 17-1 and shows that the best conversion loss of 9.2 dB was obtained with a relatively low LO power input.

The most encouraging points of this data summary are these:

1. The subharmonic circuit definitely improves harmonic mixer performance. The improvement was marginal but clear at Ku-band (13 GHz), and very clear at Ka-band. It should be noted that the Ka-band improvement cannot be attributed exclusively to the use of the two-diode circuit because of the change in diode types. Nevertheless, the antiparallel-pair connection has been shown to give measureable improvement in the performance of a quasi-optical mixer.

2. Absolute conversion loss is fairly low. A value of $8.6 \text{ dB} \pm 2 \text{ dB}$ is not outstanding, but if a designer must choose between (1) the tolerable conversion loss and feasible LO power requirements of the subharmonic mixer and (2) the good conversion loss and impossible LO power requirements of the fundamental mixer, the choice to be made is clear. This is not to say the LO power requirements of the fundamental type of mixer are impossible to meet in all cases, but they will nearly always be

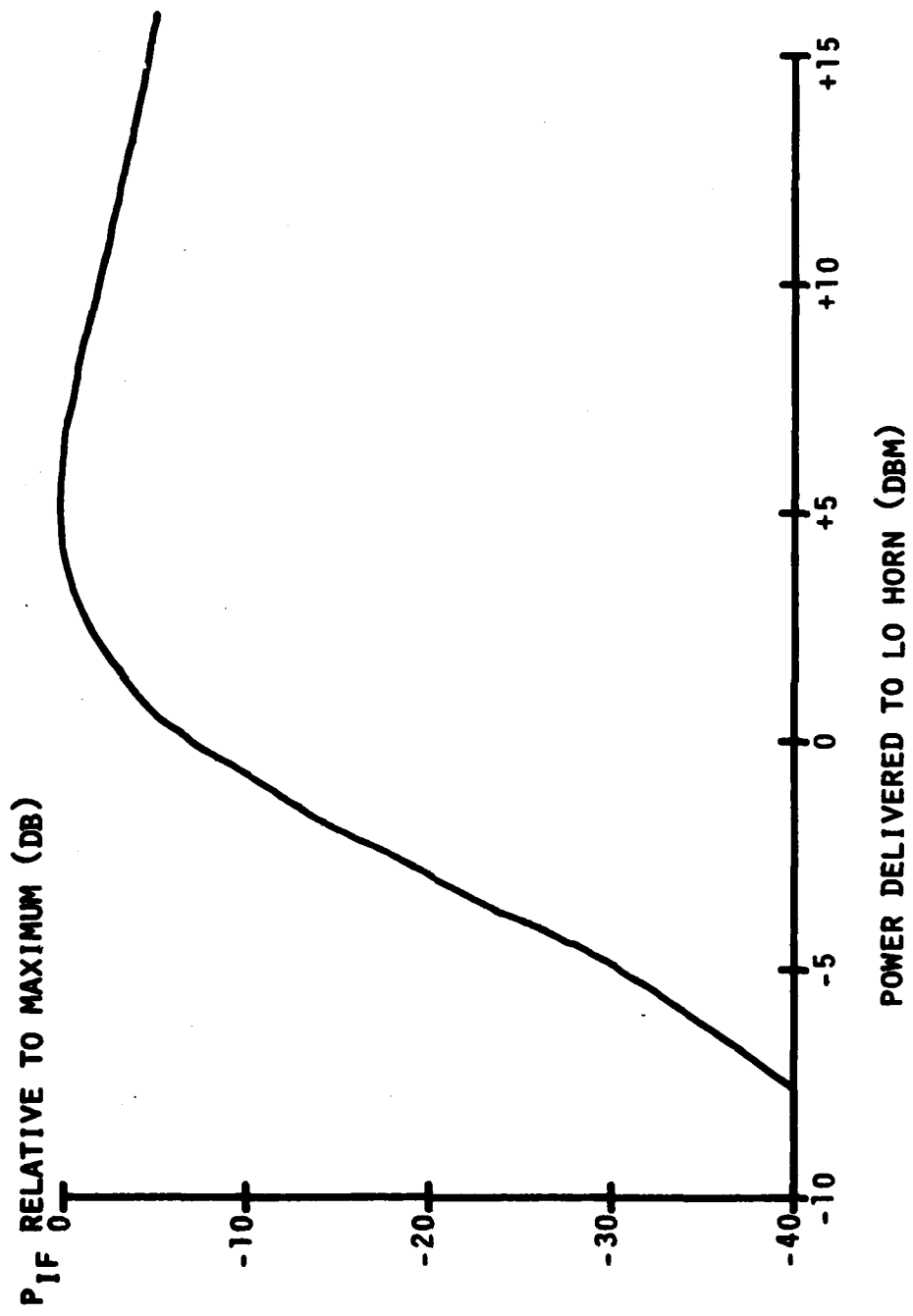


Fig. 17-1. Relative IF output power versus LO power, 14 GHz bowtie mixer.

harder to satisfy than those of a subharmonic mixer.

3. Mixer LO power requirements are relatively low. As noted in Chapter 12, the antiparallel-pair mixer has a tendency to need less LO power for optimum conversion loss than its fundamental-mixer counterpart. The fact that two diodes must be driven would seem to oppose this trend, but the effect was verified in at least one instance, during Trial 3. The optimum conversion loss was obtained at an LO power to the horn of only 60 mW, which probably delivered 10 to 15 dB less than that to the diodes. So in addition to lowering the LO frequency requirement, this type of mixer may require less LO power than the fundamental type as well.

4. The mixer was usable into the millimeter-wave band. Trials 6 and 7 were performed at the lower end of the millimeter-wave spectrum. Although the diodes were not the best available types, the encouraging results obtained with them show that this approach to quasi-optical mixer design should be applicable well past 30 GHz. At present, beam-lead diodes are being used in conventional mixers up to 100 GHz or more, and applying these devices in quasi-optical circuits should produce a mixer usable at those frequencies.

CHAPTER 18: PROPOSED USES AND CONCLUSIONS

The quasi-optical subharmonic mixer just described can be used in any application the slot-ring device can, with the exception of situations in which duplexing with dual polarizations is needed. Since the bowtie mixer requires the RF and LO waves to be polarized in the same direction, polarization-sensitive devices cannot be used for separating the two waves. However, an effect similar to polarization duplexing could be achieved over a limited bandwidth by making two dielectric screens with metallic dipoles printed on them. The dipoles on one screen would resonate at the RF frequency, and those on the other would resonate at the LO frequency. By putting the RF-resonant screen behind an array of bowtie mixers, gain in the forward direction could be enhanced, while the LO-resonant screen in front could further reduce the already small LO power requirements. The scattering cross-sections of each screen at the frequency to be passed might be excessive, but the principle is quite easy to apply.

Even without such screens, the bowtie mixer has an advantage over most other quasi-optical mixers: wide potential bandwidth. Although these experiments did not explore this possibility, the wide usable bandwidth of the bowtie means that the IF bandwidth is limited only by external circuit considerations. This is in contrast to the slot-ring mixer, which is basically a resonant circuit. Wide bandwidth is not an unmixed blessing since it carries with it the potential of a

higher noise figure. It is likely that the subharmonic mixer noise figure is somewhat higher than that of the slot-ring device. The bowtie's broader bandwidth will allow downconversion of noise from many more frequencies, although the subharmonic circuit is still better than the single-diode harmonic mixer in this respect. Regrettably, no mixer noise figures were measured. Since the mixer radiation patterns are so wide, performing a conventional hot-cold load noise figure test would have meant surrounding the entire mixer with a microwave absorber at a uniform controlled temperature.

If the noise figure of the subharmonic mixer is low enough, a wideband quasi-optical imaging system is conceivable. Since lenses and reflectors can be made "achromatic" (independent of frequency), the potential of a wideband quasi-optical imaging system is interesting, to say the least. A receiver using a bowtie array behind a lens could determine the heading of multiple targets at different wavelengths simultaneously.

In a more peaceful vein, microwave mixers using superconductive tunnelling and the Josephson effect are just beginning to be used by radio astronomers, who up to now have contented themselves with complex indirect schemes for imaging objects of interest. A salient feature of most superconductive mixers is their extremely low LO power requirement, on the order of nanowatts [1]. Such mixers are ideally suited for use in a quasi-optical array. Direct phase-coherent focal-plane imaging would be easy with such a system. Practical problems of cryogenics and fabrication remain to be overcome, but the circuits are here, waiting to be

used.

It is hoped that this work, besides contributing to man's knowledge of what can be done, will find its place in the realm of what will be done.

APPENDIX A - DERIVATION OF FAR-FIELD EXPRESSIONS

The following discussion is taken from Araki and Itoh [1]. The primary aim of their work was to calculate the resonant frequency of a circular microstrip patch antenna. They obtained expressions for the electric field on the surface of the antenna with Galerkin's method, and used those expressions to obtain the radiation pattern. Our aim in this paper is simpler: we have already assumed a certain field distribution, and merely wish to derive the radiation from this assumed field.

Suppose that the radial electric field E_r and azimuthal electric field E_ϕ both have the following azimuthal dependence:

$$E_r = e^{jn\phi} \cdot E_r(r) \tag{A-1}$$

$$E_\phi = e^{jn\phi} \cdot E_\phi(r) \tag{A-2}$$

In this appendix, the time dependence $\exp(j\omega t)$ is suppressed everywhere.

If two linear combinations of these fields are defined as

AD-A135 252

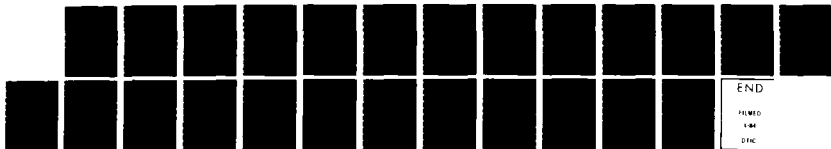
A STUDY OF MICROWAVE AND MILLIMETER-WAVE QUASI-OPTICAL
PLANAR MIXERS(U); TEXAS UNIV AT AUSTIN MICROWAVE LAB
K D STEPHAN ET AL. 31 AUG 83 MW-83-2 ARO-17735.25-EL
DAAG29-81-K-0053

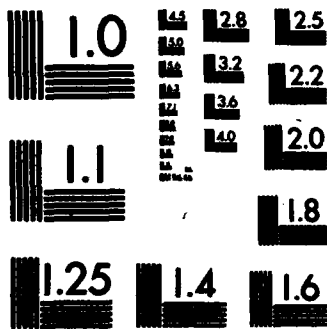
3/3

UNCLASSIFIED

F/G 9/5

NL





MICROCOPY RESOLUTION TEST CHART
NATIONAL BUREAU OF STANDARDS-1963-A

$$E_+(r) = E_r(r) + j E_\theta(r) \quad (\text{A-3})$$

$$E_-(r) = E_r(r) - j E_\theta(r) \quad (\text{A-4})$$

Araki and Itoh showed that the radiation pattern above the surface can be easily found from the Hankel transforms of these surface fields. The Hankel transform used is

$$\tilde{E}_\pm(\alpha) = \int_0^\infty E_\pm(r) J_{n\pm 1}(\alpha r) r dr \quad (\text{A-5})$$

Since it is well known that a far-field pattern can be derived directly from the Fourier-transformed aperture field, the authors began with the definition of the two-dimensional Fourier transform:

$$\tilde{F}_t(k_x, k_y) = \iint_{-\infty}^{\infty} \tilde{E}_t(x, y) \exp[j(k_x x + k_y y)] dx dy \quad (\text{A-6})$$

The rectangular aperture field components E_t can be expressed in terms of $E_+(r)$ and $E_-(r)$:

$$E_x = E_r \cos\phi - E_\phi \sin\phi = (E_+ \cdot \exp[j\phi] + E_- \cdot \exp[-j\phi])/2 \quad (\text{A-7})$$

$$E_y = (E_+ \cdot \exp[j\phi] - E_- \cdot \exp[-j\phi])/j2 \quad (\text{A-8})$$

The authors then applied a saddle-point method to derive the following far-field expressions asymptotic to the real fields as $r \rightarrow \infty$:

$$E_\theta(r, \theta, \phi) = -(k_0/2r) \cdot j^n \cdot \exp[j(n\phi - k_0 r)] \cdot [\tilde{E}_o(k_0 \sin\theta)] \quad (\text{A-9})$$

$$E_\phi(r, \theta, \phi) = +(k_0/2r) \cdot j^{n+1} \cdot \exp[j(n\phi - k_0 r)] \cdot (\cos\theta) \cdot [\tilde{E}_e(k_0 \sin\theta)] \quad (\text{A-10})$$

The even and odd functions \tilde{E}_e and \tilde{E}_o are composed of the functions \tilde{E}_+ and \tilde{E}_- :

$$\tilde{E}_e = \tilde{E}_+ + \tilde{E}_- \quad (\text{A-11})$$

$$\tilde{E}_o = \tilde{E}_+ - \tilde{E}_- \quad (\text{A-12})$$

APPENDIX B - FIELDS AT THE DIELECTRIC-AIR INTERFACE

This derivation draws heavily on a paper by Kawano and Tomimuro [1] in which the slot ring was analyzed as a resonator by using the spectral domain method. Their treatment predicted the frequencies of high-order resonances of the slot ring structure with good accuracy. Extensive attempts to apply their method to determine the resonant frequency of the first-order mode met with failure, perhaps because of the erratic behavior of Galerkin's method when the eigenvalues are not mostly real quantities. This difficulty in estimating the surface fields is a numerical one, and does not detract from the validity of their full-wave analysis. In the following paragraphs, we show how their analysis can be used to calculate the transverse fields at the dielectric-air interface from the electric fields in the gap, which are presumably known or estimated well.

Referring to Fig. B-1, the substrate material of thickness t and relative dielectric constant ϵ_r is assumed to be lossless. The axial z -directed electromagnetic fields can be expressed in the following forms using a Hankel-transform expansion:

1. In region 1 ($z > t$):

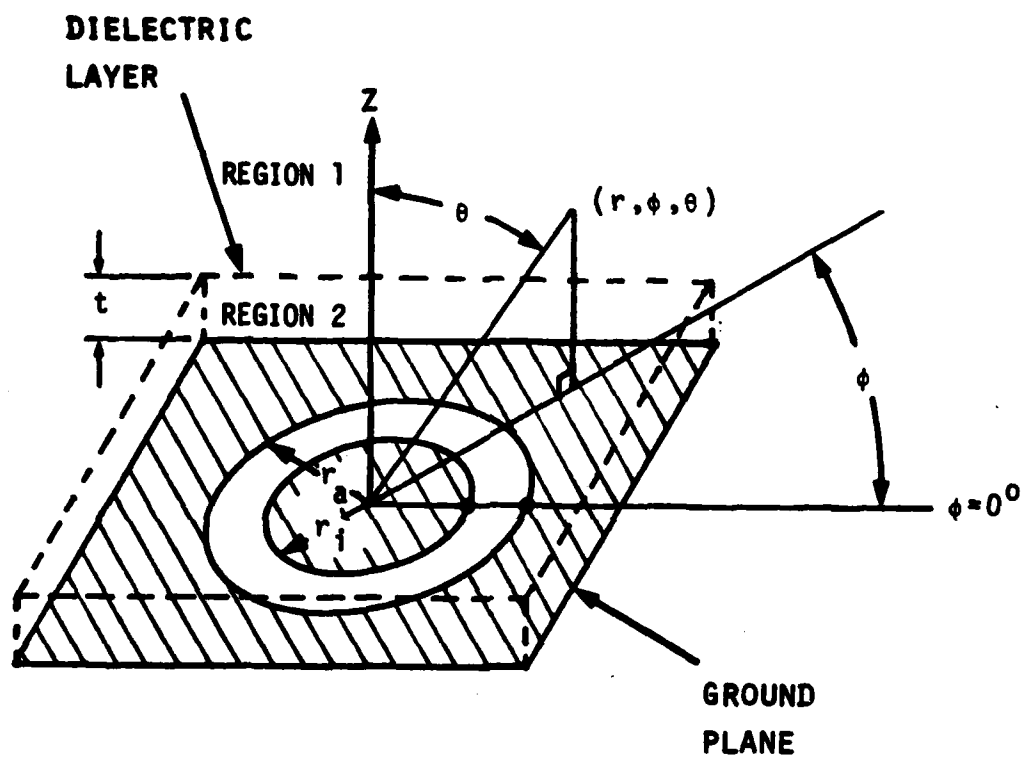


Fig. B-1. Slot-ring antenna showing coordinate system.

$$E_{z1}(r, \phi, z) = e^{jn\phi} \int_0^{\infty} A^e(\alpha) e^{-j\beta_1(z-d)} J_n(\alpha r) \alpha \, d\alpha \quad (\text{B-1})$$

$$H_{z1}(r, \phi, z) = e^{jn\phi} \int_0^{\infty} A^h(\alpha) e^{-j\beta_1(z-d)} J_n(\alpha r) \alpha \, d\alpha \quad (\text{B-2})$$

2. In region 2 ($0 < z < t$):

$$E_{z2}(r, \phi, z) = e^{jn\phi} \int_0^{\infty} [B^e(\alpha) \sin\beta_2 z + C^e(\alpha) \cos\beta_2 z] J_n(\alpha r) \alpha \, d\alpha \quad (\text{B-3})$$

$$H_{z2}(r, \phi, z) = e^{jn\phi} \int_0^{\infty} [B^h(\alpha) \sin\beta_2 z + C^h(\alpha) \cos\beta_2 z] J_n(\alpha r) \alpha \, d\alpha \quad (\text{B-4})$$

where the A's and B's are unknown functions of the Hankel transform variable α . The propagation constants are defined in the following ways:

$$\beta_1^2 = \omega^2 \epsilon_1 \mu_1 - \alpha^2 \quad (\text{B-5})$$

$$\beta_2^2 = \omega^2 \epsilon_2 \mu_2 - \alpha^2 \quad (\text{B-6})$$

$$\epsilon_2 = \epsilon_r \epsilon_0 \quad (\text{B-7})$$

$$\mu_2 = \mu_r \mu_0 \quad (\text{B-8})$$

The constants ϵ_r and μ_r are the dielectric constant and permeability of the substrate layer relative to ϵ_0 and μ_0 respectively, the values for vacuum. The z-directed fields given by Equations B-1 to B-4 result from vector potentials having only z-components proportional to solutions of the scalar Helmholtz equation in cylindrical coordinates [1]. The tangential electric and magnetic fields are derived from these z-directed fields.

If we define new tangential fields E_{\pm} and H_{\pm} which are linear combinations of the conventional radial and azimuthal fields:

$$E_+ = E_r + jE_\theta$$

(B-9)

$$E_- = E_r - jE_\theta$$

(B-10)

$$H_+ = H_r + jH_\theta$$

(B-11)

$$H_- = H_r - jH_\theta$$

(B-12)

the tangential fields in Region 2 derived from the axial fields have the following convenient form:

$$E_{2+} = e^{jn\phi} \int_0^a \{ [-B_2 B^e(\alpha) - jz_2 C^h(\alpha)] \cos \beta_2 z \\ + [B_2 C^e(\alpha) - jz_2 B^h(\alpha)] \sin \beta_2 z \} J_{n+1}(\alpha r) \alpha \, d\alpha$$

(B-13)

$$E_{2-} = e^{jn\phi} \int_0^a \{ [B_2 B^e(\alpha) - jz_2 C^h(\alpha)] \cos \beta_2 z \\ + [-B_2 C^e(\alpha) - jz_2 B^h(\alpha)] \sin \beta_2 z \} J_{n-1}(\alpha r) \alpha \, d\alpha$$

(B-14)

$$\begin{aligned}
 H_{2+} = e^{jn\phi} \int_0^{\infty} \{ & [-\beta_2 B^h(\alpha) - jy_2 C^e(\alpha)] \cos \beta_2 z \\
 & + [\beta_2 C^h(\alpha) - jy_2 B^e(\alpha)] \sin \beta_2 z \} \cdot J_{n+1}(\alpha r) \alpha \, d\alpha
 \end{aligned}
 \tag{B-15}$$

$$\begin{aligned}
 H_{2-} = e^{jn\phi} \int_0^{\infty} \{ & [\beta_2 B^h(\alpha) - jy_2 C^e(\alpha)] \cos \beta_2 z \\
 & + [-\beta_2 C^h(\alpha) - jy_2 B^e(\alpha)] \sin \beta_2 z \} \cdot J_{n-1}(\alpha r) \alpha \, d\alpha
 \end{aligned}
 \tag{B-16}$$

Similarly, the tangential fields in Region 1 are found to be:

$$E_{1+} = je^{jn\phi} \int_0^{\infty} [\beta_1 A^e(\alpha) - z_0 A^h(\alpha)] e^{-j\beta_1(z-d)} J_{n+1}(\alpha r) \alpha \, d\alpha
 \tag{B-17}$$

$$E_{1-} = je^{jn\phi} \int_0^{\infty} [-\beta_1 A^e(\alpha) - z_0 A^h(\alpha)] e^{-j\beta_1(z-d)} J_{n-1}(\alpha r) \alpha \, d\alpha
 \tag{B-18}$$

$$H_{1+} = je^{jn\phi} \int_0^{\infty} [\beta_1 A^h(\alpha) + y_0 A^e(\alpha)] e^{-j\beta_1(z-d)} J_{n+1}(\alpha r) \alpha \, d\alpha
 \tag{B-19}$$

$$H_{1-} = je^{jn\phi} \int_0^{\infty} [-\beta_1 A^h(\alpha) + y_0 A^e(\alpha)] e^{-j\beta_1(z-d)} J_{n-1}(\alpha r) \alpha \, d\alpha
 \tag{B-20}$$

where the simplifications $z_n = j\omega\mu_n$ and $y_n = j\omega\epsilon_n$ have been made for

brevery. So far, there are a total of six coefficients which are still unknown: $A^e(\alpha)$, $A^h(\alpha)$, $B^e(\alpha)$, $B^h(\alpha)$, $C^e(\alpha)$, and $C^h(\alpha)$. The values for two of these coefficients can be obtained from the assumed form of the tangential electric field at $z=0$, on the metal surface. Denoting the components of this presumably known field as $E_{\pm}(r, \phi, z)$ and the known Hankel transforms of these field components as $\tilde{E}_{\pm}(\alpha)$, we substitute the Hankel-transformed field components into Equations B-13 and B-14 to obtain:

$$\tilde{E}_{+}(\alpha, 0) = -\beta_2 B^e(\alpha) - jz_2 C^h(\alpha) \quad (\text{B-21})$$

$$\tilde{E}_{-}(\alpha, 0) = \beta_2 B^e(\alpha) - jz_2 C^h(\alpha) \quad (\text{B-22})$$

From Equations B-21 and B-22, B^e and C^h can be found explicitly:

$$C^h(\alpha) = \frac{\tilde{E}_{+}(\alpha, 0) + \tilde{E}_{-}(\alpha, 0)}{-2jz_2} \quad (\text{B-23})$$

$$B^e(\alpha) = \frac{\tilde{E}_{+}(\alpha, 0) - \tilde{E}_{-}(\alpha, 0)}{-2\beta_2} \quad (\text{B-24})$$

Now considering the dielectric-air interface, we find that by

$$H_{2+} = e^{jn\phi} \int_0^{\infty} \{ [-\beta_2 B^h(\alpha) - jy_2 C^e(\alpha)] \cos \beta_2 z + [\beta_2 C^h(\alpha) - jy_2 B^e(\alpha)] \sin \beta_2 z \} J_{n+1}(\alpha r) \alpha \, d\alpha \quad (B-15)$$

$$H_{2-} = e^{jn\phi} \int_0^{\infty} \{ [\beta_2 B^h(\alpha) - jy_2 C^e(\alpha)] \cos \beta_2 z + [-\beta_2 C^h(\alpha) - jy_2 B^e(\alpha)] \sin \beta_2 z \} J_{n-1}(\alpha r) \alpha \, d\alpha \quad (B-16)$$

Similarly, the tangential fields in Region 1 are found to be:

$$E_{1+} = je^{jn\phi} \int_0^{\infty} [\beta_1 A^e(\alpha) - z_0 A^h(\alpha)] e^{-j\beta_1(z-d)} J_{n+1}(\alpha r) \alpha \, d\alpha \quad (B-17)$$

$$E_{1-} = je^{jn\phi} \int_0^{\infty} [-\beta_1 A^e(\alpha) - z_0 A^h(\alpha)] e^{-j\beta_1(z-d)} J_{n-1}(\alpha r) \alpha \, d\alpha \quad (B-18)$$

$$H_{1+} = je^{jn\phi} \int_0^{\infty} [\beta_1 A^h(\alpha) + y_0 A^e(\alpha)] e^{-j\beta_1(z-d)} J_{n+1}(\alpha r) \alpha \, d\alpha \quad (B-19)$$

$$H_{1-} = je^{jn\phi} \int_0^{\infty} [-\beta_1 A^h(\alpha) + y_0 A^e(\alpha)] e^{-j\beta_1(z-d)} J_{n-1}(\alpha r) \alpha \, d\alpha \quad (B-20)$$

where the simplifications $z_n = j$, n and $y = j\omega \epsilon_n$ have been made for

brevity. So far, there are a total of six coefficients which are still unknown: $A^e(\alpha)$, $A^h(\alpha)$, $B^e(\alpha)$, $B^h(\alpha)$, $C^e(\alpha)$, and $C^h(\alpha)$. The values for two of these coefficients can be obtained from the assumed form of the tangential electric field at $z=0$, on the metal surface. Denoting the components of this presumably known field as $E_{\pm}(r, \phi, z)$ and the known Hankel transforms of these field components as $\tilde{E}_{\pm}(\alpha)$, we substitute the Hankel-transformed field components into Equations B-13 and B-14 to obtain:

$$\tilde{E}_{+}(\alpha, 0) = -\beta_2 B^e(\alpha) - jz_2 C^h(\alpha) \quad (\text{B-21})$$

$$\tilde{E}_{-}(\alpha, 0) = \beta_2 B^e(\alpha) - jz_2 C^h(\alpha) \quad (\text{B-22})$$

From Equations B-21 and B-22, $B(e)$ and $C(h)$ can be found explicitly:

$$C^h(\alpha) = \frac{\tilde{E}_{+}(\alpha, 0) + \tilde{E}_{-}(\alpha, 0)}{-2jz_2} \quad (\text{B-23})$$

$$B^e(\alpha) = \frac{\tilde{E}_{+}(\alpha, 0) - \tilde{E}_{-}(\alpha, 0)}{-2\beta_2} \quad (\text{B-24})$$

Now considering the dielectric-air interface, we find that by

matching tangential electric and magnetic fields at $z=d$, four more equations result:

$$E_{1+}(r, \phi, z) = E_{2+}(r, \phi, z) \quad (\text{B-25})$$

$$E_{1-}(r, \phi, z) = E_{2-}(r, \phi, z) \quad (\text{B-26})$$

$$H_{1+}(r, \phi, z) = H_{2+}(r, \phi, z) \quad (\text{B-27})$$

$$H_{1-}(r, \phi, z) = H_{2-}(r, \phi, z) \quad (\text{B-28})$$

Omitting the rather tedious but entirely straightforward algebra required, we arrive at the following expressions for the remaining four unknowns:

$$B^h(\alpha) = C^h(\alpha) \cdot \frac{\beta_2 \sin \beta_2 d - j \mu_r \beta_1 \cos \beta_2 d}{\beta_2 \cos \beta_2 d + j \mu_r \beta_1 \sin \beta_2 d} \equiv C^h(\alpha) \cdot f_h(\alpha)$$

(B-29)

$$C^e(\alpha) = B^e(\alpha) \cdot \frac{\beta_2 \cos \beta_2 d + j \epsilon_r \beta_1 \sin \beta_2 d}{\beta_2 \sin \beta_2 d - j \epsilon_r \beta_1 \cos \beta_2 d} \equiv B^e(\alpha) \cdot f_e(\alpha)$$

(B-30)

$$A^e(\alpha) = B^e(\alpha) \epsilon_r \sin \beta_2 d + C^e(\alpha) \epsilon_r \cos \beta_2 d$$

(B-31)

$$A^h(\alpha) = B^h(\alpha) \mu_r \sin \beta_2 d + C^h(\alpha) \mu_r \cos \beta_2 d$$

(B-32)

By substituting the proper coefficients into the expressions for the tangential electric field at $z = d$, we obtain:

$$\begin{aligned} \tilde{E}_+(\alpha, d) &= \tilde{E}_+(\alpha, 0) \cos \beta_2 d \\ &+ [\beta_2 B^e(\alpha) f_e(\alpha) - j z_2 C^h(\alpha) f_h(\alpha)] \sin \beta_2 d \end{aligned}$$

(B-33)

$$\begin{aligned}\tilde{E}_-(\alpha, d) &= \tilde{E}_-(\alpha, 0)\cos\beta_2 d \\ &+ [-\beta_2 B^e(\alpha)f_e(\alpha) - jz_2 C^h(\alpha)f_h(\alpha)]\sin\beta_2 d\end{aligned}\tag{B-34}$$

When the functions $\tilde{E}_e(\alpha)$ and $\tilde{E}_o(\alpha)$ are sought for use in the far-field expressions, some terms cancel and we obtain:

$$\tilde{E}_e(\alpha) = [\cos\beta_2 d + f_h(\alpha) \sin \beta_2 d] \cdot [\tilde{E}_+(\alpha, 0) + \tilde{E}_-(\alpha, 0)]\tag{B-35}$$

$$\tilde{E}_o(\alpha) = [\cos\beta_2 d - f_e(\alpha) \sin \beta_2 d] \cdot [\tilde{E}_+(\alpha, 0) - \tilde{E}_-(\alpha, 0)]\tag{B-36}$$

Thus we find the relationship between the assumed tangential electric fields at $z = 0$ (given by $\tilde{E}_\pm(\alpha, 0)$) and the fields at the surface of the dielectric.

APPENDIX C - KRADRNG PROGRAM

The following Fortran program listing was used together with some manual calculations to find the radiation resistance of the slot-ring antenna. The subprogram CSMPN is a Simpson's-rule integration subroutine, and the MMBSJ0 and MMBSJ1 functions are IMSL library subroutines developed by International Mathematical and Statistical Libraries, Inc.

```

*   K R A D R N G
*
PROGRAM KRADRNG(INPUT,OUTPUT,TAPE5=INPUT,TAPE6=OUTPUT)
EXTERNAL SUB
REAL RI,RA,FD,KNSQ,KC,PI,EPSI,MUR,NUM,DENOM,DEL
*   RESIST
COMPLEX SUM(1)
COMMON//RI,RA,KC
PI = 3.1415926535897
EPSI = 0.054E-5
MUR = 0.4*PI
*
*   THE DATA REQUIRED, IN ORDER, ARE RI,RA, (IN CM.)
*   FD (IN GHZ), AND DEL, THE INTEGRATION ERROR.
*
READ,RI
READ,RA
READ,FD
READ,DEL
*
KNSQ = ((2*PI*FD)**2)*EPSI*MUR
KC = SQRT(KNSQ)
NUM = 753.4*(ALOG(RA/RI))**2
CALL CSMPN(SUB,0,PI/2,DEL,SUM,1)
DENOM = PI*KNSQ*REAL(SUM(1))
RESIST = NUM/DENOM
PRINT
PRINT, 'RUN OF KRADRNG - AIR VERSION'
PRINT
PRINT, 'RI (CM.) = ',RI
PRINT, 'RA (CM.) = ',RA
PRINT, 'FREQUENCY (GHZ) = ',FD
PRINT, 'ERROR TOLERANCE OF INTEGRATION = ',DEL
PRINT
PRINT, 'RADIATION RESISTANCE (OHMS) = ',RESIST
PRINT
PRINT, 'END OF KRADRNG RUN'
STOP
END
*
*
*   THE SUBROUTINE SUB FORMS THE INTEGRAND.
*
SUBROUTINE SUB(THETA,TERM)
REAL, UPSILON,KC,UPPL,UPMN,THETA
COMPLEX TERM(1)
COMMON//DUM(2),KC
UPPL = UPSILON(KC*SIN(THETA),2)
UPMN = UPSILON(KC*SIN(THETA),0)
TERM(1) = (((UPPL - UPMN)**2) +
*   ((UPPL + UPMN)*COS(THETA))**2)**0.5
*   SIN(THETA)
RETURN
END
*
*

```

* THE EPSILON FUNCTION IS THE HANKEL TRANSFORM OF
 * THE ELECTRIC FIELD ESTIMATE IN THE GAP.
 *

```

FUNCTION EPSILON(ALPHA,N)
REAL RESINT,ALPHA,RA,RI,INTRA,INTRI,EPSILON
COMMON//RI,RA
IF (ALPHA.GT.1E-4) GO TO 20
IF (ALPHA.LE.0) GO TO 10
EPSILON = RA - RI
RETURN
10 EPSILON = 0.0
RETURN
20 CALL RESINT(ALPHA*PI,N,INTRA)
CALL RESINT(ALPHA*PI,N,INTRI)
EPSILON = (INTRA - INTRI)/ALPHA
RETURN
END

```

*
 *
 *
 *
 *
 *

```

FUNCTION G1(BETA1,BETA2)
REAL OMEGA,EPSE,EPREL,DEPTH,PI,EPSE
COMPLEX J,G1,BETA1,BETA2,TANB2D
COMMON//DIM(3),OMEGA,EPSE,EPREL,DEPTH
J = (0.0,1.0)
EPSE = EPSI*EPREL
TANB2D = CSIN(BETA2*DEPTH)/CCOS(BETA2*DEPTH)
G1 = ((J*OMEGA*EPSE)/(2.0*BETA2))*
> ((J*BETA2 - BETA1*EPREL*TANB2D)/
> (BETA1*EPREL + J*BETA2*TANB2D))
> = (OMEGA*EPSE)/(2.0*BETA1)
RETURN
END

```

*
 *
 *

```

FUNCTION G2(BETA1,BETA2)
REAL OMEGA,DEPTH,MUR
COMPLEX J,G2,BETA1,BETA2,TANB2D
COMMON//DIM(3),OMEGA,X1,X2,DEPTH
J = (0.0,1.0)
PI = 3.1415926535898
MUR = 8.0*PI
TANB2D = CSIN(BETA2*DEPTH)/CCOS(BETA2*DEPTH)
G2 = -((J*BETA2)/(2.0*OMEGA*MUR))*
> ((BETA1 + J*BETA2*TANB2D)/
> (J*BETA2 - BETA1*TANB2D))
> = (BETA1)/(2.0*OMEGA*MUR)
RETURN
END

```

*
 *
 *
 *
 *
 *

THE FUNCTION POIF(ALPHA) IS USED BY ZARENT TO

* FIND THE VALUE OF ALPHA FOR WHICH THE DENOMINATOR
* OF THE INTEGRAND GOES TO ZERO.

```

FUNCTION POLE(ALPHA)
REAL ALPHA, POLE, KRSQ, EPSPEL, DEPTH, ALFSQ
COMMON//KRSQ, KZSQ, DIM(3), EPSREL, DEPTH
ALFSQ = ALPHA*ALPHA
BETA1 = SQRT(ALFSQ - KRSQ)
BETA2 = SQRT(KRSQ*EPSPEL - ALFSQ)
POLE = BETA2*SIN(BETA2*DEPTH)
      - EPSREL*BETA1*COB(BETA2*DEPTH)
RETURN
END

```

*
*
*
*
*
*
*
*
*

THE SUBROUTINE RESINT PERFORMS THE INTEGRAL
FROM 0 TO 1 OF THE BESSEL FUNCTION OF THE FIRST
KIND OF ORDER N,
RETURNING THE VALUE IN INT.

```

SUBROUTINE RESINT (X,N,INT)
REAL X, INT, BESSEL, JOINT, J(40), SUM
INTEGER N, EVNO, P
IF (N.GE.-1) GO TO 5
PRINT, ORDER TOO SMALL, N
INT = 0.0
RETURN
5 IF (N.NE.-1) GO TO 10
INT = BESSEL(X,0) = 1.0
RETURN
10 IF (N.NE.1) GO TO 20
INT = JOINT(X)
RETURN
20 IF (X.GT.1E-9) GO TO 25
INT = 0.0
RETURN
25 IF (N.NE.1) GO TO 30
INT = 1.0 - BESSEL(X,1)
RETURN
30 IF (N.NE.2) GO TO 40
INT = JOINT(X) - 2.0*BESSEL(X,1)
RETURN
40 EVNO = AINT(N/2,P) = N/2.0
J(1+0) = BESSEL(X,P)
J(1+1) = BESSEL(X,1)
SUM = 0.0

```

*
*
*
*
*

THIS DO LOOP FINDS HIGHER ORDERS OF BESSEL FUNCTIONS
BY THE RECURSION RELATION, SUMMING THE PROPER
TERMS AS IT GOES.

```

DO 45 M=2,N-1
J(1+M) = ((2.0*(M-1))/X)*J(1+M-1) - J(1+M-2)
IF(EVNO.EQ.(AINT(M/2,P) - M/2.0)) GO TO 45
SUM = SUM + J(1+M)
45 CONTINUE

```

*
*
*

NOW TWO DIFFERENT EQUATIONS ARE USED DEPENDING ON
WHETHER THE ORDER IS EVEN OR ODD.


```

*
*   IF (EVAND.F.) GO TO 6A
*   INT = JOINT(X) = 2.*(J(1+1) + SUM)
*   RETURN
*
6A INT = 1.0 - J(1+0) = 2.*SUM
*   RETURN
*   END
*
*   THE FUNCTION JOINT PERFORMS THE INTEGRAL FROM 0 TO
*   X OF J(1+0). IF X < 0, A TRUNCATED SUMMATION IS USED
*   WHICH GIVES 5 DEC. PLACE ACCURACY. FOR X > 0, A
*   POLYNOMIAL APPROXIMATION IS USED.
*
FUNCTION JOINT(X)
REAL NUM,DENOM,SUM,BESSEL,J0,J1,X,JOINT,XOVA
INTEGER N,Z,NBIG,I
IF (X.LT.0.0) GO TO 10
XOVA = X/6.0
JOINT = 1.0 + ((0.79784456 - (0.1256424)/(XOVA*XOVA))
>   + SIN(X - 0.7853986)
>   - (0.06233473/XOVA - (0.0004035)/(XOVA*XOVA+XOVA))
>   + COS(X - 2.7853986))/SQRT(X)
*   RETURN
10 SUM = 0.0
NUM = X
DENOM = 1.0
J0 = BESSEL(X,0)
J1 = BESSEL(X,1)
NBIG = 170
DO 113 I=1,NBIG,4
SUM = SUM + J1*NUM/DENOM
NUM = NUM*X
DENOM = DENOM*(I+2)
SUM = SUM + J0*NUM/DENOM
NUM = NUM*X
DENOM = DENOM*(I+2)
SUM = SUM + J1*NUM/DENOM
NUM = NUM*X
DENOM = DENOM*(I+2)
SUM = SUM + J0*NUM/DENOM
NUM = NUM*X
DENOM = DENOM*(I+2)
IF(((ABS(J0) + ABS(J1))*NUM/DENOM).LT.1E-6*SUM) GO TO 120
113 CONTINUE
120 JOINT = X*(J0 + SUM)
*   RETURN
*   END
*
*
*
*   THE FUNCTION BESSEL FINDS THE BESSEL FUNCTION WITH
*   ARGUMENT X AND POSITIVE INTEGER ORDER N, RETURNING THE
*   VALUE IN RESX. THE ARRAY SUBSCRIPTS OF J( ) ARE ONE
*   HIGHER THAN THE ORDER OF THE RESPECTIVE FUNCTION, SINCE
*   THE J(N) IS NOT ALLOWED. THE RECURSION RELATION IS USED
*   FOR ORDERS HIGHER THAN 1.
*
FUNCTION BESSEL(Y,N)
REAL X,Y,RESX,MMBSJ0,MMBSJ1,J(32)
INTEGER M,N

```

```

N=KXBY
IF (X.GT.0.0) GO TO 14
PRINT,ARGUMENT OF BESSEL NEGATIVE;RESULTS WRONG.
RETURN
*
*   FOR LOW ARGUMENTS AND HIGH ORDERS, THE BESSEL FUNCTION
*   ROUTINES RUN OUT OF PRECISION AND START TO GIVE ERRONEOUS
*   RESULTS. TO ALLEVIATE THIS, A TRAP IS PLACED TO SUBSTITUTE
*   THE SMALL-ARGUMENT APPROXIMATION TO THE FUNCTION WHEN
*   APPROPRIATE. THE FOLLOWING IF STATEMENT DOES THIS.
*
14  IF ((X.LT.(N/4)),AND.(N.GT.6)) GO TO 125
    IF (N.NE.0) GO TO 50
    BESSEL=MMHBSJ0(X,IFR)
    GO TO 124
50  IF (N.NE.1) GO TO 60
    BESSEL=MMHBSJ1(X,IFR)
    GO TO 124
60  IF (N.GT.-1) GO TO 65
    BESSEL = -MMHBSJ1(X,IFR)
    RETURN
65  J(1)=MMHBSJ0(X,IFR)
    J(2)=MMHBSJ1(X,IFR)
    IF (X.GT.1E-9) GO TO 90
    BESSEL = P.0
    RETURN
90  DO 100 I=3,N+1
    J(I)=$((2.0*(I-2))/X)*J(I-1)-J(I-2)
100  CONTINUE
    BESSEL=J(N+1)
120  IF (IFR.NE.120) GO TO 130
    PRINT,BESSEL FUNCTION ARGUMENT TOO BIG - RESULTS INVALID.
125  K=1
*
*   CALCULATE NY
*
DO 127 I=1,N
    K=K+1
127  CONTINUE
BESSEL=((N.5+X)**N)/K
130  RETURN
END
*
*
*

```

BIBLIOGRAPHY

The following abbreviations are used:

BSTJ - Bell System Technical Journal

IEE -- Institution of Electrical Engineers (Great Britain)

IEEE - Institute of Electrical and Electronics Engineers

IRE -- Institute of Radio Engineers

MTT -- IEEE Transactions on Microwave Theory and Techniques

T-AP - IEEE Transactions on Antennas and Propagation

Chapter 1

1. See for example the MTT Special Issue on Solid-State Microwave/ Millimeter-wave Power Generation, Amplification, and Control, vol. MTT-27, May 1979.
2. A. A. M. Saleh and R. A. Semplak, "A Quasi-Optical Polarization-Independent Diplexer for Use in the Beam Feed System of Millimeter-wave Antennas," T-AP, vol. AP-24 (November 1976), pp. 780-787.
3. B. J. Clifton, "Schottky-Barrier Diodes for Submillimeter Heterodyne Detection," MTT, vol. MTT-25 (June 1977), pp. 457-463.
4. L. Yuan, J. Paul, and P. Yen, "140 GHz Quasi-Optical Planar Mixers," 1982 MTT International Microwave Symposium Digest, pp. 374-375.

Chapter 2

1. John R. Kraus, Antennas (New York: McGraw-Hill, 1950), pp. 361-364.
2. H. G. Booker, "Slot Aerials and their Relation to Complementary Wire Aerials (Babinet's Principle)," IEE Proceedings, vol. 93, Part IIIA, no. 4 (1946), pp. 620-626.
3. Robert E. Collin and Francis J. Zucker, Antenna Theory: Part I (McGraw-Hill, 1969), pp. 458-482.
4. S. B. Cohn, "Slot Line on a Dielectric Substrate," MTT, vol. MTT-17 (October 1969), pp. 768-778.

5. H. Ogawa, M. Akaike, M. Aikawa, T. Karaki, and J. Watanabe, "A 26-GHz Band Integrated Circuit of a Double-Balanced Mixer and Circulators," MTT, vol. MTT-30 (January 1982), pp. 34-41.
6. E. A. Mariani, C. P. Heinzman, J. P. Agrios, and S. B. Cohn, "Slot Line Characteristics," MTT, vol. MTT-17 (December 1969), pp. 1091-1096.
7. K. Kawano and H. Tomimuro, "Spectral Domain Analysis of Open Slot Ring Resonator," MTT, vol. MTT-30 (August 1982), pp. 1184-1187.
8. K. Araki and T. Itoh, "Hankel Transform Domain Analysis of Open Circular Microstrip Radiating Structures," T-AP, vol. AP-29 (January 1981), pp. 84-89.
9. M. Abramowitz and I. Stegun, Handbook of Mathematical Functions (Washington, D. C.: U. S. Government Printing Office, 1972).
10. R. F. Harrington, Time-Harmonic Electromagnetic Fields (New York: McGraw-Hill, 1961), p. 169.
11. Kraus, Antennas, p. 28.

Chapter 3

1. D. N. Held and A. R. Kerr, "Conversion Loss and Noise of Millimeter-wave Mixers," MTT, vol. MTT-26 (February 1978), pp. 49-54.
2. A. A. M. Saleh, Theory of Resistive Mixers (Cambridge, Mass.: MIT Press, 1971).
3. Held and Kerr, "Conversion Loss. . .".
4. Kawano and Tomimuro, "Spectral Domain Analysis. . .".
5. Saleh, Theory of Resistive Mixers.

Chapter 7

1. H. Lamb, "On the Reflection and Transmission of Electric Waves by a Metallic Grating," Proceedings of the London Mathematical Society, vol. 29 (1898), pp. 523-544.

Chapter 8

1. V. H. Rumsey, "Frequency-Independent Antennas," IRE National Convention Record (1957), Part I, pp. 114-118.

2. R. L. Carrel, "The Characteristic Impedance of Two Infinite Cones of Arbitrary Cross Section," T-AP, vol. AP-6 (April 1958), pp. 197-201.

Chapter 11

1. Harrington, Time-Harmonic Electromagnetic Fields, pp. 264-316.
2. Ibid., p. 277.
3. L. J. Chu, "Physical Limitations of Omnidirectional Antennas," Journal of Applied Physics, vol. 19 (December 1948), pp. 1163-1175.
4. G. H. Brown and O. M. Woodward, "Experimentally Determined Radiation Characteristics of Conical and Triangle Antennas," RCA Review, vol. 13 (December 1952), pp. 425-452.

Chapter 12

1. M. V. Schneider and W. W. Snell Jr., "Stripline Downconverter with Subharmonic Pump," BSTJ, vol. 53 (July-August 1974), pp. 1179-1183.
2. M. Cohn, J. E. Degenford, and B. A. Newman, "Harmonic Mixing with an Antiparallel Diode Pair," MTT, vol. MTT-23 (August 1975), pp. 667-673.
3. Saleh, Theory of Resistive Mixers, p. 55.
4. A. R. Kerr, "Noise and Loss in Balanced and Subharmonically Pumped Mixers: Part I - Theory," MTT, vol. MTT-27 (December 1979), pp. 938-943.
5. A. R. Kerr, "Noise and Loss in Balanced and Subharmonically Pumped Mixers: Part II - Application," MTT, vol. 27 (December 1979), pp. 944-950.

Chapter 15

1. R. Rubin, "Antenna Measurements," in Antenna Engineering Handbook, ed. H. Jasik (New York: McGraw-Hill, 1961), pp. 34-23 to 34-24.
2. Chaim Warzsmann, private communication.

Chapter 18

1. P. L. Richards, T. M. Shen, R. E. Harris, and F. L. Lloyd, "Quasiparticle heterodyne mixing in SIS tunnel junctions," Applied Physics Letters, vol. 34 (1 March 1979), pp. 345-349.

Appendix A

1. Araki and Itoh, "Hankel Transform Domain Analysis. . .".

Appendix B

1. Kawano and Tomimuro, "Spectral Domain Analysis. . .".

END

FILMED

1-84

DTIC